Durham E-Theses

Combined TEM - cathodoluminescence study of nitride semiconductor structures

Nicholas Matthews Boyall

How to cite:

Boyall, Nicholas Matthews (2003) Combined TEM - cathodoluminescence study of nitride semiconductor structures. Doctoral thesis, Durham University.

Combined TEM-Cathodoluminescence Study of Nitride Semiconductor Structures

By
Nicholas Matthews Boyall, MSci

A thesis presented in candidature for the degree of Doctor of Philosophy in the University of Durham

Department of Physics
2003

1 9 JAN 2004

Abstract

This work presents the results of an investigation into the technique of combined TEM-Cathodoluminescence and its application to the study of GaN epitaxial layers grown by MOVPE and PAMBE on sapphire and $LiAlO_2$ substrates respectively - and MOVPE grown $In_xGa_{1-x}N/GaN/Al_2O_3$ QW structures.

The measurement of CL in a TEM allows spectral information to be correlated with structural information. In-situ electron beam degradation curves of panchromatic CL from GaN epilayers and $In_{0.1}Ga_{0.9}N$ QW emission revealed a decline in the luminescence which could be attributed to the introduction of non-radiative recombination centres. The influence of thickness on both CL spectra and images was investigated experimentally and by modelling. A method of normalising STEM-CL images for thickness contrast was developed.

Application of this normalisation to $In_{0.1}Ga_{0.9}N$ QWs in cross-section revealed inhomogeneous CL with bright regions 200-700nm in width. No systematic relationship was identified between luminescence at the QW peak emission wavelength, QW_λ, and luminescence at QW_λ ±10nm. This finding does not support the hypothesis that variation in QW CL brightness is due to local compositional fluctuation. However, clusters of threading dislocations were shown to suppress QW luminescence and are suggested as a cause for the observed inhomogeneity in luminescence. A statistical analysis of (dislocation related) V-pits in $In_xGa_{1-x}N$ MQW samples revealed clustering of pits on a length scale of 60-120nm, but no long range clustering indicative of sub-grain boundaries was found.

Finally TEM-CL spectra and monochromatic line-scans were used to show that bundles of basal plane stacking faults in M-plane GaN epitaxial layers grown on $LiAlO_2$ emit radiatively at 3.3-3.35eV (100K). The radiative transition energy is consistent with models in the literature that consider basal plane stacking faults to be layers of cubic GaN in the wurtzite matrix which act as type II QWs.

Declaration

I declare that with the exception of those procedures listed below all the work presented in this thesis was carried out by the candidate. I also declare that none of this work has previously been submitted for any degree and that it is not being submitted for any other degree.

Samples were provided by:

Dr. I.W. Watson and C. Liu, Institute of Photonics, University of Strathclyde; all c-plane GaN/InGaN structures.

Dr. Achim Trampert, Paul-Drude Institute Berlin; all M-plane $LiAlO_2$/GaN samples.

SEM-CL of $LiAlO_2$ included in Figure 6.5 was provided by Dr. Achim Trampert.

AFM images included in Figures 8.10(a), 8.11(a) and 8.13(a) were performed by C. Liu

K Durose

....

Dr. K. Durose
Supervisor

N. Boyall -

....

N.M. Boyall
Candidate

Acknowledgements

First and foremost I would like to offer my thanks and gratitude to my supervisor Dr. Ken Durose without whose encouragement and enthusiasm this work would not have been possible. I would also like to thank Dr A.W. Brinkman, and Dr. D.P. Halliday for all the valuable discussions, help and encouragement over the years.

I would also like to give special thanks to Dr. Ian Watson, Chaowang Liu and Dr. Paul Edwards at the University of Strathclyde and Dr. Achim Trampert at the Paul-Drude Institute for providing not only the crystals, but also for many helpful discussions and advice.

I am extremely grateful to Norman Thompson and David Pattinson for technical support and keeping the microscope going through a seemingly endless stream of catastrophes. Recognition must also go to Pauline Russell in the drawing office for assistance in the production of diagrams for posters and papers, some of which have been amended for use in this thesis.

Thanks are due to the following group members past and present, not only for valuable discussions, but also for making the group a pleasure to work in: Arnab Basu, Ben Cantwell, Michael Cousins, Keriya Mam, John Mullins, Rainer Schmidt, David Smyth-Boyle, Andrew Yates, and Guillaume Zoppi. I would also like to wish Ben Cantwell well in his PhD study of the MTPVT growth of CdTe.

On a more personal note I would like to thank all the staff at The College of St. Hild and St. Bede for looking after me during my time in Durham, and the many friends I have made through the college and senior common room. Finally, thanks must go to my parents and wife to be, Charlotte, for supporting me through my studies. Thanks are also due to them for educating me in the correct use of punctuation and grammar, and learning more than I'm sure they ever wanted to about semiconductors.

This thesis is dedicated to
My mother and father

ABBREVIATIONS

ADF - Annular Dark Field

AFM – Atomic Force Microscopy

BF - Bright Field

BX – Bound Exciton

CDF - Centred Dark Field

CTEM - Conventional TEM

DAP – Donor Acceptor Pair

DF - Dark Field

ELOG – Epitaxial Lateral Overgrowth

FIB – Focused Ion Beam

FX – Free Exciton

HCP – Hexagonal Close-Packed

HVPE – Hydride Vapour Phase Epitaxy

LED – Light Emitting Diode

LD – Laser Diode

MBE – Molecular Beam Epitaxy

MOVPE – Metal Organic Vapour Phase Epitaxy

MQW – Multi Quantum Well

PAMBE – Plasma Assisted Molecular Beam Epitaxy

PMT – Photo-multiplier Tube

PL – Photoluminescence

QW – Quantum Well

QW$_\lambda$ – Peak Emission Wavelength from a QW

RBS – Rutherford Back-Scattering

SAD - Selected Area Diffraction

SEM – Scanning Electron Microscopy

SFE - Stacking Fault Bound Exciton

SQW – Single Quantum Well

STEM – Scanning Transmission Electron Microscopy

STEM-CL – Cathodoluminescence Measurment in STEM

(S)TEM-CL – STEM-CL or TEM-CL

TEM – Transmission Electron Microscopy

TEM-CL – Cathodoluminescence Measurement in TEM

CONTENTS

Chapter 1

Introduction

1.1 Introduction

The $In_xGa_{1-x}N$ alloy is an important material for the fabrication of light emitting diodes (LEDs) and laser diodes (LDs) spanning the visible range into the near ultra-violet [1-4]. LEDs offer increased efficiency and longer operational lifetimes compared to traditional incandescent lighting. Production of red and yellow LEDs is an established technology. However, prior to the development of $In_xGa_{1-x}N$, technology devices of similar brightness with emission extending into shorter regions of the spectrum proved problematic. LEDs based on $In_xGa_{1-x}N$ multi-quantum well (MQW) active regions operating in the blue-green region of the spectrum have facilitated the production of high-brightness, high efficiency full colour displays, and offer the possibility of replacing inefficient incandescent sources for everyday lighting.

Semiconductor LDs provide a cheap, reliable and efficient source of monochromatic light for reading and writing optical disks and in other applications such as laser printers. GaAs LDs operating in the near infrared (780nm) are used in compact disk players providing a data capacity of ~650 megabytes. The more recent digital versatile disk (DVD) uses a red AlInGaP LD operating at 650nm which, together with improved signal processing techniques, gives data capacity of ~4.7 gigabytes. A greater areal data density is possible with

a smaller wavelength laser. Data capacity has now been further increased to ~27 gigabytes in devices compliant with the *Blu-ray* standard [5] using recently commercialized 405nm LDs based around an $In_xGa_{1-x}N$ MQW.

This new technology was made possible by the pioneering research of Isamu Akasaki into the use of AlN and GaN nucleation layers for the growth of GaN films [6, 7]. Building on this research Shuji Nakamura at *Nichia Chemicals* was able to grow high quality GaN films using a low temperature buffer layer [8] and create a blue/green $In_xGa_{1-x}N$ single quantum well LED [9]. Within a short space of time LDs based around $In_xGa_{1-x}N$ MQWs were developed [10-12] with predicted lifetimes approaching 10000 hours at room temperature continuous wave operation.

Clearly the development of nitride based light emitting devices has been extremely successful. Despite this a number of materials issues remain. Nitride based devices contain large dislocation densities of the order of $10^{10}cm^{-2}$ [13]. Whilst these devices are commercially available and have acceptable lifetimes, evidence that threading dislocations act as non-radiative recombination centres [14-17] shows that a reduction in the dislocation density is necessary further to improve device efficiency and output power. Two major challenges are, therefore, to reduce the dislocation density, and to explain why the devices are so effective at high dislocation densities. A cause of dislocations is the substrates used for the growth of GaN epitaxial layers. Epitaxial GaN is commonly grown on the sapphire (0001) plane. The large mismatch between the two materials, 13.8%, is a cause of these dislocations. In addition to their role as non-radiative recombination centres, dislocations can impair the operation of LDs by acting as scattering centres for light. Complex growth procedures such as epitaxial lateral overgrowth (ELOG) have been used to reduce dislocation densities in LDs [12]. Better matched substrates, however, offer clear advantages for nitride growth.

The active regions of nitride light emitting devices are often $In_xGa_{1-x}N$ quantum well structures grown on GaN epitaxial layers. These structures exhibit high efficiencies despite the large density of threading dislocations in the GaN epilayers. There is considerable debate in the literature as to whether this efficiency is due to localised states caused by compositional inhomogeneities and/or strain [18-21]. Identification of the cause of this localisation is of importance for the realization of longer wavelength devices as the larger in-plane

(0001) lattice spacing of InN compared to GaN will lead to increased strain as the In content is increased.

The purpose of this work is to use the unusual technique of combined transmission electron microscopy and cathodoluminescence (TEM-CL) to investigate the properties of GaN epitaxial layers and $In_xGa_{1-x}N$ QW structures. TEM is a commonly used technique for the study of structure and defects in semiconductors and CL is the emission of light as a result of electron bombardment. In semiconductors this emission is a result of radiative recombination of electrons and holes generated by incident electrons. The energy of an emitted photon yields information about the energy states of the participating electron and hole pairs. Hence a CL spectrum contains information concerning the fundamental band-gap, donor and acceptor levels, and excitonic structure. The advantage of a TEM-CL system is the ability to correlate the spectroscopic CL information with structural information from TEM. CL measurements taken in such a system benefit from high spatial resolution due to surface recombination limited diffusion lengths, and limited beam broadening in comparison to the large generation volumes typically associated with the more common SEM-CL [22]. A necessary consequence of this high spatial resolution in TEM-CL is a major loss of signal due to both non-radiative recombination at surface states and a small specimen-electron beam interaction volume. This is an underlying limiting factor in all TEM-CL experiments.

In the first section of this work the historical development and progress of TEM-CL is reviewed in Chapter Two. The growth and structure of epitaxial GaN and $In_xGa_{1-x}N$ QW structures are described in Chapter Three. A description of experimental techniques is given in Chapter Four followed by the experimental results which are divided into four chapters as follows:

- Chapter Five is divided into two parts. The first describes the calibration and investigation of the TEM-CL system. In the second part the resolution of STEM-CL is considered and thin film optical interference effects are discussed and modelled.

- Aspects of TEM-CL spectroscopy are discussed in Chapter Six. The features observed in TEM-CL spectra of GaN and $In_xGa_{1-x}N$ QWs are identified and the effects of electron beam degradation are investigated.

- Chapter Seven describes STEM-CL imaging of $In_xGa_{1-x}N$ QW structures. A model to normalise CL line-scans for thickness contrast is developed and utilised to investigate inhomogeneity in QW CL emission.

- In the first part of Chapter Eight STEM-CL images of $In_xGa_{1-x}N$ SQWs are correlated with diffraction contrast TEM imaging to investigate the effects of threading dislocation on the non-uniformity of QW CL emission. The statistical distribution of threading dislocation in a TEM foil is then analysed in one dimension. This is followed by a statistical analysis of V-pits in $In_xGa_{1-x}N$ MQWs. In the second part of the chapter luminescence associated with basal plane stacking faults in M-plane GaN grown on γ-LiAlO$_2$ is investigated using TEM-CL spectroscopy and line-scans.

Overall discussion and conclusions are given in Chapter Nine. Computer code and other supplementary material is given in Appendices A-C.

1.2 References

1.   Nakamura, S., *The Roles of Structural Imperfections in InGaN-Based Blue Light-Emitting Diodes and Laser Diodes,* Science **281** (1998) 956-961.

2.   Ponce, F.A. and D.P. Bour, *Nitride-Based Semiconductors for Blue and Green Light-Emitting Devices,* Nature **386** (1997) 351-359.

3.   Morkoc, H. and S.N. Mohammad, *High-Luminosity Blue and Blue-Green Gallium Nitride Light-Emitting Diodes,* Science **267** (1995) 51-55.

4.   Nakamura, S. and G. Fasol, *The Blue Laser Diode: GaN Based Light Emitters and Lasers,* (Springer-Verlag, Heidelberg, 1997).

5.   *www.blu-ray.com.*

6.   Amano, H., N. Sawaki, I. Akasaki, and Y. Toyoda, *Metalorganic Vapor Phase Epitaxial Growth of a High Quality GaN Film Using an AlN Buffer Layer,* Applied Physics Letters **48** (1986) 353-355.

7.   Akasaki, I., H. Amano, Y. Koide, K. Hiramatsu, and N. Sawaki, *Effects of AlN Buffer Layer on Crystallographic Structure and on Electrical and Optical Properties of GaN and $Ga_{(1-x)}Al_{(x)}N$ (0<x<0.4) Films Grown on Sapphire Substrate by MOVPE,* Journal of Crystal Growth **98** (1989) 209-219.

8.   Nakamura, S., *GaN Growth Using GaN Buffer Layer,* Japanese Journal of Applied Physics **30** (1991) L1705-L1707.

9.   Nakamura, S., M. Senoh, N. Iwasa, S. Nagahama, T. Yamada, and T. Mukai, *Superbright Green InGaN Single-Quantum-Well-Structure Light-Emitting Diodes,* Japanese Journal of Applied Physics **34** (1995) L1332-L1335.

10.   Nakamura, S., M. Senoh, S. Nagahama, N. Iwasa, T. Yamada, T. Matsushita, H. Kiyoku, and Y. Sugimoto, *InGaN-Based Multi-Quantum-Well-Structure Laser Diodes,* Japanese Journal of Applied Physics **35** (1996) L74-L76.

11.   Nakamura, S., M. Senoh, S. Nagahama, N. Iwasa, T. Yamada, T. Matsushita, H. Kiyoku, Y. Sugimoto, T. Kozaki, H. Umemoto, M. Sano, and K. Chocho, *InGaN/GaN/AlGaN-Based Laser Diodes with Modulation-Doped Strained-Layer Superlattices,* Japanese Journal of Applied Physics **36** (1997) L1568-L1571.

12.   Nakamura, S., M. Senoh, S. Nagahama, N. Iwasa, T. Yamada, T. Matsushita, H. Kiyoku, Y. Sugimoto, T. Kozaki, H. Umemoto, M. Sano, and K. Chocho, *InGaN/GaN/AlGaN-Based Laser Diodes with Modulation-Doped Strained-Layer Supperlattices Grown on an Epitaxially Laterally Overgrown GaN Substrate,* Applied Physics Letters **72** (1998) 211-213.

13. Lester, S.D., F.A. Ponce, M.G. Craford, and D.A. Steigerwald, *High Dislocation Densities in High Efficiency GaN-Based Light-Emitting Diodes,* Applied Physics Letters **66** (1995) 1249-1251.

14. Cremades, A., J. Piqueras, M. Albrecht, M. Stutzmann, and H.P. Strunk, *Study of Structural Defects Limiting the Luminescence of InGaN Single Quantum Wells,* Materials Science & Engineering B **80** (2001) 313-317.

15. Rosner, S.J., E.C. Carr, M.J. Ludowise, G. Girolami, and H.I. Erikson, *Correlation of Cathodoluminescence Inhomogeneity With Microstructural Defects in Epitaxial GaN Grown by Metalorganic Chemical-Vapor Deposition.,* Applied Physics Letters **70** (1997) 420-422.

16. Cherns, D., S.J. Henley, and F.A. Ponce, *Edge and Screw Dislocations as Nonradiative Centers in InGaN/GaN Quantum Well Luminescence,* Applied Physics Letters **78** (2001) 2691-2693.

17. Sugahara, T., H. Sato, M. Hao, Y. Naoi, S. Kurai, S. Tottori, K. Yamashita, K. Nishino, L.T. Romano, and S. Sakai, *Direct Evidence that Dislocations are Non-Radiative Recombination Centers in GaN,* Japanese Journal of Applied Physics **37** (1998) L398-L400.

18. Chichibu, S., T. Azuhata, T. Sota, and S. Nakamura, *Spontaneous Emission of Localized Excitons in InGaN Single and Multiquantum Well Structures,* Applied Physics Letters **69** (1996) 4188-4190.

19. Narukawa, Y., Y. Kawakami, M. Funato, S. Fujita, S. Fujita, and S. Nakamura, *Role of Self-Formed InGaN Quantum Dots for Exciton Localization in the Purple Laser Diode Emitting at 420nm.,* Applied Physics Letters **70** (1997) 981-983.

20. Martin, R.W., P.R. Edwards, R. Pecharroman-Gallego, C. Liu, C.J. Deatcher, I.M. Watson, and K.P. O'Donnell, *Light Emission Ranging From Blue to Red From a Series of InGaN/GaN Single Quantum Wells,* Journal of Physics D: Applied Physics **35** (2002) 604-608.

21. O'Donnell, K.P., R.W. Martin, and P.G. Middleton, *Origin of Luminescence from InGaN Diodes,* Physical Review Letters **82** (1999) 237-240.

22. Yacobi, B.G. and D.B. Holt, *Cathodoluminescence Microscopy of Inorganic Solids,* (Plenum Press, New York, 1990).

Chapter 2

Review of (S)TEM-CL Technique

2.1 Introduction

CL spectroscopy and CL microscopy are widely used techniques in semiconductor characterisation. Cathodoluminescence yields information about the properties of a semiconductor such as: diffusion length (minority carrier lifetime), impurity content and distribution, lattice defects, strain, composition and is temperature dependent. The development of high resolution scanning probe CL systems in a scanning electron microscope (SEM) and scanning transmission electron microscope (STEM) has been of importance for the characterisation of nanometer scale quantum confined structures for LEDs and LDs [1-5]. In this chapter the strengths and weaknesses of SEM-CL and (S)TEM-CL are discussed. This is followed by a review of the development of (S)TEM-CL techniques and their applications.

2.2 Scanning Cathodoluminescence Microscopy

The ability to scan an electron beam over a sample allows the formation of a CL image, thus yielding information about the spatial distribution of luminescence. Keeping the beam stationary at a single point or rastering over a

small area allows spectra from different positions on a sample to be collected with a greater spatial resolution than is achievable in photoluminescence (PL) experiments. The SEM is therefore highly suited for CL measurements and as such SEM-CL is a widely used technique.

SEM-CL. The main advantage of SEM-CL is that a bulk sample may be used thereby saving on preparation time and allowing a large region to be rapidly evaluated. SEM-CL is non-destructive as long as the specimen is not affected by the electron beam. A necessary consequence of using a bulk sample is the formation of the so called generation volume [2]. This region excited by the incident beam is typically of the order of microns at typical SEM operating voltages (15-40kV) and thus limits the resolution of SEM-CL to this size. This is both beneficial and disadvantageous. Depth resolved CL takes advantage of the generation volume through experiments where the primary beam voltage is varied to change the depth of the generation volume in a controlled manner. This is a useful technique for investigating buried structures. Calibration of the extent of the generation volume, however, is difficult and care must be taken to consider internal absorption of the luminescence. On the negative side a micron scale spatial resolution is inadequate for the investigation of nanoscale structures. Techniques developed to overcome this include the use of a low energy (~1kV) electron probe [6] or the analysis of a thin foil.

(S)TEM-CL. Installation of a CL collection system into a TEM or STEM is complex due to space constraints in the TEM pole piece; therefore there need to be clear benefits over SEM-CL to justify the conversion of a TEM. The main impetus to implement such a system is the ability to correlate spectroscopic information with structural information from diffraction contrast TEM. The spatial resolution in STEM-CL is much improved on SEM-CL, a typical resolution being 100nm (See Chapter 5 for further discussion of spatial resolution). This is due to limited beam broadening in a TEM foil and a smaller, surface recombination limited, diffusion length. Conversely to bulk SEM-CL an increase in primary electron beam energy decreases beam broadening, whereas for a bulk specimen such an increase will extend the range of the generation volume. These benefits are offset by dramatically reduced CL intensity compared to SEM-CL, due to a smaller excitation volume and large losses of free carriers to surface

recombination. High beam energies in TEM (>100keV) also increase the likelihood of specimen damage.

Before proceeding to a review of the literature it is first necessary to clarify the difference between TEM-CL and STEM-CL. In TEM-CL the microscope is operated in conventional TEM mode with the ability to collect CL spectra from the material illuminated by the beam. STEM-CL is either performed in a dedicated STEM or a TEM with scanning attachment. This allows panchromatic and monochromatic images to be collected for comparison with STEM bright field (BF) or annular dark field (ADF) images from exactly the same region. Spectra may be collected using a stationary probe or a scanning probe either to average the CL signal over a larger area or to minimise beam damage.

2.3 Review of (S)TEM-CL

The earliest report of TEM-CL is by Kingsley [7]. STEM-CL was first described by Pennycook *et al* [8] in the Cavendish laboratory and Petroff *et al* [9] at Bell laboratories. These two groups implemented quite different techniques for collecting the luminescence and reflecting it out of the microscope column.

Pennycook and co-workers [8] adapted a dedicated STEM using a concave aluminium reflector built into the sample holder on the electron exit side of the specimen. This design allowed for uniform collection over an area ~1mm in diameter thereby eliminating lengthy alignment procedures. A tapered, silvered tube collected the luminescence before directing it into a quartz light guide and photomultiplier (PMT). The light guide could be replaced with fibre optics connected to a spectrometer when needed [10]. A major advantage of this design was that it allowed the specimen to be tilted, thereby enabling investigations into the variation of CL intensity with diffraction conditions to be performed [8, 11, 12]. Panchromatic STEM-CL images and line-scans were used to demonstrate that dislocations in type IIb diamond act as sites for radiative recombination. No correlation with dislocation type was found, however, and dislocations of the same type were shown to be also non-luminescent in some occurrences [10, 11]. Performance of this system was inhibited by considerable background noise as a result of stray electrons striking the silvered collection tube. This was overcome by moving the collection tube to the electron entrance side with the specimen

tilted towards the tube [13, 14] and later by replacing the tube with a plane mirror at 45° to the specimen reflecting light on to a collimating lens and PMT assembly [15-17].

The CL collection system implemented by Petroff *et al* [9] was installed in a TEM with scanning facilities. An elliptical mirror positioned above the specimen reflected the luminescence from the specimen onto an arrangement of planar mirror and optical fibre for transmission out of the microscope. The luminescence was then dispersed in a monochromator before detection by a PMT or solid state detector. Using a combination of electron beam induced current (EBIC), STEM and monochromatic STEM-CL imaging Petroff *et al* [18, 19] observed non-radiative carrier recombination at misfit dislocations at a $Ga_{1-x}Al_xAs_{1-y}P_y$/GaAs interface with edge sessile dislocations found to be electrically neutral. The absence of non-radiative recombination was explained by suggesting the dislocation has no dangling bonds [19]. Studies of GaAs/$Ga_{1-x}Al_xAs$ double heterostructures identified defect-bound exciton emission lines associated with point defects concentrated around dislocations and showed interface roughness in QW superlattices to be related to trapped impurities at the inferfaces [20-23]. Magnea *et al* [24, 25] used EBIC and STEM-CL for the study of InP/InGaAs photodiodes, determining microplasmas to be associated with increased electric fields localised at doping fluctuations. In later work Cibert *et al* [26] and Petroff, latterly at the University of California, [27-29] investigated GaAs/AlGaAs quantum wires and boxes demonstrating the effectiveness of high resolution STEM-CL for the investigation of nanoscale structures. Lines were attributed to transitions from ground and excited states within these low-dimensional structures and demonstrated to originate from them using monochromatic STEM-CL imaging.

Following the pioneering work of Pennycook and Petroff a number of laboratories began to implement (S)TEM-CL systems. The first of these was Bristol. Bearing similarities to the system at Bell the Bristol apparatus consisted of a retractable, ellipsoidal mirror positioned above the specimen reflecting luminescence outside the microscope column onto a quartz light guide and a grating monochromator [30-35]. A continuous flow liquid He cold stage allowed samples to be cooled to 30K. The main advantage of this system over the light guide used by Pennycook is improved collection efficiency, albeit at the cost of a

smaller collection area, ~150μm, leaving no space to tilt the specimen with the CL mirror in place. The performance of this system is reviewed by Steeds [36].

Myhajlenko *et al* [34] report on CL studies of individual dislocations in ZnSe and InP. Y-band luminescence at 2.60eV and S-band at 2.52eV in ZnSe was attributed to dislocations. Specifically the Y-emission was correlated to quenching of exitonic (2.79eV) emission in regions of high dislocation density. This quenching was shown to be variable at screw dislocations. However, in studies of InP crystals [34, 37, 38] although exciton quenching was observed at dislocations no dislocation related luminescence was observed.

Wang *et al* studied molecular beam epitaxy (MBE) grown AlGaAs/GaAs quantum well structures [39-41] and AlGaAs/GaAs quantum dots [42]. Monochromatic STEM-CL imaging revealed that residual impurities in the growth system tended to be trapped in the first QW grown and agglomerate at defect interfaces [39, 40, 43]. These investigations included the first reported application of STEM-CL to an electron transparent cross-sectional foil [41], demonstrating a spatial resolution of ~50nm normal to the QW. In other work the origins of degradation mechanisms in AlGaAs/GaAs laser diode structures was studied [44] using STEM-CL spectra to identify Al fluctuations in AlGaAs epilayers. These fluctuations were considered to induce stress into the layers promoting defect formation. CL analysis of $In_xGa_{1-x}P$/GaAs strained layers identified an increase in CL emission energy and a reduction in the FWHM with compressive strain [45, 46].

Implementing a similar CL collection system to Bristol, Yamamoto *et al* [47] at Arizona State University describe a (S)TEM-CL system with the added innovation of a polariser mounted directly in front of the monochromator. This was used to identify the dislocation emission at 2.85eV in type IIb diamond (previously identified by Pennycook *et al* [11]) as being polarised along the dislocation line [47, 48]. CL studies of chemical vapour deposition (CVD) grown diamond films by Graham *et al* [49-52] showed that band-A emission due to closely spaced donor-acceptor pairs (431 and 436nm) is correlated with dislocations, whilst band-A emission due to widely spaced donor-acceptor pairs (586 and 607nm) was shown to be uniformly distributed throughout the film. The use of high resolution STEM-CL monochromatic imaging for assessing doping was demonstrated by imaging boron related CL emission at 2.32eV in diamond films [53].

At the Tokyo Institute of Technology, Yamamoto (formerly at Arizona State University) reports the construction of a (S)TEM-CL detection system based around an ellipsoidal collection mirror which could be positioned either above or below the specimen [54]. By positioning the mirror below the specimen Yamamoto and Toda [55-57] demonstrated that Cherenkov radiation generated by high energy electrons exceeding the critical velocity[1], v_c, in a specimen could be detected in a TEM. Polarisation-dependent CL studies of plan-view and cross-sectional ZnSe films grown on GaAs substrates revealed Y-band emission at 2.60eV (previously identified as dislocation related by Myhajlenko *et al* [34]) to be polarised parallel to the dislocation line [58-61]. The action of defects in a ZnCdSe/ZnSe QW structure was also investigated using the STEM-CL method [62]. Inhomogeneous QW emission was observed and attributed to well thickness fluctuations and recombination at defects and impurities.

Mitsui et al [58, 63, 64] correlated diffraction contrast TEM and monochromatic CL images of ZnS films on GaAs in plan view and cross-section. A reduction in neutral-acceptor to bound-exciton and free-electron to ionised-acceptor emission in regions of high stacking fault density was observed. Deep level emission at 425nm due to Ga doping was observed in these samples close to the interface. This was attributed to the diffusion of Ga atoms from the substrate. An unexpected peak was also identified at 527nm and attributed to point defects produced during Ar^+ milling. This hypothesis was confirmed by in-situ observation of the CL emission using the electron beam as a source of point defects [65] revealing a linear rise in CL emission at this wavelength during electron beam irradiation at 100keV [66].

Further studies into beam degradation processes were carried out by Ohno and Takeda [67-69] using a TEM specially developed for both simultaneous CL and PL studies [70]. PL excitation was achieved by shining a laser beam into the microscope column through an optical window and reflecting it down the column using an on-axis mirror with a hole to allow the electron beam passage. A 20μm diameter laser spot could then be positioned on the TEM foil with an accuracy of 1μm by adjusting the optics outside the microscope. Collected CL and/or PL was guided out of the column using an ellipsoidal mirror focusing light onto an optical fibre coupled to a monochromator. In-situ PL/CL spectroscopy of GaP during

---

[1] $v_c=c/n$, where c is the velocity of light and n is the refractive index of the medium

irradiation with 200keV electrons revealed degradation of the luminescence at a temperature of 90K. Cooling to 20K arrested the degradation [67]. The degradation curves were modelled analytically using a recombination centre model for the introduction of non-radiative recombination centres. This analysis was then extended to the electron beam induced degradation of InGaP by Ohno *et al* [68, 69] and elsewhere by Bailey *et al* [71].

Recent innovation of the (S)TEM-CL concept includes the work carried out by Furuya and Saito [72] who incorporated a 25keV Ga focused ion beam (FIB) gun into a CL equipped TEM. This device was capable of forming a 200nm diameter collimated Ga^+ beam with a 80pA spot intensity. Boundaries between FIB irradiated and unirradiated areas were identified by TEM and investigated with CL showing a decrease in the CL from FIB irradiated regions. This is suggested to be a strain-induced effect due to ion implantation. Tanabe *et al* [73] describe a specially constructed TEM specimen holder containing a flat reflector below the specimen reflecting light into a quartz fibre leading out of the microscope. This design has the major advantage of allowing large angle tilting and requires no modifications to the microscope. The performance of this CL enabled specimen holder is as yet limited by lack of sample cooling and light emission from the optical fibre due to stray electrons. Other reports of STEM-CL are by Gao *et al* [74] of voids in Y_2O_3:Eu thin films investigated by CL in a Z-contrast STEM; Ohno and Takeda [75] who consider the effect of reflection off an ellipsoidal mirror on the polarisation of CL; and Grillo et al [76] who use STEM-CL to investigate Cu drops formed on InAs ultrathin QWs.

More recently monochromatic STEM-CL analysis has been used to investigate the optical properties of dislocations in GaN [5, 77, 78] and the luminescence from $In_xGa_{1-x}N$ QWs [79]. Albrecht *et al* [79] use an *Oxford MonoCL* system with a paraboloidal CL collection mirror together with energy filtered TEM (performed in a separate instrument) to investigate the optical, compositional and structural properties of $In_xGa_{1-x}N$ QWs (*x*=0.1 and 0.2). They report uniform QW emission in cross-section with a constant FWHM as the spot size is increased from 5nm to 1μm suggesting well thickness and composition is uniform on a length scale >5nm. Compositional analysis of these same samples showed inhomogeneous In distribution in the QWs on a length scale of 3-9nm. They conclude that the optical properties of $In_xGa_{1-x}N$ QWs are therefore not influenced by In segregation on a nanometer scale. Remmele *et al* [77] and Albrecht *et al*

[78] addressed the controversial topic of whether dislocations in GaN act as recombination centres. TEM imaging and STEM-CL of dislocations showed strong contrast in band-edge CL images of edge dislocations in agreement with Yamamoto [5]. A-type 60° basal plane dislocations introduced by indentation were shown to be sites of radiative recombination with an emission energy of 2.9eV, whilst a–type screw dislocations were seen to be non-radiative recombination centres.

To summarise, a brief review of the development and applications of CL collection in a TEM or STEM has been presented with consideration of the merits and disadvantages of the different CL collection techniques. The use of an ellipsoidal or parabolic mirror positioned above the specimen is a popular method offering uniform, efficient collection. The major limitation of this design is the proximity of the mirror to the specimen making tilting impossible with the mirror in place. STEM-CL has been shown to be a powerful technique for the investigation of the optical properties of dislocations in II-VI and III-V semiconductors and in the characterisation of quantum confined structures.

2.4 References

1. Yacobi, B.G. and D.B. Holt, *Cathodoluminescence Scanning Electron Microscopy of Semiconductors*, Journal of Applied Physics **59** (1986) R1-R24.

2. Yacobi, B.G. and D.B. Holt, *Cathodoluminescence Microscopy of Inorganic Solids*, (Plenum Press, New York, 1990).

3. Petrov, V.I., *Cathodoluminescence Scanning Microscopy*, Physica Status Solidi A **133** (1992) 189-230.

4. Gustafsson, A., M.-E. Pistol, L. Montelius, and L. Samuelson, *Local Probe Techniques for Luminescence Studies of Low-Dimensional Semiconductor Structures*, Journal of Applied Physics **84** (1998) 1715-1775.

5. Yamamoto, N., *Development of Cathodoluminescence for Semiconductor Research*, in *Nanoscale Spectroscopy and Its Applications to Semiconductor Research*, Y. Watanabe, S. Heun, G. Salviati, and N. Yamamoto, (Springer-Verlag, Heidelberg, 2002).

6. Norman, C.E., *Challenging the Spatial Resolution Limits of CL and EBIC*, Solid State Phenomena **78-79** (2001) 19-28.

7. Kingsley, N., *An Apparatus for Studying Cathodoluminescence in Transmission Electron Microscope Specimens*, Septieme Congres International de Microscopie Electronique, Grenoble (1970) 285-286.

8. Pennycook, S.J., A.J. Craven, and L.M. Brown, *Cathodoluminescence on a Scanning Transmission Electron Microscope*, Institute of Physics Conference Series **36** (1977) 69-72.

9. Petroff, P.M., D.V. Lang, J.L. Strudel, and R.A. Logan, *Scanning Transmission Electron Microscopy Techniques for Simultaneous Electronic Analysis and Observation of Defects in Semiconductors*, Scanning Electron Microscopy **1** (1978) 325.

10. Pennycook, S.J. and L.M. Brown, *Cathodoluminescence at Dislocations in Divalent Oxides*, Journal of Luminescence **18/19** (1979) 905-909.

11. Pennycook, S.J., L.M. Brown, and A.J. Craven, *Observation of Cathodoluminescence at Single Dislocations by STEM*, Philosophical Magazine A **41** (1980) 589-600.

12. Pennycook, S.J. and A. Howie, *Study of Single-Electron Excitations by Electron Microscopy, II, Cathodoluminescence Image Contrast From Localized Energy Transfers*, Philosophical Magazine A **41** (1980) 809-827.

13. Pennycook, S.J., *Investigation of the Electronic Effects of Dislocations by STEM*, Ultramicroscopy **7** (1981) 99-104.

14.   Pennycook, S.J., *A Simple Cathodoluminescence Detector for the STEM,* Institute of Physics Conference Series **61** (1981) 55-58.

15.   Berger, S.D. and L.M. Brown, *Cathodoluminescence From Dislocations in Type II Natural Diamond,* Institute of Physics Conference Series **68** (1983) 115-117.

16.   Berger, S.D., D. McMullan, J. Yuan, and L.M. Brown, *The Spectrum of Cathodoluminescence From Thin Films in STEM,* Institute of Physics Conference Series **78** (1985) 137-140.

17.   Yuan, J., P. Caro, and L.M. Brown, *Correlation Between Cathodoluminescence and the Composition of a Tb^{3+} Doped Phosphor,* Institute of Physics Conference Series **78** (1985) 307-310.

18.   Petroff, P.M., R.A. Logan, and A. Savage, *Nonradiative Recombination at Dislocations in III-V Compound Semiconductors,* Journal of Microscopy **118** (1980) 255-261.

19.   Petroff, P.M., R.A. Logan, and A. Savage, *Nonradiative Recombination at Dislocations in III-V Compound Semiconductors,* Physical Review Letters **44** (1980) 287-291.

20.   Petroff, P.M., C. Weisbuch, R. Dingle, A.C. Gossard, and W. Wiegmann, *Luminescence Properties of GaAs-Ga$_{(1-x)}$Al$_{(x)}$As Double Heterostructures and Multiquantum-Well Superlattices Grown by Molecular Beam Epitaxy,* Applied Physics Letters **38** (1981) 965-967.

21.   Petroff, P.M., *Luminescence Properties of GaAs Epitaxial Layers Grown by Liquid Phase Epitaxy and Molecular Beam Epitaxy,* in *Defects in Semiconductors,* J. Narayan and T.Y. Tan, (North-Holland, Amsterdam, 1981).

22.   Petroff, P.M., R.C. Miller, A.C. Gossard, and W. Wiegmann, *Impurity Trapping, Interface Structure, and Luminescence of GaAs Quantum Wells Grown by Molecular Beam Epitaxy,* Applied Physics Letters **44** (1984) 217-219.

23.   Cibert, J., P.M. Petroff, D.J. Werder, S.J. Pearton, A.C. Gossard, and J.H. English, *Kinetics of Implantation Enhanced Interdiffusion of Ga and Al at GaAs-Ga$_{(x)}$Al$_{(1-x)}$As Interfaces,* Applied Physics Letters **49** (1986) 223-225.

24.   Magnea, N., P.M. Petroff, F. Capasso, R.A. Logan, K. Alavi, and A.Y. Cho, *Electric Field Dependent Cathodoluminescence of III-V Compound Heterostructures: A New Interface Characterisation Technique,* Applied Physics Letters **46** (1985) 1074-1076.

25.   Magnea, N., P.M. Petroff, F. Capasso, R.A. Logan, and P.W. Foy, *Microplasma Characteristics in InP-In$_{(0.53)}$Ga$_{(0.47)}$As Long Wavelength Avalanche Photodiodes,* Applied Physics Letters **46** (1985) 66-68.

26. Cibert, J., P.M. Petroff, G.J. Dolan, S.J. Pearton, A.C. Gossard, and J.H. English, *Optically Detected Carrier Confinement to One and Zero Dimension in GaAs Quantum Well Wires and Boxes,* Applied Physics Letters **49** (1986) 1275-1277.

27. Petroff, P.M., *Carrier Confinement to One and Zero Degrees of Freedom: The Optical and Structural Properties of Quantum Wires and Quantum Boxes in Gallium Arsenide,* Institute of Physics Conference Series **87** (1987) 187-193.

28. Petroff, P.M., J. Cibert, A.C. Gossard, G.J. Dolan, and C.W. Tu, *Interface Structure and Optical Properties of Quantum Wells and Quantum Boxes,* Journal of Vacuum Science and Technology B **5** (1987) 1204-1208.

29. Li, Y.J., S. Sasa, W. Beinstingl, M.S. Miller, Z. Xu, G. Snider, and P.M. Petroff, *Optical Studies of Direct Modulation Doping and Quantum Wire Formation by Focused Si on Beam Implantation,* Journal of Vacuum Science and Technology B **9** (1991) 3456-3458.

30. Roberts, S.H., *Cathodoluminescence of ZnS in the Transmission Electron Microscope,* Institute of Physics Conference Series **60** (1981) 377-380.

31. Roberts, S.H., *Cathodoluminescence Spectrometer Design for the TEM,* Institute of Physics Conference Series **61** (1981) 51-54.

32. Roberts, S.H. and J.W. Steeds, *High Resolution in Scanning Cathodoluminescence of ZnS "Edge Emission",* Journal of Crystal Growth **59** (1982) 312-316.

33. Myhajlenko, S., *Near Infrared Cathodoluminescence Assessment of Semiconductors in a TEM,* Institute of Physics Conference Series **68** (1983) 111-114.

34. Myhajlenko, S., J.L. Batstone, H.J. Hutchinson, and J.W. Steeds, *Luminescence Studies of Individual Dislocations in II-VI (ZnSe) and III-V (InP) Semiconductors,* Journal of Physics C: Solid State Physics **17** (1984) 6477-6492.

35. Day, J.C.C., *Parallel Detection of Cathodoluminescence,* PhD Thesis (1988), H.H. Wills Physics Laboratory, Univeristy of Bristol, Bristol.

36. Steeds, J.W., *Performance and Applications of a STEM-Cathodoluminescence System,* Revue de Physique Appliquee **24** (1989) C6-65 - C6-72.

37. Hutchinson, H.J. and S. Myhajlenko, *TEM Cathodoluminescence Study of Recombination Behaviour at Dislocations in Indium Phosphide,* Philosophical Magazine B **50** (1984) L49-L53.

38. Graham, R.J., S. Myhajlenko, and J.W. Steeds, *High-Resolution Luminescence Studies of Indium Phosphide Under Ohmic Contacts,* Journal of Applied Physics **57** (1985) 1311-1316.

39. Wang, J., J.W. Steeds, and C.W. Tu, *The Investigation of Impurity Distributions Around an Oval Defect in Molecular Beam Epitaxy AlGaAs/GaAs Single Quantum Wells by Transmission Electron Microscopy and Cathodoluminescence.*, Institute of Physics Conference Series **95** (1988) 45-50.

40. Wang, J., *Cathodoluminescence and Transmission Electron Microscopy Characterisation of GaAs/AlGaAs and InGaAs/InP Quantum Well Structures*, PhD Thesis (1990), H.H. Wills Physics Laboratory, University of Bristol, Bristol.

41. Wang, J., J.W. Steeds, and M. Henini, *High-Resolution TEM-CL From the Cross-Sectional Specimens of GaAs/AlGaAs QWs*, Journal de Physique IV **1** (1991) C6-125 - C6-130.

42. Wang, J., J.W. Steeds, and H. Arnot, *The Study of Individual Free Standing GaAs/AlGaAs Quantum-Dots by STEM-CL*, Microscopy Microanalysis Microstructures **1** (1990) 241-246.

43. Bailey, S.J. and J.W. Steeds, *Cathodoluminescence Studies of Oval Defects in Quantum-Well Structures*, Institute of Physics Conference Series **100** (1989) 777-782.

44. Sieber, B., J.L. Farvacque, J. Wang, and J.W. Steeds, *Possible Origin of Degradation Mechanisms in AlGaAs/GaAs Laserlike Structures*, Applied Physics Letters **60** (1992) 2654-2656.

45. Wang, J.N., J.W. Steeds, and M. Hopkinson, *The Study of MBE Grown (001) $In_{(x)}Ga_{(1-x)}P$/GaAs Strained-Layer Heterostructures by TEM and CL*, Institute of Physics Conference Series **134** (1993) 295-300.

46. Wang, J.N., J.W. Steeds, and M. Hopkinson, *Microstructure and Cathodoluminescence of MBE-Grown (001) InGaP/GaAs Strained-Layer Heterostructures*, Semiconductor Science and Technology **8** (1993) 502-508.

47. Yamamoto, N., J.C.H. Spence, and D. Fathy, *Cathodoluminescence and Polarization Studies from Individual Dislocations in Diamond*, Philosophical Magazine B **49** (1984) 609-629.

48. Yamomoto, J.C.H. Spence, and D. Fathy, *Cathodoluminescence and Polarization Studies from Individual Dislocations in Diamond*, Norelco Reporter **32** (1985) 38-52.

49. Graham, R.J., J.B. Posthill, R.A. Rudder, and R.J. Markunas, *Cathodoluminescence From Diamond Films Grown by Plasma-Enhanced Chemical Vapor Deposition in Dilute $CO/H_2, CF_4/H_2$, and CH_4/H_2 Mixtures*, Applied Physics Letters **59** (1991) 2463-2465.

50. Graham, R.J., T.D. Moustakas, and M.M. Disko, *Cathodoluminescence Imaging of Defects and Impurities in Diamond Films Grown by Chemical Vapor Deposition*, Journal of Applied Physics **69** (1991) 3212-3218.

51. Graham, R.J. and K.V. Ravi, *Cathodoluminescence Investigation of Impurities and Defects in Single Crystal Diamond Grown by the Combustion-Flame Method*, Applied Physics Letters **60** (1992) 1310-1312.

52. Graham, R.J., *Investigation of CVD-Grown Diamond by Cathodoluminescence in TEM*, Materials Research Society Symposium Proceedings **242** (1992) 97-107.

53. Graham, R.J., F. Shaapur, Y. Kato, and B.R. Stoner, *Imaging of Boron Dopant in Highly Oriented Diamon Films by Cathodoluminescence in a Transmission Electron Microscope*, Applied Physics Letters **65** (1994) 292-294.

54. Yamamoto, N., *Characterization of Crystal Defects by Cathodoluminescence Detection System Combined with TEM*, Transactions of the Japan Institute of Metals **31** (1990) 659-665.

55. Yamamoto, N. and H. Sugiyama, *Cherenkov and Transition Radiation Generated in 200kV Electron Microscope*, Radiation Effects and Defects in Solids **117** (1991) 5-10.

56. Sugiyama, H., A. Toda, and N. Yamamoto, *Detection of Cherenkov and Transition Radiation in TEM*, ICEM 13, Paris (1994) 833-834.

57. Yamamoto, N. and A. Toda, *Imaging of Cherenkov and Transition Radiation from Thin Films and Particles*, Scanning Microscopy **9** (1995) 669-676.

58. Mitsui, T., N. Yamamoto, J. Yoshino, T. Tadokoro, S. Ohta, K. Yanashima, and K. Inoue, *Correlation Between Cathodoluminescence and Structural Defects in ZnS/GaAs(100) and ZnSe/GaAs(100) Studied by Transmission Electron Microscopy*, Applied Surface Science **100/101** (1996) 625-633.

59. Mitsui, T. and N. Yamamoto, *Distribution of Polarized-Cathodoluminescence Around the Structural Defects in ZnSe/GaAs(001) Studied by Transmission Electron Microscopy*, Journal of Applied Physics **81** (1997) 7492-7496.

60. Mitsui, T. and N. Yamamoto, *Polarised-Cathodoluminescence Imaging by Using Transmission Electron Microscope: The Y_0 Emission and the Dislocations in ZnSe*, ICEM 14, Mexico (1998) 455-456.

61. Mita, T., N. Yamamoto, T. Mitsui, S. Heun, A. Franciosi, and J.M. Bonard, *Cathodoluminescence Study of the Y0 Emission from ZnSe Films*, Solid State Phenomena **78-79** (2001) 89-94.

62. Mitsui, T. and N. Yamamoto, *Distribution of Cathodoluminescence in Triple Quantum Well of ZnCdSe/ZnSe*, Japanese Journal of Applied Physics **36** (1997) 2136-2139.

63.   Mitsui, T. and N. Yamamoto, *Cathodoluminescence Image of Defects and Luminescence Centers in ZnS/GaAs(100)*, Journal of Applied Physics **80** (1996) 6972-6979.

64.   Mitsui, T. and N. Yamamoto, *Influences of Interfacial Misfit Dislocations on Cathodoluminescence of ZnS/GaAs(001) Studied by Transmission Electron Microscopy.*, Japanese Journal of Applied Physics **39** (2000) 1172-1175.

65.   Mitsui, T., N. Yamamoto, K. Takemoto, and O. Nittono, *Cathodoluminescence and Electron Beam Irradiation Effect of Porous Silicon Studied by Transmission Electron Microscopy*, Japanese Journal of Applied Physics **33** (1994) L342-L344.

66.   Mitsui, T. and N. Yamamoto, *Deep Level Emission in ZnS Caused by Elecron Beam Irradiation Studied by Cathodoluminescence Measurement System*, Japanese Journal of Applied Physics **37** (1998) L1390-L1392.

67.   Ohno, Y. and S. Takeda, *Study of Electron-Irradiation-Induced Defects in GaP by In-situ Optical Spectroscopy in a Transmission Electron Microscope.*, Journal of Electron Microscopy **45** (1996) 73-78.

68.   Ohno, Y., Y. Kawai, and S. Takeda, *Vacancy-Migration-Mediated Disordering in CuPt-Ordered (Ga,In)P Studied by In Situ Optical Spectroscopy in a Transmission Electron Microscope*, Physical Review B **59** (1999) 2694-2699.

69.   Ohno, Y. and S. Takeda, *Optical Properties of Anti-Phase Boundaries and Frenkel-Type Defects in CuPt-Ordered GaInP Studied by Optical Spectroscopy in a Transmission Electron Microscope*, Institute of Physics Conference Series **164** (1999) 175-178.

70.   Ohno, Y. and S. Takeda, *A New Apparatus for In Situ Photoluminescence Spectroscopy in a Transmission Electron Microscope.*, Review of Scientific Instruments **66** (1995) 4866-4869.

71.   Bailey, S.J., J.A. Eades, and J.M. Olson, *Cathodoluminescence Studies of $Ga_{(x)}In_{(1-x)}P$*, Institute of Physics Conference Series **100** (1989) 761-765.

72.   Furuya, K. and T. Saito, *Determination of Beam Affected Area and Degradation of Cathodoluminescnence in GaAs Induced by Focused Ion Beam Irradiation.*, Journal of Applied Physics **80** (1996) 1922-1924.

73.   Tanabe, T., S. Muto, and S. Tohtake, *Development of New TEM Specimen Holder for Cathodoluminescence Detection*, Journal of Electron Microscopy **515** (2002) 311-313.

74.   Gao, H.-J., G. Duscher, M. Kim, S.J. Pennycook, D. Kumar, K.G. Cho, and R.K. Singh, *Cathodoluminescent Properties at Nanometer Resolution Through Z-Contrast Scanning Transmission Electron Microscopy*, Applied Physics Letters **77** (2000) 594-596.

75.   Ohno, Y. and S. Takeda, *Analysis of Polarization by Means of Polarized Cathodoluminescence Spectroscopy in a TEM,* Journal of Electron Microscopy **51** (2002) 281-290.

76.   Grillo, V., A. Genseki, N. Yamamoto, and Y. Watanabe, *Characterisation of Ultrathin InAs Quantum Wells by TEM-Cathodoluminescence and TEM Techniques,* Surface and Interface Analysis **35** (2003) 40-44.

77.   Remmele, T., M. Albrecht, H.P. Strunk, A.T. Blumenau, M.I. Heggie, J. Elsner, T. Frauenheim, H.P.D. Schenk, and P. Gibart, *Core Structure of Dislocations in GaN Revealed by Transmission Electron Microscopy,* Institute of Physics Conference Series **169** (2001) 323-326.

78.   Albrecht, M., H.P. Strunk, J.L. Weyher, I. Grzegory, S. Porowski, and T. Wosinski, *Carrier Recombination at Single Dislocations in GaN Measured by Cathodoluminescence in a Transmission Electron Microscope,* Journal of Applied Physics **92** (2002) 2000-2005.

79.   Albrecht, M., V. Grillo, J. Borysiuk, T. Remmele, H.P. Strunk, T. Walther, W. Mader, P. Prystawko, M. Leszczynski, I. Grzegory, and S. Porowski, *Correlating Compositional, Structural and Optical Properties of InGaN Quantum Wells by Transmission Electron Microscopy,* Institute of Physics Conference Series **169** (2001) 267-272.

General Properties of Nitrides

3.1 Crystal Structure of Nitrides

The $Al_xIn_yGa_{1-x-y}N$ quaternary system offers the possibility of continuously variable alloying to obtain a bandgap in the range 1.9 to 6.2eV as can be seen in Figure 3.1. The variation in lattice parameters and thermal expansion coefficients between the three binary alloys complicates the fabrication of structures and devices and has a significant effect on the properties and structure of the resultant alloys.

Under ambient conditions the wurtzite lattice is thermodynamically stable for AlN, GaN and InN. In the ideal wurtzite structure this consists of two interpenetrating hexagonal close-packed (HCP) sublattices offset along the c-axis by 5/8 of the unit cell height. The zincblende form can be grown on cubic substrates such as Si, MgO and GaAs, and takes the structure of two interpenetrating face-centred cubic sublattices offset by a quarter of the distance along a body diagonal. In both cases each group III atom is co-ordinated by four nitrogen atoms and vice versa. In the wurtzite form the stacking sequence of (0001) planes is ABABAB, whilst in the zincblende lattice the stacking sequence of (111) planes is ABCABCABC.
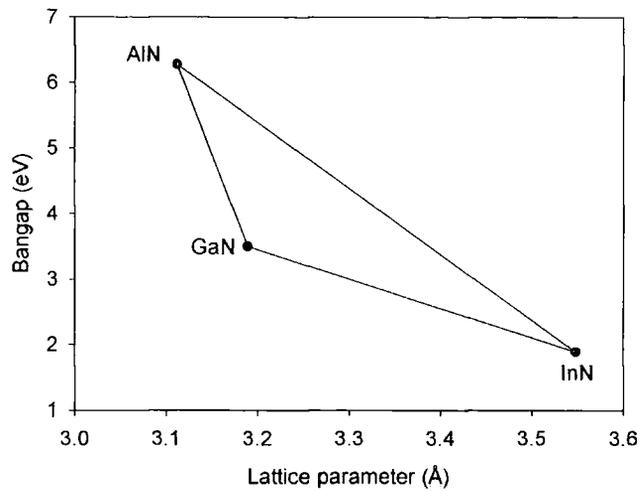
Figure 3.1: Bandgap and lattice parameter (hexagonal plane) for the wurtzite form of the binary alloys AlN, GaN and InN.

Wurtzite GaN exhibits both a spontaneous and piezoelectric polarisation along the <0001> directions [1-3]. The spontaneous polarisation is the polarisation at zero strain, the difference in this polarisation being much larger in $Al_xGa_{1-x}N$/GaN than in $In_xGa_{1-x}N$/GaN heterostructures [4]. Due to the small difference in spontaneous polarisation between InN and GaN the piezoelectric polarisation is the dominant factor at GaN/$In_xGa_{1-x}N$ interfaces. The piezoelectric polarisation is determined by lattice mismatch strain and thermal strain from the difference in thermal expansion coefficients. A consequence of this for the growth of $In_xGa_{1-x}N$ epitaxial layers on GaN is that increasing the In mole fraction increases the piezoelectric field due to increased lattice mismatch strain.

3.2 Epitaxy

Epitaxial growth is an established technique for the growth of crystalline thin films. It has the advantage of allowing the combination of different materials to create heterostructures, and is an efficient way of growing devices with a large surface area [5]. In general terms epitaxy is the oriented growth of a crystalline material on the single crystal surface of a different material [6]. Due to difficulties in the growth of bulk single crystals of the group III nitrides foreign substrates need to be used for nitride epitaxy. Ideally such a substrate should be closely

matched to the lattice spacing and thermal expansion coefficients of the material to be grown. A lack of suitable substrates meeting these requirements is a cause of many of the problems of Group III nitride epitaxial growth. Despite this GaN has been successfully grown on a wide range of substrates including sapphire, ZnO, 6H-SiC, Si, GaAs and MgO [7, 8]. The epitaxial layers investigated in this work were grown on sapphire and γ-LiAlO₂ substrates which are briefly described below.

Sapphire. Sapphire is composed of HCP planes of oxygen intercalated with HCP planes of aluminium. The aluminium planes have vacancies on one third of the sites so that each Al atom is surrounded by six oxygen atoms, and each oxygen atom is surrounded by four aluminium atoms. The lattice mismatch between the GaN basal plane and the sapphire basal plane is 13.8%. Despite this large mismatch growth of GaN in the (0001) direction on the sapphire basal plane is the most popular choice of orientation and substrate. This is in part due to the availability of low price, large wafers of good quality sapphire. Sapphire's high temperature stability is also an inportant factor. However, the growth of GaN layers directly on to sapphire results in very poor quality films unsuitable for device fabrication. This was overcome by the use of AlN [9] or GaN [10] buffer layers grown at low temperature. After deposition of the nucleation layer the temperature is then elevated to allow the semi-amorphous buffer layer to crystallise and provide a closer matched epitaxial system for GaN growth. Growth of the main GaN layer is initiated by the formation of hexagonal islands which form on the buffer layer and grow laterally until they coalesce.

γ-LiAlO₂. The (100) face of γ-LiAlO₂ is an attractive substrate for the epitaxial growth of (1-100) M-plane GaN with a misfit of 1.7% in the [001]$_{LiAlO2}$‖[11-20]$_{GaN}$ direction and 0.3% in the [010]$_{LiAlO2}$‖[0001]$_{GaN}$ direction. Growth of M-plane GaN was initially hampered by a lack of high quality γ-LiAlO₂ substrates [11-13]. However, with improved substrates the successful growth of M-plane GaN has recently been achieved [14-16].

3.3 Doping

Nominally undoped GaN is generally n-type. This conductivity is often attributed to nitrogen vacancies shown to be shallow donors in InN and GaN [17]. Intentional n-type doping in GaN is often achieved with Si [18]. Si substitutes Ga

in the lattice providing a loosely bound electron which is free to enter the conduction band. P-type doping in GaN has been demonstrated using Mg. Initially Mg doped GaN was found to be highly resistive. However, Mg doped GaN can be activated by low energy electron beam irradiation (LEEBI) [19] or annealing [20]. A possible mechanism for this activation process is the breaking down of a complex formed between Mg and H in Mg doped films.

3.4 Nitride Growth

Techniques such as hydride vapour phase epitaxy (HVPE), molecular beam epitaxy (MBE) and metalorganic vapour phase epitaxy (MOVPE) are used for the growth of epitaxial films. The techniques of MOVPE on a sapphire substrate [21] and plasma assisted molecular beam epitaxy (PAMBE) on a γ-LiAlO$_2$ substrate [16] used for the growth of epilayers examined in this work, are now briefly discussed.

MOVPE. The group three precursors for MOVPE growth are trimethylgallium and trimethylindium. The nitrogen precursor is ammonia. Prior to growth the substrate is annealed at high temperature (>1000°C) in an ammonia ambient forming an AlN monolayer. The substrate is then cooled to 500-800°C for the growth of a thin (<50nm) GaN nucleation layer. The temperature is then increased to 800-1200°C for growth of the main GaN layer. In$_x$Ga$_{1-x}$N growth requires a lower growth temperature of around 800°C since In will evaporate at higher temperatures. N-type doping with silicon or germanium in MOVPE is achieved with silane (SiH$_4$) or germane (GeH$_4$). P-type doping with magnesium is performed with bis-cyclopentadienyl magnesium (Cp$_2$Mg) or bis-methlycyclopentadienyl magnesium (MCp$_2$Mg).

PAMBE. Molecular nitrogen does not chemisorb on GaN at MBE growth temperatures (550-800°C), therefore atomic nitrogen is created by passing molecular nitrogen through an electron cyclotron resonance (ECR) or radio-frequency (RF) plasma source. A beam of Ga atoms is directed onto the heated substrate and nucleates there with the atomic nitrogen. Doping is achieved by evaporating Mg or Si during layer growth.

3.5 Structural Defects and Materials Performance

The structural quality of GaN epitaxial films is of importance since extended defects may reduce carrier lifetimes and consequently device efficiencies. Dislocation densities of the order of 10^{10}cm^{-2} are common in GaN epitaxial layers used in commercially available In$_x$Ga$_{1-x}$N QW LEDs [22]. Since dislocation densities of the order of 10^3cm^{-2} adversely affect the efficiency of GaAs devices the cause of this unexpected efficiency in In$_x$Ga$_{1-x}$N/GaN devices is of interest. This section contains reviews of the extended defects found in MOVPE and MBE grown GaN and a discussion of recombination mechanisms in In$_x$Ga$_{1-x}$N QWs.

Threading Dislocations. These are the dominant extended defects in c-plane, MOVPE grown GaN with densities of the order of 10^{10}cm^{-2}, whereas in M-plane MBE grown GaN the threading dislocation density is less than 8×10^8cm^{-2} [16]. Edge (**b**=1/3<2-1-10>), screw (**b**=<0001>) and mixed (**b**=1/3<11-23>) type dislocations are found in GaN epilayers and have been shown to be sources of non-radiative recombination in wurtzite GaN [23-25]. The role of threading dislocations in GaN is further discussed in Section 8.4.1.

Stacking Faults. The dominant defects in M-plane, MBE grown GaN are intrinsic, I$_2$, basal plane stacking faults [16, 26]. Low temperature (4K) PL spectra from these layers were dominated by a peak at 3.356eV. This luminescence was shown to be localised at regions of surface corrugation which were believed to have a high density of stacking faults [16]. The I$_2$ stacking fault introduces a thin layer of face-centred cubic material into the crystal. This cubic layer is calculated to form a type II QW where captured electrons can form excitons with holes attracted through the Coulomb potential [27]. The emission energy from recombination across this well was calculated to be 3.4eV and was considered to account for the observed stacking fault luminescence. However, the spontaneous polarisation of the wurtzite matrix along the (0001) direction was not taken into account in this calculation. Allowing for the spontaneous polarisation revealed a triangular potential [16]. The relationship between stacking faults and luminescence at 3.3-3.35eV is investigated in Section 8.5.

Inversion Domains. GaN has a polar asymmetry in the (0001) direction with the [0001] direction defined as the direction from the N terminated plane to the Ga terminated plane. Inversion domains are regions where the polarity is

inverted to that of the bulk matrix. These domains are thought to be nucleated at AlN sites formed on the sapphire surface during nitridation of the substrate [28, 29]. There is no evidence of significant strain or states within the bandgap associated with inversion domains [30, 31].

Nanopipes. Micro or nanopipes are hollow tubes, typically 5-25nm in diameter propagating in the [0001] direction in c-plane GaN [32]. Nanopipes are thought to result from oxygen contamination of the {10-10} island side walls preventing coalescence of the GaN layer [33]. A possible source for this contamination is migration of oxygen atoms from sapphire substrates. This is consistent with reports of higher nanopipe densities in high temperature MOVPE grown GaN than in lower temperature MBE material using GaAs and GaP substrates [29].

$In_xGa_{1-x}N$ QWs. A possible explanation for the surprising efficiency of $In_xGa_{1-x}N$ QW based light emitting devices is exciton localisation [34, 35] in the wells limiting the non-radiative effects of dislocations. A number of mechanisms for this localisation of carriers have been proposed.

It has been postulated that lattice mismatch induced strain causes a piezoelectric field in the QW lowering the energy levels and introducing a spatial separation of the electron and hole wavefunctions. This model may account for an observed red-shift of emission and increase in luminescence decay times with increasing well width [36]. Martin et al [37] consider this effect on a homogeneous QW and conclude that the observed long wavelength emission cannot be solely accounted for by the action of the piezoelectric field. They consider an additional effect due to InN-GaN segregation to be necessary to account for the experimental observations.

A number of authors attribute localisation effects to perturbations in the QW depth caused by fluctuations in the In content of the well as a result of phase separation [38]. Narukawa et al [39] used energy dispersive x-ray microanalysis to show that inhomogeneous contrast from $In_xGa_{1-x}N$ QWs imaged with cross-sectional TEM [34] corresponds with fluctuations in In content. Radiative recombination within this structure was attributed to excitons localised at In-rich regions of the QW. O'Donnell et al [40, 41] argue that these In-rich regions are actually nearly pure InN quantum dots. This explanation of In clustering as an intrinsic property of the $In_xGa_{1-x}N$ alloy is supported by Chichibu *et al* [42] with

analysis of bulk cubic $In_{0.1}Ga_{0.9}N$, which does not exhibit a polarisation field, showing similar optical properties to wurtzite $In_xGa_{1-x}N$ QWs.

Contradictory evidence to the In clustering model is given by Albrecht *et al* [43]. Using STEM-CL and energy filtered TEM of $In_xGa_{1-x}N$ QWs in cross-section they show that the optical properties of the QWs are not influenced by In segregation on a nanometre scale. These results are best explained as an effect intrinsic to the $In_xGa_{1-x}N$ alloy due to hole localisation at the In atom. Bellaiche and Zunger [44] and Bellaiche *et al* [45] calculate that alloying of In with GaN leads to localisation of hole states accounting for the observed localisation effects in $In_xGa_{1-x}N$.

3.6 References

1. McKie, D. and C. McKie, *Crystalline Solids*, (Thomas Nelson and Sons Ltd., London, 1974).

2. Bernardini, F., V. Fiorentini, and D. Vanderbilt, *Spontaneous Polarization and Piezoelectric Constants of III-V Nitrides*, Physical Review B **56** (1997) R10024-R10027.

3. Amano, H., S. Kamiyama, and I. Akasaki, *Growth Optimisation of Low-Dimensional Nitrides by Metalorganic Vapour Phase Epitaxy and Dislocation Control*, in *Low-Dimensional Nitride Semiconductors*, B. Gil, (Oxford Univeristy Press, Oxford, 2002).

4. Morkoc, H., *Nitride Semiconductors and Devices*, (Springer Verlag, Heidelberg, 1999).

5. Trampert, A., *Heteroepitaxy of Dissimiliar Materials: Effect of Interface Structure on Strain and Defect Formation*, Physica E **13** (2002) 1119-1125.

6. Markov, I.V., *Crystal Growth for Beginners*, (World Scientific, Singapore, 1995).

7. Popovici, G., H. Morkoc, and S.N. Mohammad, *Deposition and Properties of Group III Nitrides by Molecular Beam Epitaxy*, in *Group III Nitride Semiconductor Compounds*, B. Gil, (Oxford University Press, Oxford, 1998).

8. Briot, O., *MOVPE Growth of Nitrides*, in *Group III Nitride Semiconductor Compounds*, B. Gil, (Oxford University Press, Oxford, 1998).

9. Akasaki, I., H. Amano, Y. Koide, K. Hiramatsu, and N. Sawaki, *Effects of AlN Buffer Layer on Crystallographic Structure and on Electrical and Optical Properties of GaN and $Ga_{(1-x)}Al_{(x)}N$ (0<x<0.4) Films Grown on Sapphire Substrate by MOVPE*, Journal of Crystal Growth **98** (1989) 209-219.

10. Nakamura, S., *GaN Growth Using GaN Buffer Layer*, Japanese Journal of Applied Physics **30** (1991) L1705-L1707.

11. Hellman, E.S., Z. Liliental-Weber, and D.N.E. Buchanan, *Epitaxial Growth and Orientation of GaN on (100) γ-LiAlO2*, MRS Internet Journal of Nitride Semiconductor Research **2** (1997) 30.

12. Ke, X., X. Jun, D. Peizhen, Z. Yongzong, Z. Guoqing, Q. Rongsheng, and F. Zujie, *γ-LiAlO2 Single Crystal: A Novel Substrate for GaN Epitaxy*, Journal of Crystal Growth **193** (1998) 127-132.

13. Waltereit, P., O. Brandt, and K.H. Ploog, *Violet and Blue Emitting (In,Ga)N/GaN Multiple Quantum Wells Grown on γ-LiAlO2(100) by Radio Frequency Plasma-Assisted Molecular Beam Epitaxy*, Applied Physics Letters **75** (1999) 2029-2031.

14. Xu, K., J. Xu, P. Deng, R. Qiu, and Z. Fang, *MOCVD Growth of GaN on LiAlO₂(100) Substrates,* Physica Status Solidi A **176** (1999) 589-593.

15. Waltereit, P., O. Brandt, M. Ramsteiner, A. Trampert, H.T. Grahn, J. Menniger, M. Reiche, R. Uecker, P. Reiche, and K.H. Ploog, *Growth of M-Plane GaN(1-100): A Way to Evade Electrical Polarization in Nitrides,* Physica Status Solidi A **180** (2000) 133-138.

16. Sun, Y.J., O. Brandt, U. Jahn, T.Y. Liu, A. Trampert, S. Cronenberg, S. Dhar, and K.H. Ploog, *Impact of Nucleation Conditions on the Structural and Optical Properties of M-Plane GaN(1-100) Grown on γ-LiAlO2,* Journal of Applied Physics **92** (2002) 5714-5719.

17. Jenkins, D.W., J.D. Dow, and M.-H. Tsai, *N Vacancies in Al₍ₓ₎Ga₍₁₋ₓ₎N,* Journal of Applied Physics **72** (1992) 4130-4133.

18. Koide, N., H. Kato, M. Sassa, S. Yamasaki, K. Manabe, M. Hashimoto, H. Amano, K. Hiramatsu, and I. Akasaki, *Doping of GaN with Si and Properties of Blue m/i/n/n⁺ GaN LED with Si-Doped n⁺ Layer by MOVPE,* Journal of Crystal Growth **115** (1991) 639-642.

19. Amano, H., M. Kito, K. Hiramatsu, and I. Akasaki, *P-Type Conduction in Mg-Doped GaN Treated with Low-Energy Electron Beam Irradiation (LEEBI),* Japanese Journal of Applied Physics **28** (1989) L2112-L2114.

20. Nakamura, S., T. Mukai, M. Senoh, and N. Iwasa, *Thermal Annealing Effects on P-Type Mg-Doped GaN Films,* Japanese Journal of Applied Physics **31** (1992) L139-L142.

21. Deatcher, C.J., C. Liu, S. Pereira, M. Lada, A.G. Cullis, Y.J. Sun, O. Brandt, and I.M. Watson, *In Situ Optical Reflectometry Applied to Growth of Indium Gallium Nitride Epilayers and Multi Quantum Well Structures,* Semiconductor Science and Technology **18** (2003) 212-218.

22. Lester, S.D., F.A. Ponce, M.G. Craford, and D.A. Steigerwald, *High Dislocation Densities in High Efficiency GaN-Based Light-Emitting Diodes,* Applied Physics Letters **66** (1995) 1249-1251.

23. Rosner, S.J., E.C. Carr, M.J. Ludowise, G. Girolami, and H.I. Erikson, *Correlation of Cathodoluminescence Inhomogeneity With Microstructural Defects in Epitaxial GaN Grown by Metalorganic Chemical-Vapor Deposition.,* Applied Physics Letters **70** (1997) 420-422.

24. Sugahara, T., H. Sato, M. Hao, Y. Naoi, S. Kurai, S. Tottori, K. Yamashita, K. Nishino, L.T. Romano, and S. Sakai, *Direct Evidence that Dislocations are Non-Radiative Recombination Centers in GaN,* Japanese Journal of Applied Physics **37** (1998) L398-L400.

25. Cherns, D., S.J. Henley, and F.A. Ponce, *Edge and Screw Dislocations as Nonradiative Centers in InGaN/GaN Quantum Well Luminescence,* Applied Physics Letters **78** (2001) 2691-2693.

26. Trampert, A., T.Y. Liu, and K.H. Ploog, *Defect Structure of Thin GaN Epilayers: M-Plane Versus C-Plane Growth,* Proceedings of the Fourth Symposium on Non-Stoichiometric III-V Compounds (2002) 111-118.

27. Rebane, Y.T., Y.G. Shreter, and M. Albrecht, *Stacking Faults as Quantum Wells for Excitons in Wurtzite GaN,* Physica Status Solidi A **164** (1997) 141-144.

28. Rouviere, J.-L., M. Arlery, and A. Bourret, *Structural Characterisation of GaN Layers: Influence of Polarity and Strain Release,* Institute of Physics Conference Series **157** (1997) 173-182.

29. Brown, P.D., *TEM Assessment of GaN Epitaxial Growth,* Journal of Crystal Growth **210** (2000) 143-150.

30. Ponce, F.A., *Structural Defects and Materials Performance of the III-V Nitrides,* in *Group III Nitride Semiconductor Compounds,* B. Gil, (Oxford University Press, Oxford, 1998).

31. Northrup, J.E., J. Neugebauer, and L.T. Romano, *Inversion Domain and Stacking Mismatch Boundaries in GaN,* Physical Review Letters **77** (1996) 103-106.

32. Cherns, D., W.T. Young, M.A. Saunders, F.A. Ponce, and S. Nakamura, *The Analysis of Nanopipes and Inversion Domains in GaN Thin Films,* Institute of Physics Conference Series **157** (1997) 187-190.

33. Elsner, J., R. Jones, M. Haugk, R. Gutierrez, T. Frauenheim, M.I. Heggie, S. Oberg, and P.R. Briddon, *Effect of Oxygen on the Growth of (10-10) GaN Surfaces: The Formation of Nanopipes,* Applied Physics Letters **73** (1998) 3530-3532.

34. Chichibu, S., T. Azuhata, T. Sota, and S. Nakamura, *Spontaneous Emission of Localized Excitons in InGaN Single and Multiquantum Well Structures,* Applied Physics Letters **69** (1996) 4188-4190.

35. Kanie, H., N. Tsukamoto, H. Koami, T. Kawano, and T. Totsuka, *Localised Luminescence Centres of InGaN,* Journal of Crystal Growth **189-190** (1998) 52-56.

36. Im, J.S., H. Kollmer, J. Off, A. Sohmer, F. Scholz, and A. Hangleiter, *Reduction of Oscillator Strength Due to Piezoelectric Fields in GaN/AlGaN Quantum Wells,* Physical Review B **57** (1998) R9435-R9438.

37. Martin, R.W., P.R. Edwards, R. Pecharroman-Gallego, C. Liu, C.J. Deatcher, I.M. Watson, and K.P. O'Donnell, *Light Emission Ranging From Blue to Red From a Series of InGaN/GaN Single Quantum Wells,* Journal of Physics D: Applied Physics **35** (2002) 604-608.

38. Ho, I.-h. and G.B. Stringfellow, *Solid Phase Immiscibility in GaInN,* Applied Physics Letters **69** (1996) 2701-2703.

39.   Narukawa, Y., Y. Kawakami, M. Funato, S. Fujita, S. Fujita, and S. Nakamura, *Role of Self-Formed InGaN Quantum Dots for Exciton Localization in the Purple Laser Diode Emitting at 420nm.,* Applied Physics Letters **70** (1997) 981-983.

40.   O'Donnell, K.P., R.W. Martin, and P.G. Middleton, *Origin of Luminescence from InGaN Diodes,* Physical Review Letters **82** (1999) 237-240.

41.   O'Donnell, K.P., R.W. Martin, C. Trager-Cowan, M.E. White, K. Esona, C. Deatcher, P.G. Middleton, K. Jacobs, W.V. Stricht, C. Merlet, B. Gil, A. Vantomme, and J.F.W. Mosselmans, *The Dependence of the Optical Energies on InGaN Composition,* Materials Science & Engineering B **82** (2001) 194-196.

42.   Chichibu, S.F., T. Azuhata, H. Okumura, A. Tackeuchi, T. Sota, and T. Mukai, *Localized Exciton Dynamics in InGaN Quantum Well Structures,* Applied Surface Science **190** (2002) 330-338.

43.   Albrecht, M., V. Grillo, J. Borysiuk, T. Remmele, H.P. Strunk, T. Walther, W. Mader, P. Prystawko, M. Leszczynski, I. Grzegory, and S. Porowski, *Correlating Compositional, Structural and Optical Properties of InGaN Quantum Wells by Transmission Electron Microscopy,* Institute of Physics Conference Series **169** (2001) 267-272.

44.   Bellaiche, L. and A. Zunger, *Effects of Atomic Short-Range Order on the Electronic and Optical Properties of GaAsN, GaInN, and GaInAs Alloys,* Physical Review B **57** (1998) 4425-4431.

45.   Bellaiche, L., T. Mattila, L.-W. Wang, S.-H. Wei, and A. Zunger, *Resonant Hole Localization and Anomalous Optical Bowing in InGaN Alloys,* Applied Physics Letters **74** (1999) 1842-1844.

Chapter 4

Experimental Techniques

4.1 Introduction

In this chapter the techniques used for the growth of samples and the preparation of cross-sectional and plan-view TEM foils from these are described. The standard characterisation techniques of SEM and TEM used in this study are briefly outlined, whilst the experimental techniques specific to TEM-CL are discussed in greater detail. However, to begin with, the details of the sample growth are outlined below.

4.2 Material Growth

Samples grown on two different epitaxial systems were investigated. $In_xGa_{1-x}N$ QW structures were grown on c-plane GaN/sapphire by MOVPE at the *Institute of Photonics, University of Strathclyde.* The technique of MOVPE is reviewed in Section 3.4. M-plane GaN epitaxial layers were grown on $LiAlO_2$ by PAMBE at the *Paul-Drude Institut in Berlin.* PAMBE is also reviewed in Section 3.4. Summary growth details and references to further information are given in Tables 6.1 and 8.1.

4.3 Sample Preparation

Cross-sectional TEM foil preparation by mechanical polishing followed by Ar^+ milling to perforation is a routine operation and is reviewed by a number of authors [1-6]. In this study TEM foils were prepared in cross-section and plan view orientations. The techniques used are outlined below.

Cross-sectional TEM foil preparation. Slices of sapphire/GaN wafers were sandwiched together with the epitaxial layers together using silicon as a packing material creating a $Si/Al_2O_3/GaN/GaN/Al_2O_3/Si$ structure. *M-Bond 610* epoxy was used as an adhesive and was cured at 175°C for 90 minutes. This sandwich was mechanically polished from both sides using a *Logitech PM2* polishing machine with 17µm SiC powder to a thickness of ~1mm. A *Testbourne Model 360* micro-drill with 17µm SiC slurry to assist cutting was then used to cut 3.05mm discs from the 1mm thick sandwich. A 3.05mm disc was then mounted on to the sample stub of a *Gatan* disc grinder. The emergent face was then polished with *Buehler Metadi Supreme* diamond suspension of decreasing roughness (15 µm, 5 µm and 1 µm) and appropriate *Struers* polishing pads using an arrangement where the Gatan disc grinder was mounted on a *Logitech PR2* mechanical polisher. This arrangement is shown in Figure 4.1. The advantage of mounting the *Gatan* disc grinder on a mechanical polisher is that the pressure on the sample is constant. The polisher can be operated on a timer so the required amount of material can be exposed using the screw thread on the *Gatan* grinder and the polisher can be left unattended. The *Gatan* grinder moves inwards towards the centre of the polishing pad as the sample becomes level with the bottom surface of the *Gatan* grinder. When changing the grade of diamond suspension care was taken to ensure all the components were thoroughly cleaned and a new polishing pad was fitted.
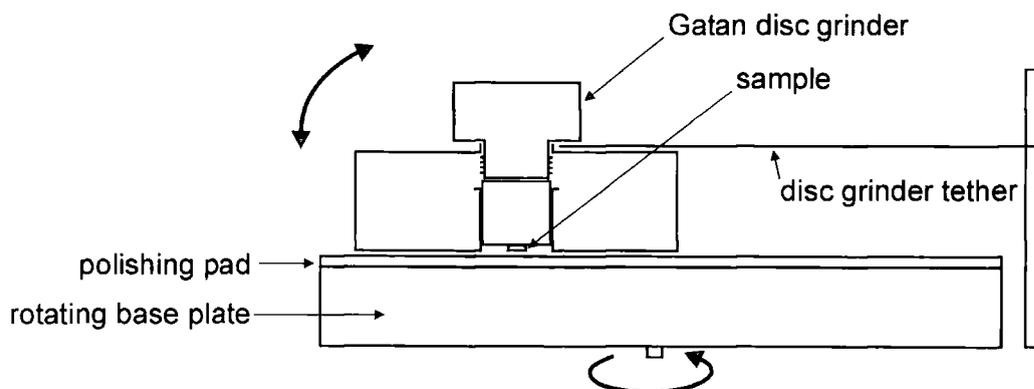
Figure 4.1: **Arrangement for the mounting of a *Gatan* disc grinder on a *Logitech* PM2 mechanical polisher.**

Once the exposed side was polished to a 1μm finish it was cleaned with isopropyl alcohol and a Cu or Au support ring was glued to the sample using a room temperature curing epoxy. Care was taken to avoid any contamination of the sample surface with epoxy and to ensure the support ring lay flat. The sample was then remounted on the Gatan grinder sample stub with the support ring in contact with the metal stub. Mild pressure was applied during mounting so that the sample lay flat. The sample was then polished until it was <50μm thick (not including the thickness of the support ring). The diamond suspension roughness was reduced from 15μm to 1μm as the target thickness was approached. The sample was then removed and degreased in trichloroethane.

Following degreasing the sample was mounted in an *Ion Tech 800 Series* Ar⁺ miller operating at 4kV. The sample stage in the Ar⁺ miller was cooled with flowing liquid nitrogen and rotated using a PC controlled *Atom Tech 820T Series* Stepper Motor Drive with an *RS 4-Phase Unipolar Stepper Motor Drive Board 332-098*. A simple program was written to increase the speed of rotation for the period that the glue-line of the sample was parallel to the ion beam within an angular range of ±10°. This alleviated preferential sputtering of the epitaxial layer. The angle of incidence of the Ar+ beam was reduced from 30° to 5° as perforation was approached.

Plan view TEM foil preparation. A Cu or Au support ring was glued on the epilayer side of the sample. A 3.05mm disc was then drilled from the sample encompassing the support disc. The sample disc was then mounted, supporting disc upwards, on a Gatan grinder stub. The sample was then polished to a

thickness of <50μm, removed and mounted in the Ar⁺ thinner using the techniques described for cross-sectional samples. Ar+ milling was then performed from the substrate side only until perforation.

4.4 Scanning Electron Microscopy

Scanning electron microscopy (SEM) is a non-destructive method of investigating the surface morphology of materials. In its most basic mode a SEM operates by scanning a focused beam of electrons across an area of the sample and building up an image from backscattered or secondary electrons. The accelerating voltage is typically in the region of 1-40kV. SEM in this study was performed on a *JEOL JSM-IC848* operating in secondary electron mode with an accelerating voltage of 20kV. Detailed SEM operating procedures can be found in references [7-9]. However a brief description of backscattered electron and secondary electron modes follows.

Backscattered Electron Mode. Backscattered electrons are primary electrons which have been elastically scattered (through single or multiple scattering events) by Coulombic interactions with atomic nuclei in the target so that they re-emerge from the target sample. Since the probability of scatter by the atomic nuclei is Coulombic in nature the rate of electron backscatter contains compositional information.

Secondary Electron Mode. Secondary electrons typically have energies below 50eV and are generated close to the sample surface. They are generated through the interaction of the primary beam with loosely bound conduction electrons. Secondary electrons are commonly used for surface topology studies.

4.5 Transmission Electron Microscopy

The use of transmission electron microscopy (TEM) for the study of the structure and defects in semiconductors is a well established technique and is described in detail in a number of texts [1, 5, 8, 10-14]. In this study TEM was performed on a *JEOL 200CX* with a *JEOL EM-ASID3D2* scanning unit operating at 80-120kV. TEM was used for bright field microscopy, dark field microscopy, selected area diffraction and STEM which are described briefly below;

Selected Area Diffraction (SAD). This technique is used to select a specific area of the specimen to contribute to the diffraction pattern by inserting an aperture into the image plane of the objective lens.

Bright Field (BF) Microscopy. A bright field image is formed if the central, undeviated beam in the SAD pattern is selected by inserting the objective aperture into the back focal plane of the objective lens.

Dark Field (DF) Microscopy. A dark field image may be formed by selecting a Bragg reflected beam with the objective aperture. This may be done by displacing the objective aperture off-axis or by centering the objective aperture on axis and tilting the beam to form a centred dark field (CDF) image.

Scanning Transmission Electron Microscopy (STEM). In STEM operation a fine electron probe (10nm) is used to scan an area of the sample. The probe scans parallel to the optic axis and is controlled by two pairs of scan coils between the second condenser lens and the upper objective polepiece. The signal from an on-axis BF scintillator-photomultiplier detector is synchronized with the scan coils to form an image.
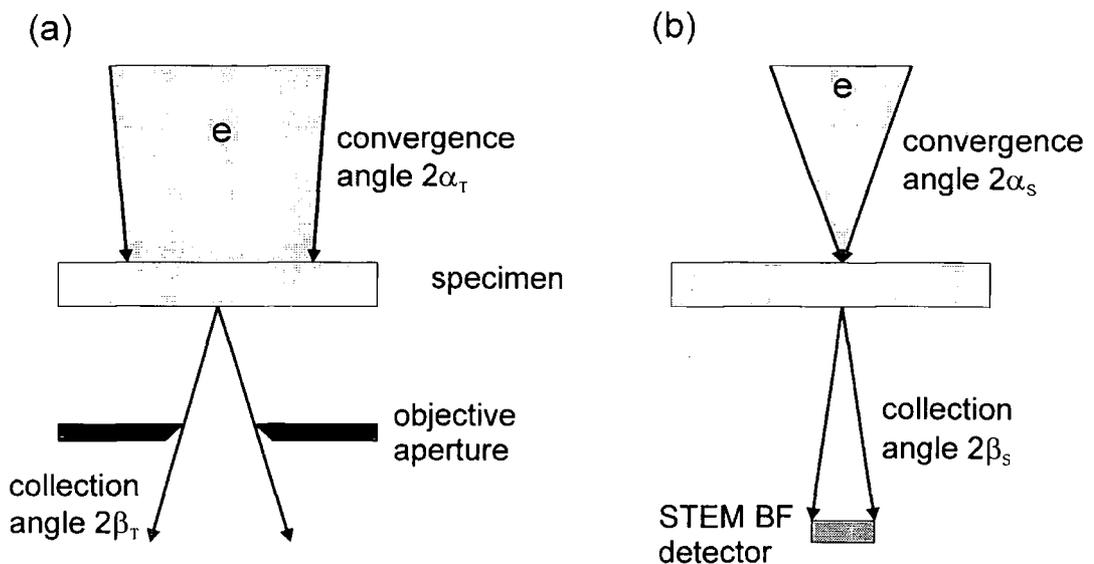

Figure 4.2: Beam convergence and divergence angles in (a) TEM, and (b) STEM [12]

The diffraction contrast in STEM mode is typically much poorer than in TEM. This can be demonstrated with the aid of Figure 4.2 where the TEM convergence semi-angle is defined as α_T, and the objective aperture collection

semiangle is β_T. The equivalent STEM angles are the beam-convergence angle α_S, and STEM detector collection angle β_S. The principle of reciprocity states that if

$$\alpha_S = \beta_T \qquad (4.1)$$

and

$$\alpha_T = \beta_S \qquad (4.2)$$

then the diffraction conditions in STEM will be identical to those in TEM. Since β_T is typically similar to α_S Equation 4.1 is satisfied. However, as a parallel beam is necessary for strong diffraction contrast in TEM, α_T needs to be small. To satisfy Equation 4.2 it is necessary for β_S to be as small as possible for strong STEM diffraction contrast. As β_S is reduced the electron flux incident on the on-axis BF detector falls and the image becomes noisy. Therefore the amount of diffraction contrast achievable in STEM is a trade-off against image noise.

Calibration. Standard *Agar* ruled grids were used to calibrate the magnification in TEM and STEM. The camera-length was calibrated using an evaporated aluminium foil and the image rotation relative to the diffraction pattern was calibrated using the [001] direction of Molybdenum Oxide crystals.

4.6 TEM-CL

The TEM-CL collection system is an *Oxford Instruments[1] MonoCL2* controlled by the *LINK ISIS 300* system. The system consists of a CL collection mirror, 0.3m spectrometer, a Peltier cooled *Burle C31034* photomultiplier tube, *PA3* photoamplifier supply and stepper driver, and *ISIS 300* control system. The system and its characteristics are discussed in Chapter 5 and can be seen in Figure 4.3. The TEM-CL apparatus and experimental techniques used for recording CL spectra and performing panchromatic and monochromatic imaging are described below.

---

[1] Now trading as *Gatan* plc.

(a)　　　　　　　　(b)

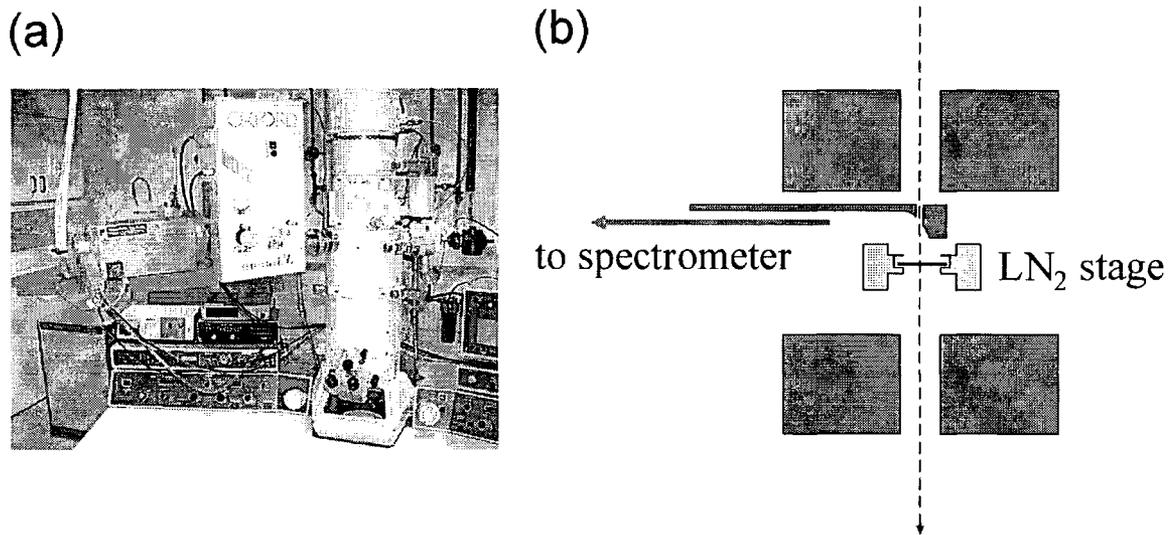to spectrometer　　　LN$_2$ stage

Figure 4.3: **(a) Photograph of *JEOL 200CX* with TEM-CL attachment, (b) diagram showing TEM-CL mirror in the collection position above the specimen holder.**

CL Collection Mirror. CL from the TEM foil is collected using the *Oxford CL302* collection system. This consists of a retractable paraboloidal aluminium mirror which collects and guides the CL either to the slits of the monochromator or directly on to the photomultiplier tube for panchromatic imaging. The collection efficiency for the mirror, as specified by the manufacturer, is 80%. However, as the light emission from a high refractive index material is not directionally uniform this collection efficiency is not necessarily applicable. This is discussed in greater detail in Section 5.4.2.

Low CL emission from thin films makes accurate positioning of the mirror critical. The mirror position is variable in all three dimensions. The mirror is inserted and retracted from the microscope column using a screw thread and can be varied in the directions normal to this using two positioning screws. As the focus of the mirror is 1mm below the bottom of the mirror and the sample is held in the sample holder 0.5-1mm below the top surface, the mirror has to be positioned very close to the sample holder without colliding with it. A preset mirror position is not practical as the vertical, z, position of the mirror varies with eucentric height and a misalignment of as little as 0.1mm can reduce the CL signal by an order of magnitude. Initial mirror positioning was done by illuminating an unused section of the specimen and positioning the mirror to optimise the signal. Care has to be taken to ensure that an increase in signal

due to ongoing cooling of the sample or a decrease due to beam degradation (see Chapter 6 for further discussion) does not disrupt optimisation.

TEM-CL LN₂ Specimen Holder. Due to the limited space available in the microscope pole piece and requirement for a 1mm mirror/specimen separation a specially designed specimen holder is used. The specimen holder is an *Oxford Instruments CT3500TR Tilt-Rotate Cryo-Transfer Holder.* The sample is held in a cradle in the specimen holder using a screwed ring to achieve a good thermal contact. The cradle is cooled by a short braid and a solid conduction rod from a nitrogen dewar. The specimen is rotated by a flexible line which is connected to a drive motor. This is controlled by an *Oxford Instruments Digital Tilt Indicator.* When the TEM-CL mirror is inserted the sample can be rotated. However the proximity of the mirror means tilting is not possible. Once inside the TEM the specimen holder can be filled with liquid nitrogen approximately fifteen minutes after the anti-contamination trap on the TEM has been cooled. The specimen temperature is monitored and controlled using an *Oxford Instruments ITC502 Temperature Controller.* The lowest temperature achievable is a nominal 90K. Once stabilised at this temperature experiments may be performed for around one hour without significant specimen drift or the need to refill the dewar.

Monochromator. The collected CL could be either directed undeviated into the aperture of the photomultiplier or dispersed using a 0.3 metre monochromator. The spectrometer was fitted with two 150 lines/mm gratings blazed for maximum transmission at 300 and 500nm. The spectral dispersion was 21.6nm/mm. Typically the monochromator entrance and exit slits were set between 0.5 and 1mm yielding a dispersion of 10.8-21.6nm.

Spectral Acquisition. The *LINK ISIS 300* control system allowed spectra to be recorded using the *PA3* photoamplifier supply and stepper driver with integration times ranging from 1ms to 10s. Spectra were recorded in CTEM, STEM, and STEM point illumination modes. The calibration and spectral response of the optical system are discussed in Chapter 5.

CL Imaging and Line-Scans. Panchromatic and monochromatic CL imaging was performed in STEM mode using the *LINK ISIS* control system. Images were recorded with resolutions of 128×100, 256×200, 512×400, and 1024×800 pixels. Dwell times between 100 and 12800 μs yielded a range of 1.5 seconds to ~3 hours for image acquisition. The onset of specimen drift limited acquisition times to forty minutes or less. A major limitation of STEM-CL imaging

was the short integration time at each pixel (limited to a maximum of 12800µs by the control software). This was particularly limiting for monochromatic imaging. However, by performing line-scans the integration times could be varied from 1 ms to 10s with 1 to 10000 data points along the line. Line-scans were set up by recording a STEM image and overlaying the required scan direction.

4.7 Image Analysis

A *Visual Basic* routine (listed in Appendix A2) was used to obtain numerical position/intensity data from greyscale bitmap images and hence to make vertical summations from noisy images of single layers.
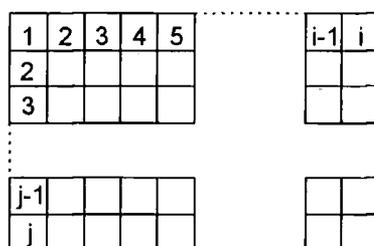
Figure 4.4:   **Pixel positions in a rectangular bitmap image.**

The operation of the program is represented in Figure 4.4 with each numbered square representing a pixel. A rectangular greyscale bitmap is loaded into memory in an *ixj* array where *i* is the image width in pixels and *j* is the image height in pixels. Each pixel has a numerical value associated with it ranging from 0 (black) to 256 or 2^8 (white). The matrix is then summed vertically and *i* numbers are saved to a file with each number equal to the sum of ith column.

4.8 References

1.   Hirsch, P.B., A. Howie, R.B. Nicholson, D.W. Pashley, and M.J. Whelan, *Electron Microscopy of Thin Crystals*, (Spottiswoode, Ballantyne & Co. Ltd., London and Colchester, 1965).

2.   Kay, D., *Techniques for Electron Microscopy*, (Blackwell, Oxford, 1965).

3.   Goodhew, P.J., *Specimen Preparation for Transmission Electron Microscopy of Materials*, (Oxford University Press, Oxford, 1984).

4.   Glauert, A.M., *Practical Methods in Electron Microscopy*, (North-Holland Publishing Company, Amsterdam, 1972).

5.   Williams, D.B. and C.B. Carter, *Transmission Electron Microscopy - Basics*, (Plenum Press, New York, 1996).

6.   Bravman, J.C., R.M. Anderson, and M.L. McDonald, *Specimen Preparation for Transmission Electron Microscopy of Materials*, (Materials Research Society, Pittsburgh, 1988).

7.   Goodhew, P.J. and F.J. Humphreys, *Electron Microscope and Analysis*, (Taylor and Francis, London, 1988).

8.   Chescoe, D. and P.J. Goodhew, *The Operation of Transmission and Scanning Electron Microscopes*, (Oxford University Press, Oxford, 1990).

9.   Goldstein, J.I., D.E. Newbury, P. Echlin, D.C. Joy, C. Fiori, and E. Lifshin, *Scanning Electron Microscopy and X-Ray Microanalysis*, (Plenum Press, New York, 1981).

10.   Reimer, L., *Transmission Electron Microscopy, Physics of Image Formation and Microanalysis*, (Springer-Verlag, Heidelberg, 1984).

11.   Williams, D.B. and C.B. Carter, *Transmission Electron Microscopy - Diffraction*, (Plenum Press, New York, 1996).

12.   Williams, D.B. and C.B. Carter, *Transmission Electron Microscopy - Imaging*, (Plenum Press, New York, 1996).

13.   Hirsch, P.B., *Topics in Electron Diffraction and Microscopy of Materials*, (Institute of Physics, Bristol, 1999).

14.   Amelinckx, S., R. Gevers, and J.V. Landuyt, *Diffraction and Imaging Techniques in Material Science, Volume I: Electron Microscopy*, (North-Holland Publishing Company, Amsterdam, 1978).

TEM-CL System and CL Generation

5.1 Introduction

In the first part of this chapter the calibration of the TEM-CL apparatus and characterisation of the instrument are reported. As TEM-CL is a non-standard technique brief descriptions of routine calibration operations, which may be of interest to other operators, have been included for completeness. In the second part of this chapter the resolution of STEM-CL is considered and thin film interference effects are discussed and investigated using computer models.

5.2 Calibration

5.2.1 Wavelength Calibration

The spectrometer wavelength calibration was performed using sodium and cadmium spectral lamps. This was performed in-situ by bringing the microscope column up to air, positioning the lamp close to a removable seal in the pole piece and inserting the CL mirror with no specimen holder present. The spectrometer calibration was fitted to the spectral lines with associated RMS fitting errors of

0.243nm for the grating blazed for maximum reflectance at 300nm and 0.707 for the 500nm blazed grating.

5.2.2 Wavelength Response

Spectra presented in this study have not been corrected for the relative attenuation of different wavelengths as light passes through the optical system. The manufacturer's standard 150 lines/mm, 500nm blaze grating was found to have poor transmittance below 400nm so a second grating, blazed at 300nm, was fitted. The products of the transmittance of these gratings and the photomultiplier based upon the manufacturer's specifications are shown in Figure 5.1.
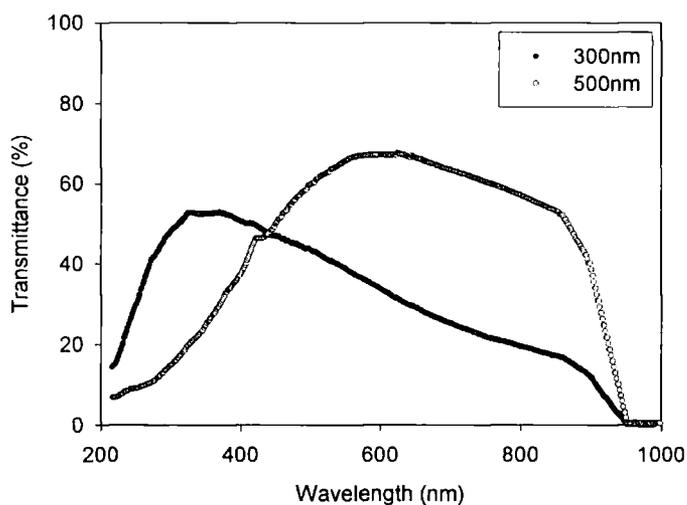
Figure 5.1: **TEM-CL system wavelength response curves for 150 lines/mm gratings blazed for peak reflectance at 300nm and 500nm.**

All lenses and light guides in the system are *Spectrosil B* quartz providing good uniformity in transmission across the optical range of the system.

5.2.3 Spectrometer Resolution

The maximum resolution of the optical system was investigated using a flake of ruby held within a slot grid. Intense CL emission was generated by illuminating the bulk ruby with a 100kV electron beam at a temperature of 100K. The resulting spectra can be seen in Figure 5.2(a) and (b).

(a)

(b)

Figure 5.2: **Spectra obtained from bulk ruby with a 100kV electron beam at 100K with nominal wavelength dispersions of (a) 4.32nm, 2.16nm and 1.06nm, and (b) 1.08nm.**

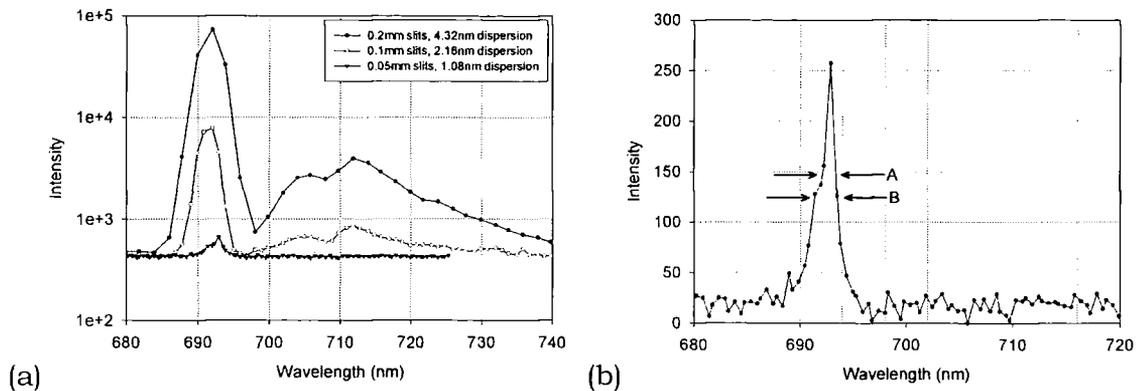Ruby has a characteristic doublet; R_1=6,942.3Å and R_2=6,927.4Å [1], as a result of chromium doping. Figure 5.2(a) demonstrates the effect of decreasing the monochromator entrance and exit slits. Halving the slit width from 0.2mm to 0.1mm results in an order of magnitude drop in signal and halving of the full width half maximum (FWHM). The highest resolution obtainable before no signal was detected was nominally 1.08nm (0.05mm slits). This can be seen in Figure 5.2(b) with dark noise and gun glow (see ahead to 5.2.4 for further details) removed. As can be seen this resolution is not high enough completely to resolve the ruby doublet, but a shoulder is visible (see A and B in Figure 5.2b). It is not possible to calculate an exact FWHM for the more intense peak at 693nm. However at the point A, where the peak broadens, it is possible to interpolate a FWHM of ~1nm which is in agreement with the nominal value.

The position of the ruby doublet peaks shown in Figure 5(b) at 692 and 693nm is 1nm below the literature values. However, this error is within the RMS fitting error of ~1nm for the 500nm blaze grating used and it should be noted that the literature values for ruby are for room temperature.

5.2.4 Hole Spectra and Dark Noise

As part of the system calibration process it was necessary to measure the PMT dark noise and record 'hole' spectra, with the electron beam on, but no sample loaded. Without cooling the PMT the dark noise would swamp all but the strongest signals; however cooling reduced the dark noise by several orders of

magnitude to around a 100 counts per second. The dark noise levels of the PMT were monitored periodically as they tended to increase slightly with time.

Hole spectra were investigated rigorously as light emission due to glow of the tungsten filament (gun glow) or CL emission from stray electrons were considered a possibility.

Figure 5.3(a) shows three spectra. The first is taken with no electron beam. The slight decrease in dark noise is due to ongoing cooling of the PMT. The two remaining spectra were taken with the beam passing through the hole in a TEM foil as shown in Figure 5.3(b). The spectrum taken with condenser aperture 3 (200µm diameter) has a higher level of background noise, but no spectral features, whilst the spectrum taken with condenser aperture 1 (400µm diameter) has a broad peak centred around 650nm. This peak may be due to light from the filament being measured, larger CL emission due to stray electrons striking the sides of the column, or some combination of the two.

(a)   (b)
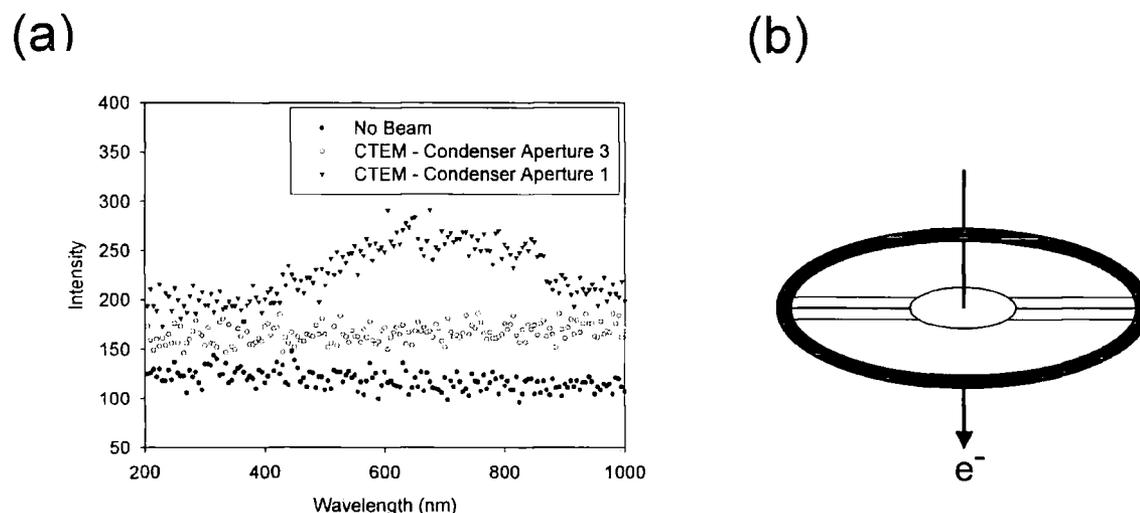
Figure 5.3:(a) Hole spectra taken with a 100kV CTEM beam and varying condenser aperture size, (b) schematic of electron beam passing through a hole in a TEM foil.

Figure 5.4 is taken under the same conditions as Figure 5.3, with the accelerating voltage varied and with a fixed condenser aperture. An increase in the accelerating voltage is seen to increase the level of recorded CL without changing the shape of the spectrum. This is consistent with increased filament emission at higher operating voltages and is borne out by beam current measurements taken with a Faraday cup (see Table 6.2).
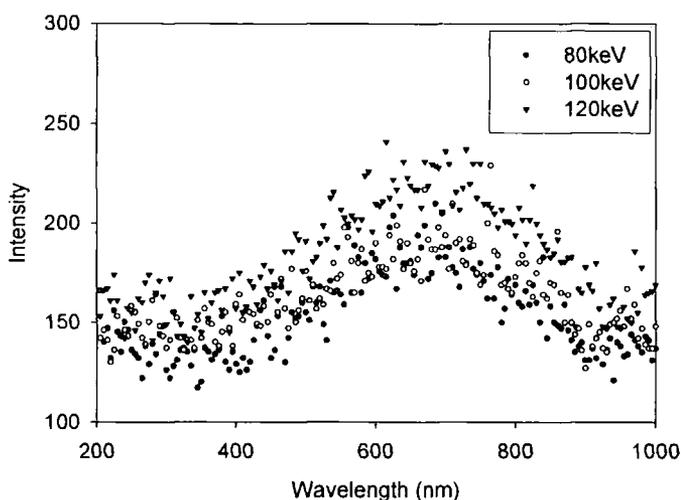
Figure 5.4: **Hole spectra taken with a CTEM beam and the maximum condenser aperture width.**

Recording hole spectra (as shown in Figures 5.3(a) and 5.4) is an established method of investigating background emission in detector systems. It is conceivable, however, that hole spectra underestimate the amount of gun glow picked up by the system. As can be seen in Figure 5.5(b) the mirror is facing away from the gun so it can only collect reflected gun glow. Therefore it would be better to illuminate a reflective TEM foil which has no intrinsic CL emission. Such a test specimen was made by gold coating a perforated carbon film. The holes in the film are much smaller than the large hole in a standard specimen (Figure 5.3(b)) and allow the beam to pass whilst leaving plenty of reflective surface area directly below the hole in the CL collection mirror. A series of spectra collected with this specimen is shown in Figure 5.5(a).

(a)

(b)

(c)

(d)
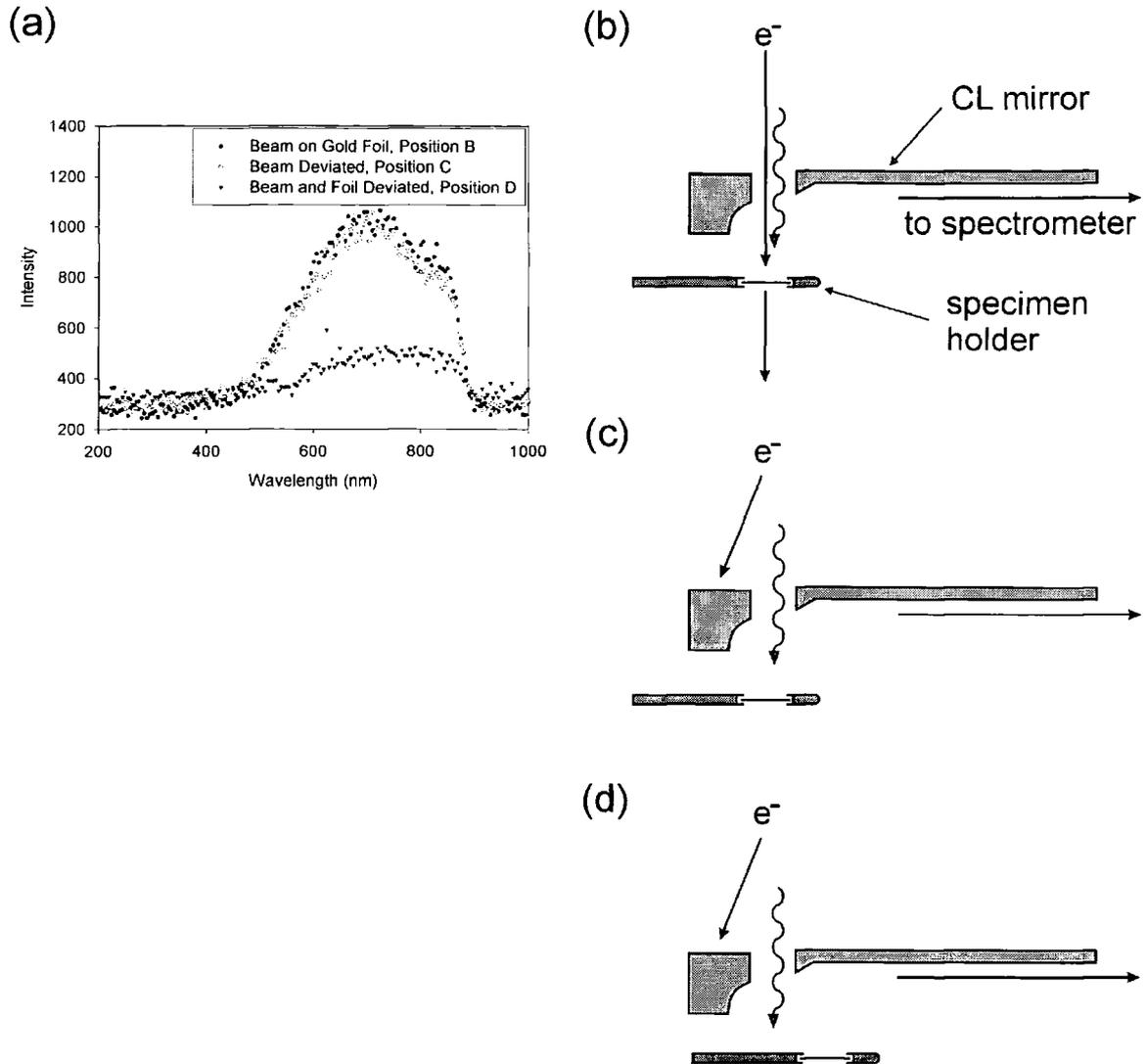
Figure 5.5:(a) Spectra taken with a 100kV beam and 400μm diameter condenser aperture with a gold coated holey carbon film in the specimen holder, spectra were taken for arrangements B,C and D; (b) beam passes through small hole in specimen; (c) specimen directly below hole in CL mirror, electron beam deviated above the mirror; (d) specimen holder directly below hole in CL mirror, electron beam deviated above the mirror.

Spectrum 'B' in Figure 5.5(a) shows the the spectrum with the beam passing through a hole in the gold coated carbon film. The spectrum has a peak around 650nm, similar to Figure 5.3(a). The intensity, however, is around five times greater. Spectrum 'C' is taken with the geometrical arrangement shown in Figure 5.5(c) - with the beam diverted off-axis so that it hits the top surface of the CL collection mirror. Spectrum 'C' is identical to spectrum 'B' demonstrating that the feature seen is indeed due to gun glow, not emission from the foil. Figure

5.5(d) shows the geometrical arrangement for spectrum 'D'. For this spectrum the specimen holder was inserted into the microscope column as far as possible so that the dull stainless steel of the holder was below the hole in the mirror. The beam was left off-axis. Spectrum 'D' consists of a broad band in the 600nm to 900nm range. This is similar to the hole spectra recorded in Figure 5.3(a) and is attributed to the lower reflectivity of the steel surface compared to the gold coated carbon film.

These experiments have identified a broad peak in the range 600-900nm as attributable to gun glow effects. The intensity of gun glow increases with the size of the condenser aperture. Operationally it is therefore advisable to work with the smallest possible condenser aperture setting in order to reduce the effects of gun glow.

5.2.5 Effect of Cooling

Luminescence studies are generally performed at the lowest temperatures possible to achieve sharply defined spectral lines and an increased probability of radiative recombination due to a lessening of phonon interactions [2-4]. The actual specimen temperature achieved using a liquid nitrogen cooled specimen holder is a function of the beam current, illumination area, sample geometry and thermal coefficients. The absolute sample temperature typically achieved has not been calculated; however a nominal temperature of 90K is routinely achieved if the specimen holder vacuum is regularly pumped out. Figure 5.6 shows the panchromatic CL emission from a GaN epilayer as it is cooled from room temperature to 90K. A STEM area raster was used to minimise specimen damage (see Chapter 6 for further discussion) and the area under the beam was monitored during cooling to counter sample drift during cooling. Cooling to 10-20K is reported to increase CL intensities by an order of magnitude or more [5], and work at this temperature is suggested as an area for future investigation.
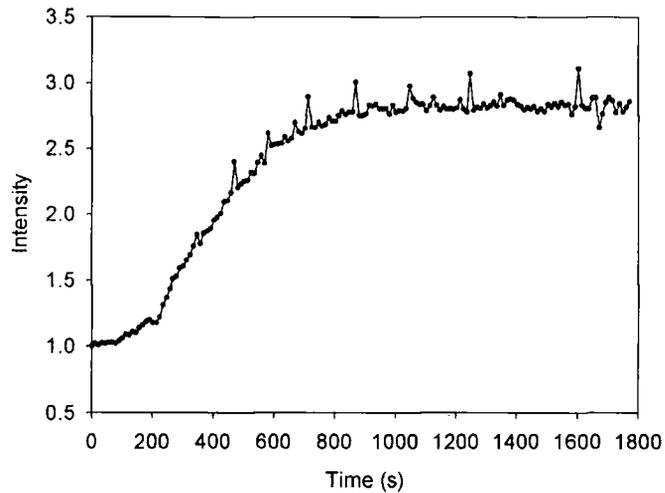
Figure 5.6: **Effect of cooling from room temperature to 90K on the panchromatic CL emission from GaN (120kV beam, STEM area scan).**

5.2.6 The Objective Aperture

When in place the objective aperture was discovered to have the effect of introducing a strong CL signal characteristic of the bulk material in a TEM foil. The CL emission was several orders of magnitude greater than the signal from the material under direct illumination. This effect has been observed in X-Ray microanalysis [6] and is thought to be due to electrons scattering off the upper surface of the objective aperture and exciting the TEM foil. This effect is not a major limitation as the inability to tilt the specimen with the CL collection mirror in place limits simultaneous diffraction contrast and CL imaging. Care was taken to ensure the objective aperture was removed prior to CL work.

5.4 CL Emission from a Thin Crystal

5.4.1 Resolution, Beam Broadening and Generation Volume

The spatial resolution of CL, d, is related to the electron probe diameter, d_p; the diameter of the generation volume, d_g; and the carrier diffusion length, L_d. The relationship between these parameters is given by Pennycook to be [7, 8]:

$$d = \sqrt{(d_p^2 + d_g^2 + L_d^2)} \qquad (5.1)$$

Whilst the probe diameter, d_p, will be constant the value of the parameters d_g and L_d in Equation 5.1 will vary depending on whether a bulk specimen or thin foil is being investigated. Both the bulk and thin foil regimes are briefly discussed below.

Bulk. There are a number of empirical expressions [2, 9-11] for the range of electron penetration in a material as a function of the incident beam energy. The range according to Kanaya and Okayama [11] is given as:

$$R_e = \left(\frac{0.0276A}{\rho Z^{0.889}}\right) E_b^{1.67} \qquad (\mu m) \qquad (5.2)$$

where A is the atomic weight in g/mol, the beam energy, E_b, is in keV, ρ is in g/cm³ and Z is the atomic number. This expression yields a value of $R_e \approx 40\mu m$ for a 120kV electron beam incident on GaN. Therefore at TEM operating voltages, considering only resolution, it is necessary to use a thin foil to limit the formation of a generation volume as shown in Figure 5.7.
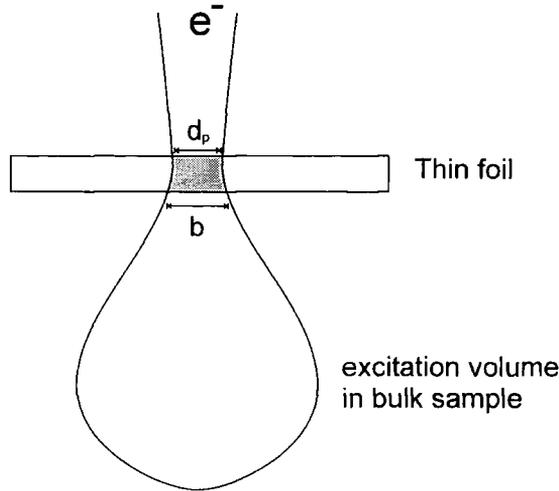
Figure 5.7:   Excitation volumes in a thin foil and a bulk specimen.

Thin foil. Passing through a thin foil the primary beam will undergo scattering events which will broaden the beam. Brown [12] gives the beam size, *b*, on exciting a thin foil of thickness *t* to be:

$$b = 6 \times 10^{-6} \frac{ZN^{1/2} \left(\frac{t}{a}\right)^{3/2}}{E_b} \quad (\mu m) \tag{5.3}$$

where *a* is the lattice parameter of the unit cell and *N* is the number of atoms in the cell. For a 250nm thick foil, *b*=80nm. Equation 5.3 assumes the incident electron beam to have a negligible width. A probe diameter of 10nm would therefore yield an exit beam size, *b*, of 90nm.

Monte Carlo simulations are another method of investigating electron scattering [2, 13]. In a simulation a trajectory is calculated for each electron as it undergoes elastic and inelastic scattering. Monte Carlo simulations for 100kV electrons have been performed using the commercially available *MC-SET* software [14] and are shown in Figure 5.8. The simulations shown in Figure 5.8(a-e) are for 100keV electrons incident on GaN layers of thickness 100nm to 10μm. The beam broadening seen in these simulations is in line with that given by Equation 5.3.

(a)

100.00 kV (scale = 0.10 um)
GaN Layer
GaN Gallium Nitride dx= 4.00 dy= 4.00 dz= 0.10

(b)

100.00 kV (scale = 0.25 um)
GaN Layer
GaN Gallium Nitride dx= 4.00 dy= 4.00 dz= 0.25

(c)

100.00 kV (scale = 0.50 um)
GaN Layer
GaN Gallium Nitride dx= 4.00 dy= 4.00 dz= 0.50

(d)

100.00 kV (scale = 1.00 um)
GaN thin section
GaN Gallium Nitride dx= 4.00 dy= 4.00 dz= 1.00

(e)

100.00 kV (scale = 10.00 um)
GaN Layer
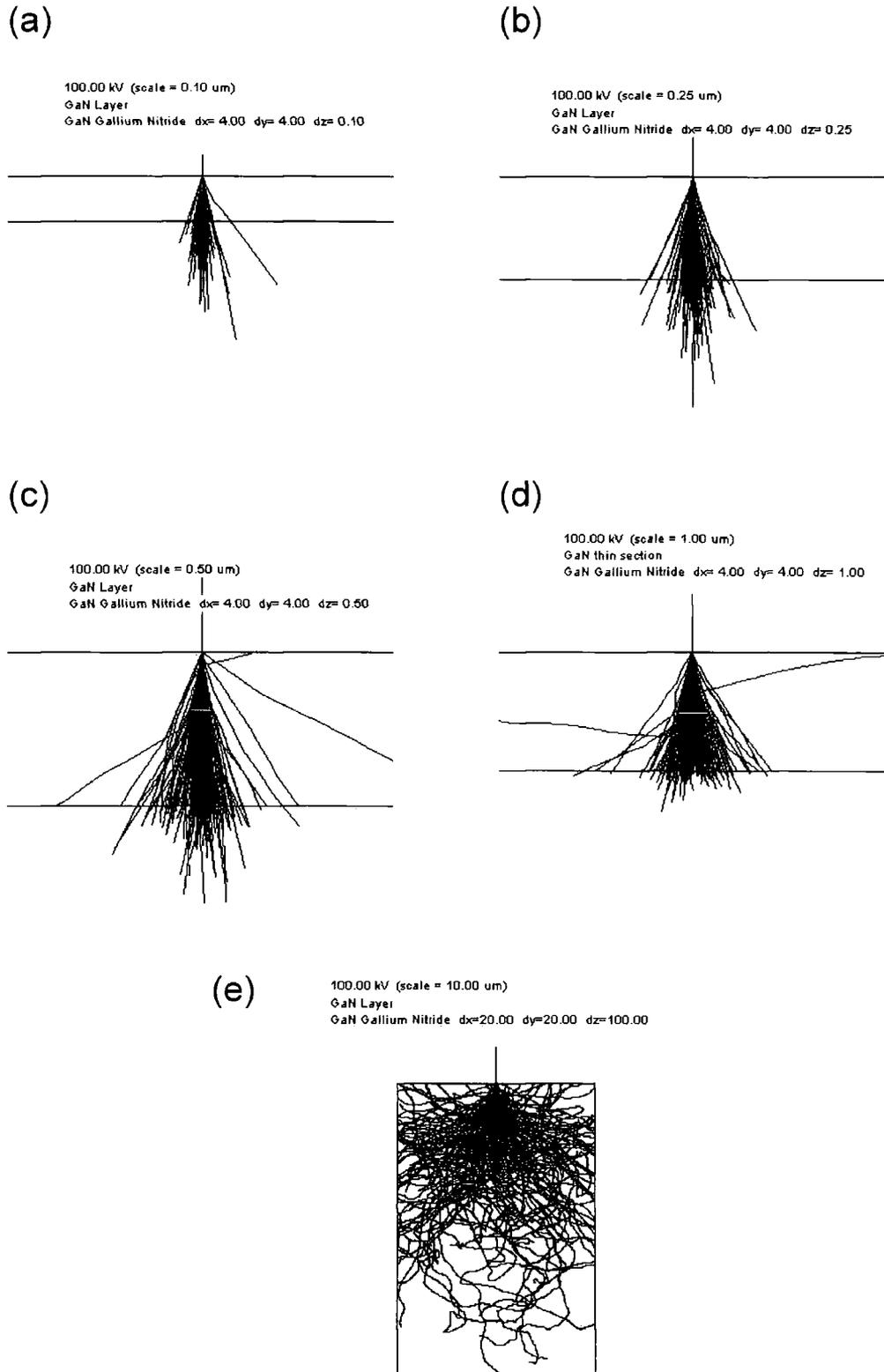GaN Gallium Nitride dx=20.00 dy=20.00 dz=100.00

Figure 5.8: Monte Carlo simulations for 100kV electron incident on GaN thin foils of thickness; (a) 100nm, (b) 250nm, (c) 500nm, (d) 1μm, and (e) 10μm. Simulations are performed using *MC-SET* [14].

The final parameter to consider in Equation 5.1 is carrier diffusion. In a bulk semiconductor the carrier diffusion length, L_d, is a function of impurity scattering and recombination processes. It is commonly defined as:

$$L_d = \sqrt{D\tau} \qquad (5.4)$$

where, D is a diffusion coefficient, and τ is the carrier lifetime. In a thin foil, however, the proximity of the crystal surfaces to the generated carriers will have a dominant effect. The rate of surface recombination is a function of the surface recombination velocity, s, expressed in cm/s. In a thin foil, making the assumption that $s=\infty$, Shockley [15] showed that:

$$L_d = \frac{t}{\pi} \qquad (5.5)$$

This can be thought of intuitively as effective 'pinning' of generated carriers by surface states, with carriers generated in the centre of the thin foil having the greatest diffusion length. However, Equation 5.5 was shown slightly to underestimate diffusion lengths as Pennycook [7] determined the diffusion length to be $t/2.2$.

With calculated values for the size of the generation volume and diffusion length it is now possible to calculate an estimated spatial resolution using Equation 5.1. For a 250nm thick foil with d_p=10nm, d_g=80nm and L_d=80nm, the spatial resolution, d=110nm. This value compares well to typical spatial resolutions of ~1μm in SEM-CL [16].

5.4.2 Thin Film Interference Effects

Thin film interference effects have been previously observed in TEM-CL spectroscopy experiments [17-19]. Yuan et al [18] modelled this effect by considering the interference from light generated in a thin pencil and emitted normal to the film. In the following section this concept is extended so that CL emission across all collection angles is included in the interference term.

5.4.3 Visual Basic Model

The incident electron beam is considered to generate electron-hole pairs in a thin cylinder through the specimen. It is assumed that the recombination of these electron-hole pairs results in the generation of cathodoluminescence (CL) uniformly through the specimen. Figure 5.9 represents the emission of CL from a point S at a depth x in a specimen of thickness t.
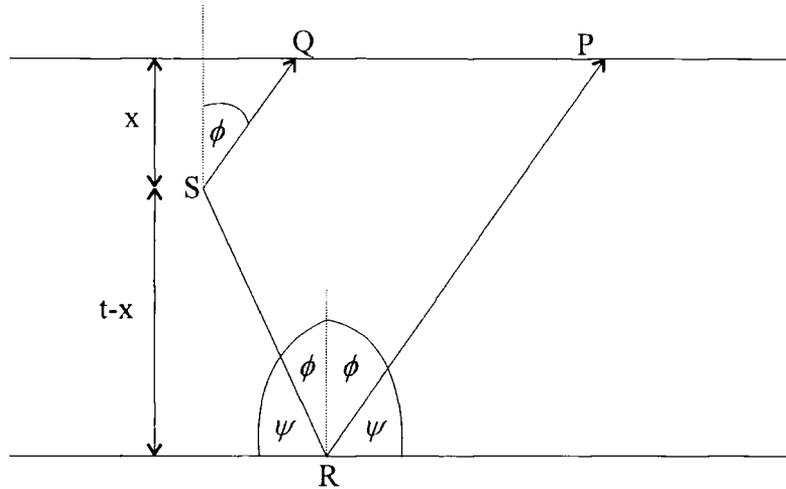
Figure 5.9: **Geometrical arrangement of CL emission from a point S at a depth x in a specimen of thickness t.**

To calculate the total interference term at the CL collection mirror it is necessary to calculate the interference term across the range of angles between the critical angle for escape from the specimen $(sin^{-1}(1/n))$ and the normal to the surface. Since the distance from the surface of the specimen to the CL collection mirror is much greater than the specimen thickness, d, we make the assumption that ϕ is fixed for a pair of rays SQ and RP and $\psi = 90 - \phi$.

Equation 5.6 describes, to a first approximation, the electric field $E(z)$ resulting from light emission from a point source a distance x below the top surface of the foil:

$$E(z) \cong E_0(z)\left[(1-r)e^{\frac{iknx}{\cos\phi}} + re^{\frac{ikn(2t-x)}{\cos\phi}}\right]$$

(5.6)

where r is the reflection coefficient of the light at the film's interface[1] and E_0 is the electric field from a single point source. The first term describes the interference contribution from the light travelling directly to the detector, whilst the second term describes the interference contribution of the light reflecting off the back surface of the film. All higher terms in r representing multiple internal reflections have been neglected since they have a significance of less than three percent. The total measured intensity, $I_{T\phi}$, at the detector resulting from interference from this cylinder of point sources is calculated by integrating the product of Equation 5.6 and its complex conjugate over the thickness of the foil:

$$I_{T\phi} \cong I_0\left[d - 2rd + \frac{r\cos\phi}{kn}\sin\left(\frac{2knt}{\cos\phi}\right) \right] \tag{5.7}$$

where I_0 is the intensity generated from a point source. To calculate the total observed interference, I_T, it is necessary to integrate Equation 5.7 at all angles between the critical angle for light escape from the foil and the normal to its surface. This was calculated numerically by considering the intensity across an annulus of thickness $d\phi$ at a position ϕ. It was found that 100 incremental angular steps were sufficient to evaluate the integral. The effect of foil thickness variation on emission at constant wavelength is now discussed.

Constant Wavelength. Figure 5.10 has been calculated using only the periodic part of Equation 5.7 to highlight features which are masked when all three terms in Equation 5.7 are included as in Figure 5.11. There are three features in Figure 5.10. The first is the rapidly oscillating line which is a function of the thickness of the foil and the wavelength of emission. The second feature is the overall envelope function which is a result of the numerical integration over a range of angles between the normal to the surface and the critical angle. The third is the increase in magnitude of the oscillation as the thickness of the foil increases. However this will only be true for completely coherent point sources. In reality the interference from rays with large path lengths will not be so marked

---

[1] The value of r for GaN is calculated to be 0.17. This value diverges as we approach the critical angle. A derivation of r using the Fresnel equations is given in Appendix B and the effect of using a variable value for r is shown in Figure 5.14.

since partial temporal coherence will suppress the interference from these rays [18, 20, 21].
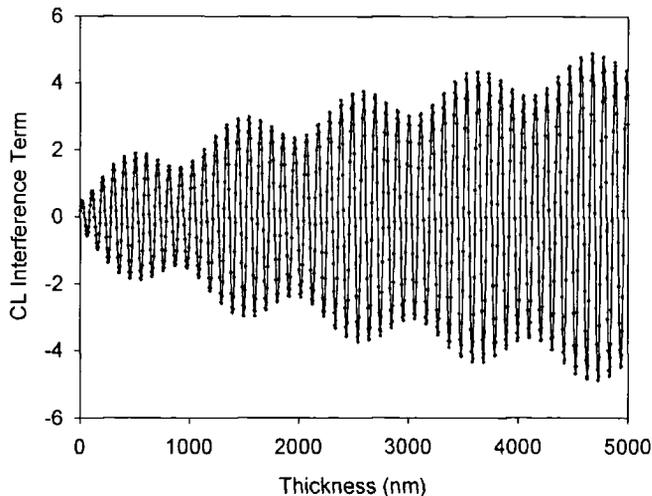

Figure 5.10: Numerical evaluation of Equation 5.7 calculated with an emission wavelength of 500nm.

Whilst Figure 5.10 highlights the interference effects the total observed light output is shown in Figure 5.11.
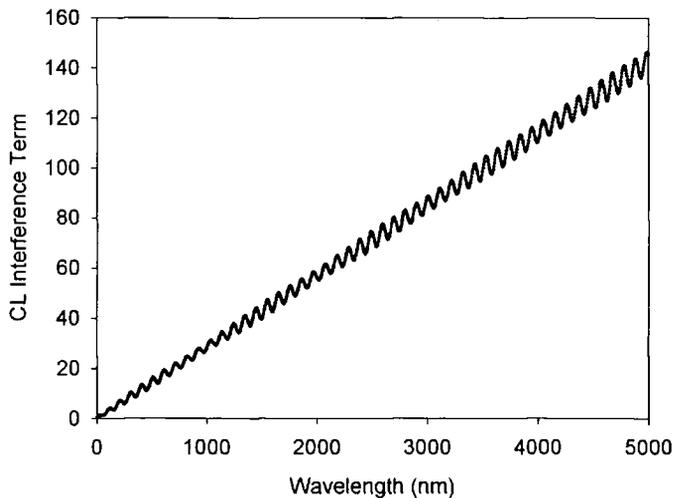

Figure 5.11: Evaluation of the total observed light output calculated with an emission wavelength of 500nm.

Figure 5.12 compares the effect of only considering light that is emitted normal to the foil's surface with the full calculation across all angles between the critical angle and the normal. Considering only the normal rays yields oscillations of the same periodicity as the full angular range, but of increased amplitude. This is in agreement with the analysis performed by Yuan et al [18] where only light in the limiting case of emission normal to the surface was considered. This difference can be attributed to the smoothing effect of the range of phase differences generated by the integration over the angular range performed in this analysis. This is a more accurate representation of the physical system encountered in TEM-CL, where all emission close to the normal would travel through the hole in the CL mirror without being recorded. This has been allowed for in the calculations. It was shown that when the mirror is in its optimum collection position 1mm above the sample it is wide enough to collect all light emission up to the critical angle of gallium nitride.
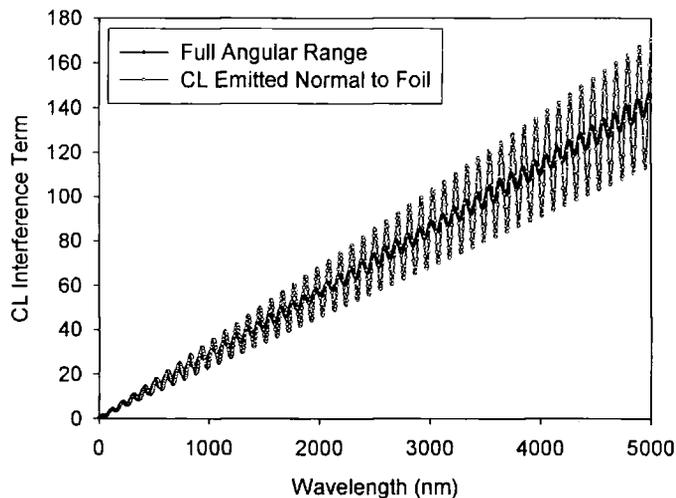

Figure 12: **Numerical evaluation of the total observed light output calculated with an emission wavelength of 500nm using the full angular range method and only considering the light emitted normal to the foil's surface.**

In the next section the variation of CL intensity with wavelength for foils of constant thickness is considered.

Spectra From Foils of Constant Thickness. Figure 5.13 has been generated using Equation 5.7 with the thickness held constant while the wavelength is changed, again using 100 angular steps to calculate each data point.
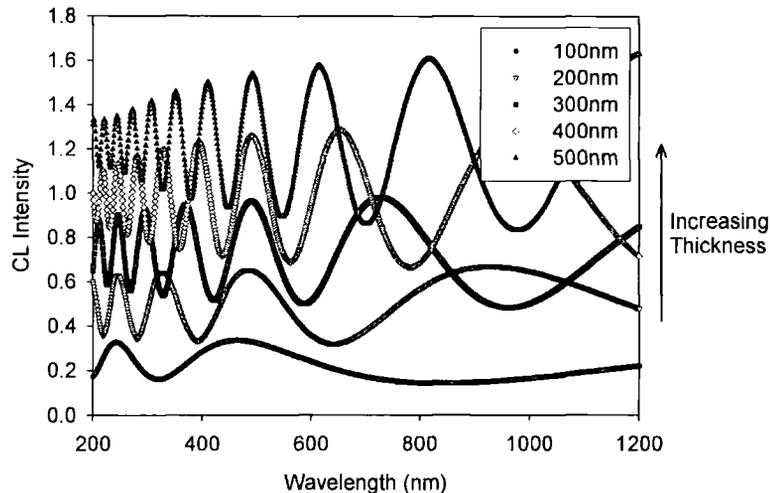
Figure 5.13: CL emission vs wavelength for foils of thickness varying between 100nm and 500nm.

It is seen that the CL emission from the thicker foils is greater, as would be expected, and that the intensity modulation of the CL intensity from interference is less for thinner foils. At shorter wavelengths the oscillations of the CL intensity are more frequent as the wave fronts are closer together at the high frequency end of the spectrum. The amplitude of the interference oscillations increases with wavelength. This is because at longer wavelengths it becomes less likely that there will be both constructive and destructive interference at the same wavelength thereby increasing the magnitude of the oscillations. Once the wavelength becomes an order of magnitude greater or more than the thickness of the foil, the CL intensity increases to a steady state as the phase difference between the direct and reflected rays tends to zero.

Reflectivity considerations. In this subsection the effect of the variation in reflectance, *r*, calculated in Appendix B, is considered. The simulation has been performed for a range of foil thicknesses and is shown in Figure 5.14 for a 500nm thick foil.
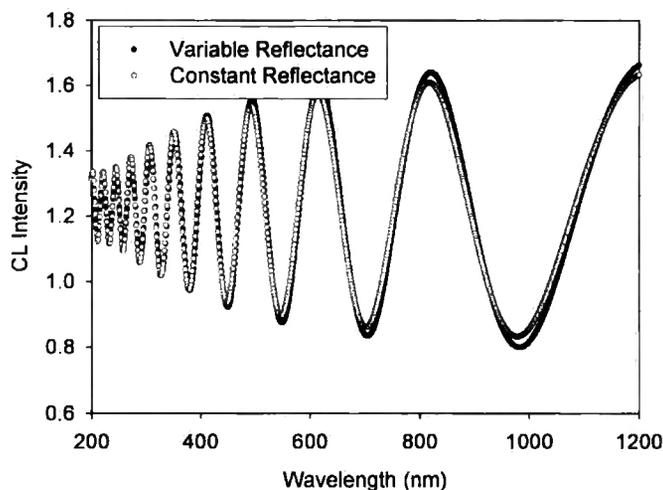
Figure 5.14: **CL emission versus wavelength for a 500nm thick foil with reflectance set to a fixed value of 0.17 and varying as defined by Equation B3.**

There is little change to the CL emission from thinner foils when a variable value for the reflectivity is used. However for foils thicker than 300nm there is a noticeable effect with the amplitude of oscillation of CL emission increasing and an increase in period of the oscillations. These differences are more marked at longer wavelengths.

Effect of surface recombination and generation function. The analyses in the previous subsections all have the implicit assumption that the CL is generated uniformly throughout the foil. The aim of this section is to model how non-radiative surface recombination and inhomogeneous electron-hole pair generation by the electron beam will affect the total emitted CL. To do this it is necessary to evaluate $I_{T\phi}$ numerically rather than using the algebraic solution given in Equation 5.7. Simulations show that an adequate numerical integration is achieved by using an incremental thickness step of one angstrom. The calculated intensity for each incremental thickness is multiplied by a factor to allow for the effects of non-radiative surface recombination and non-homogenous energy deposition by the electron beam with foil thickness. The model used to allow for these effects is described in detail in Section 7.4. The simulated CL emission for a 500nm thick foil using this modified model is compared to a simulation performed on a uniform generation assumption in Figure 5.15.
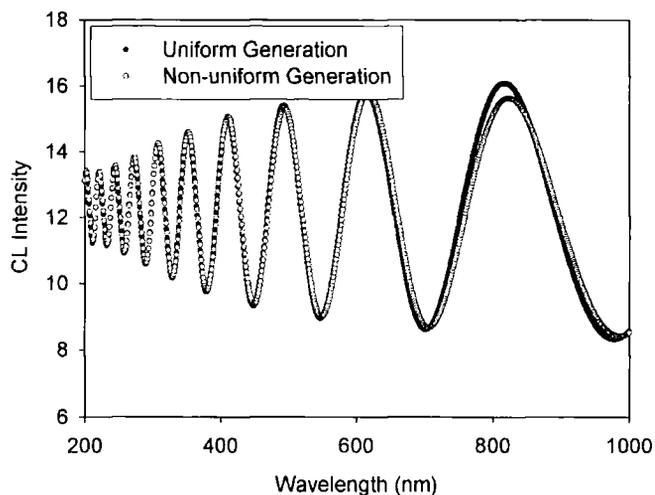
Figure 5.15: Comparison of CL emission versus wavelength for a 500nm thick foil using a uniform factor for the generation of CL and a non-uniform factor with depth dependent values. The CL emission calculated using the depth dependent generation model has been scaled up for comparison purposes. In reality the use of this model will result in reduced CL emission due to losses from non-radiative surface recombination.

Figure 5.15 shows there is little difference in the two simulations for a 500nm thick foil. Other simulations have shown the greatest difference to occur for thinner foils. This is a logical finding as it would be expected that the relative effects of surface recombination would be greater for a thin foil.

5.4.4 Comparison with Experimental Data (and limitations of the model)

Thin film interference effects were not observed in TEM-CL spectra acquired using a CTEM beam as a source of excitation. This may be accounted for by the larger area illuminated by the CTEM beam resulting in CL emission from parts of the foil with different thicknesses. Interference effects were also not observed in STEM-CL monochromatic images. This is thought to be due to the relatively large spectral dispersion typically needed (~20nm) to achieve a measurable signal from a thin foil. Over the spectral range measured constructive and destructive interference may be self compensating. Interference effects were, however, observed in spectra acquired using a stationary STEM probe as a source of excitation. Such a spectrum is shown in Figure 5.16 in which the underlying curve can be seen to be overlaid with a rapidly oscillating function. Fitting this function to the simulations performed indicated that the

61

section of foil was approximately 500nm thick. (Spectra were rarely collected using a stationary STEM probe to avoid damage to the specimen. A small area STEM scan was found to be a more satisfactory method for spectral acquisition.)
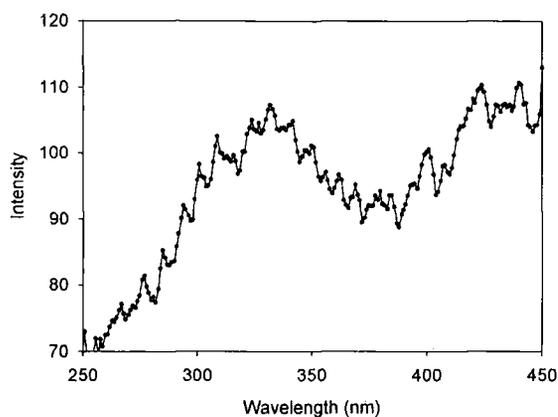
Figure 5.16: TEM-CL spectra acquired with a stationary STEM probe on a thin GaN epilayer (100kV beam, 100K nominal temperature).

This fitting process clearly has the potential to be used to strip the interference fringes from a peak so the underlying peaks can be investigated. It can also be used as a thickness estimator for STEM work in which extinction fringes are not as clear as in diffraction contrast TEM.

5.5 Conclusions

The performance of a CL collection system fitted to a *JEOL 200CX* TEM with STEM scanning attachment was investigated. The spectrometer was calibrated using standard sources to an error of 0.243nm for a grating blazed for maximum reflectance at 300nm and 0.707nm for a grating blazed at 500nm. The maximum spectral resolution was determined to be 1nm. A broad peak centred at 650nm observed with the largest condenser aperture in place was attributed to glow from the tungsten filament and CL from stray electron collisions. If the objective aperture was inserted electrons scattered from the aperture were shown to excite the substrate and give spurious CL emission.

Thin film interference in a parallel sided specimen excited by a cylindrical electron probe was modelled using a *Visual Basic* routine. Emission over an

angular range between the critical angle for emission and the hole in the collecting mirror were considered for the first time. The model was used to investigate the variation in CL intensity with foil thickness for a particular wavelength or the variation in CL intensity with wavelength for a particular thickness. Thickness fringes in images were predicted, as were thickness oscillations in spectra. Refinement of the model to account for the wavelength dependence of reflectance and surface recombination had only a minor influence on the form of the modelling results. Interference effects on spectra were observed experimentally, but only for the case of a stationary STEM beam. Irradiation of a distribution of thicknesses in an area using either a CTEM or moving STEM beam caused the fringes to be lost: this suggests the conditions to be used for the most reliable spectral acquisition.

5.6 References

1.	Curie, D., *Luminescence in Crystals*, (Methuen & Co., London, 1963).

2.	Yacobi, B.G. and D.B. Holt, *Cathodoluminescence Microscopy of Inorganic Solids*, (Plenum Press, New York, 1990).

3.	Garlick, G.F.J., *Luminescent Materials*, (Oxford University Press, London, 1949).

4.	Dekker, A.J., *Solid State Physics*, (Macmillan & Co Ltd., London, 1964).

5.	Ohno, Y., *Private communication*, (2003).

6.	Williams, D.B. and C.B. Carter, *Transmission Electron Microscopy - Spectrometry*, (Plenum Press, New York, 1996).

7.	Pennycook, S.J., *Investigation of the Electronic Effects of Dislocations by STEM*, Ultramicroscopy **7** (1981) 99-104.

8.	Pennycook, S.J., *Studies of Cathodoluminescence on a Scanning Transmission Electron Microscope*, PhD Thesis (1978), University of Cambridge, Cambridge.

9.	Goldstein, J.I., D.E. Newbury, P. Echlin, D.C. Joy, C. Fiori, and E. Lifshin, *Scanning Electron Microscopy and X-Ray Microanalysis*, (Plenum Press, New York, 1981).

10.	Everhart, T.E. and P.H. Hoff, *Determination of Kilovolt Electron Energy Dissipation vs Penetration Distance in Solid Materials*, Journal of Applied Physics **42** (1971) 5837-5846.

11.	Kanaya, K. and S. Okayama, *Penetration and Energy-Loss Theory of Electrons in Solid Targets*, Journal of Physics D: Applied Physics **5** (1972) 43-58.

12.	Brown, L.M., *Scanning Transmission Electron Microscopy: Microanalysis for the Microelectronic Age*, Journal of Physics F: Metal Physics **11** (1981) 1-26.

13.	Joy, D.C., *Monte Carlo Modeling for Electron Microscopy and Microanalysis*, (Oxford Univeristy Press, Inc., New York, 1995).

14.	Napchan, E., *MC-SET*, (2003), DLM Enterprises.

15.	Shockley, W., *Electrons and Holes in Semiconductors*, (D. Van Nostrand Company, Inc., New York, 1950).

16. Yamamoto, N., *Development of Cathodoluminescence for Semiconductor Research*, in *Nanoscale Spectroscopy and Its Applications to Semiconductor Research*, Y. Watanabe, S. Heun, G. Salviati, and N. Yamamoto, (Springer-Verlag, Heidelberg, 2002).

17. Steeds, J.W., *Performance and Applications of a STEM-Cathodoluminescence System*, Revue de Physique Appliquee **24** (1989) C6-65 - C6-72.

18. Yuan, J., S.D. Berger, and L.M. Brown, *Thickness Dependence of Cathodoluminescence in Thin Films*, Journal of Physics: Condensed Matter **1** (1989) 3253-3265.

19. Albrecht, M., H.P. Strunk, J.L. Weyher, I. Grzegory, S. Porowski, and T. Wosinski, *Carrier Recombination at Single Dislocations in GaN Measured by Cathodoluminescence in a Transmission Electron Microscope*, Journal of Applied Physics **92** (2002) 2000-2005.

20. Hecht, E., *Optics*, (Addison-Wesley, Reading, Massachusetts, 1974).

21. Curry, C., *Geometrical Optics*, (Edward Arnold & Co., London, 1953).

TEM-CL Spectroscopy

6.1 Introduction

The aims of this chapter are: to identify features observed in TEM-CL spectra of GaN/In$_x$Ga$_{1-x}$N QW structures grown on sapphire and in GaN epilayers grown on LiAlO$_2$; to investigate how the excitation conditions in TEM-CL affect these spectra; and to investigate the effects of electron beam degradation on the CL emission from these materials.

This information is necessary to further the interpretation of STEM-CL images and spectral data presented in Chapters 7 and 8. The excitation conditions in TEM-CL are evaluated using beam current measurements and an empirical description of the energy deposited by a high energy electron beam in a TEM foil. In-situ measurements of the beam induced degradation of CL emission are presented and analysed using a recombination-centre model.

6.2 Samples used in this chapter

Sample	Epilayer structure	Substrate	Growth Method	Summary Growth Details
M-plane GaN epilayer	500nm epilayer	γ-LiAlO$_2$ (100)	PAMBE (Paul-Drude Institute, Berlin)	750°C substrate temperature, constant nitrogen flux [1, 2]
In$_{0.1}$Ga$_{0.9}$N SQW	1μm GaN buffer layer, 2.5nm In$_x$Ga$_{1-x}$N QW, 15nm GaN capping layer. (x=0.101±0.015)	c-plane sapphire	MOVPE (Institute of Photonics, University of Strathclyde)	20nm GaN nucleation layer at 540°C, GaN buffer layer at 1140°C, In$_x$Ga$_{1-x}$N QW grown at 832°C [3, 4]
In$_{0.1}$Ga$_{0.9}$N 2QW	1μm GaN buffer layer, 2.5nm In$_x$Ga$_{1-x}$N QW, 7.5nm GaN barrier layer, 2.5nm In$_x$Ga$_{1-x}$N QW, 15nm GaN capping layer. (x=0.101±0.015)	c-plane sapphire	MOVPE (Institute of Photonics, University of Strathclyde)	20nm GaN nucleation layer at 540°C, GaN buffer layer at 1140°C, In$_x$Ga$_{1-x}$N QWs grown at 832°C [3, 4]
In$_{0.2}$Ga$_{0.8}$N 8QW	1μm GaN buffer layer, 8-period In$_x$Ga$_{1-x}$N/GaN QW structure (7nm barrier thickness, 2.8nm QW thickness), 0.4nm GaN capping layer (growth interrupted). (x=0.196±0.025)	c-plane sapphire	MOVPE (Institute of Photonics, University of Strathclyde)	20nm GaN nucleation layer at 540°C, GaN buffer layer at 1140°C, In$_x$Ga$_{1-x}$N QW grown at 760°C. [3, 5]

Table 6.1:　**Specimen growth details.**

The samples investigated in this chapter are listed in Table 6.1 and the reader is referred to Section 3.4 for general descriptions of growth methods. Spectra from the samples investigated in this chapter are typical of spectra from other samples investigated in this work. Differences such as quantum well emission wavelengths are discussed when results from other samples are presented.

6.3 Excitation Conditions

A fraction of the electron beam energy deposited in a semiconductor will be converted into cathodoluminescence through the radiative recombination of electron-hole pairs. It has been shown that the injected density of electron-hole pairs in a semiconductor can influence luminescent properties [6, 7]. To

investigate the free carrier generation rate in TEM-CL experiments, beam current measurements (Section 6.3a) have been analysed using an analytical expression for the energy loss per unit path length for electrons described in Section 6.3b.

(a) Beam Current Measurements

Beam current measurements for the *JEOL 200CX* TEM taken with a Faraday cup in STEM and CTEM modes are shown in Table 6.2. In each instance the filament current was set to saturation before inserting the Faraday cup. Beam current values vary with the position of the tip of the tungsten filament in relation to the top of the Wehnelt cylinder so beam current measurements were repeated as needed.

Accelerating Voltage	Condenser Aperture	STEM Current (amps)	e⁻ per cm² per s	CTEM Current (amps)	e⁻ per cm² per s
40kV	1	2.1E-11	1.7E+20	2.1E-09	1.7E+18
	2	7.0E-12	5.6E+19	7.0E-10	5.6E+17
	3	2.0E-12	1.6E+19	1.8E-10	1.4E+17
	4	-	-	7.0E-12	5.6E+15
80kV	1	3.1E-11	2.5E+20	2.0E-09	1.6E+18
	2	1.1E-11	8.8E+19	6.8E-10	5.4E+17
	3	3.0E-12	2.4E+19	1.9E-10	1.5E+17
	4	-	-	7.0E-12	5.6E+15
100kV	1	1.0E-10	8.0E+20	9.3E-09	7.4E+18
	2	3.3E-11	2.6E+20	3.2E-09	2.5E+18
	3	9.0E-12	7.2E+19	8.6E-10	6.9E+17
	4	-	-	3.2E-11	2.5E+16
120kV	1	1.3E-10	9.9E+20	1.1E-08	8.6E+18
	2	3.7E-11	2.9E+20	3.3E-09	2.6E+18
	3	1.1E-11	8.8E+19	9.7E-10	7.7E+17
	4	-	-	3.5E-11	2.8E+16

Table 6.2: **STEM and CTEM beam currents for different beam accelerating voltages and condenser apertures in the *JEOL 200CX*. The electron flux density is calculated based upon a CTEM beam diameter of 1μm and STEM beam diameter of 10nm.**

(b) Energy Deposition – Bethe Model

The average rate of energy loss by an electron travelling through a material was originally derived by Bethe. [8] This is expressed in Equation 6.1 with relativistic corrections [9]:

$$\left(\frac{dE}{dz}\right)=\left(\frac{e^2}{4\pi\varepsilon_0}\right)^2\frac{2\pi N_0 Z\rho}{mc^2\beta^2 A}\left[\begin{array}{c}\ln\dfrac{T(T+mc^2)^2\beta^2}{2I^2mc^2}+(1-\beta^2)\\-\left(2\sqrt{1-\beta^2}-1+\beta^2\right)\ln 2+\dfrac{1}{8}\left(1-\sqrt{1-\beta^2}\right)^2\end{array}\right] \tag{6.1}$$

where $\beta=v/c$, v is the electron velocity, c the speed of light, Z the atomic number, A the atomic weight, ρ the density, N_0 is Avogadro's constant, T the kinetic energy of the electron, and I is the mean ionisation potential. The mean ionisation potential represents the average energy lost by an electron at an electron-solid interaction. This has been shown to be described empirically as [10]:

$$I=\left[9.76Z+\frac{58.5}{Z^{0.19}}\right] \quad \text{(eV)} \tag{6.2}$$

Values of the variation in dE/dz with accelerating voltage are shown in Table 6.3. These have been calculated using a mean value of 25 for the atomic number in Equations 6.1 and 6.2.

	80kV	**100kV**	**120kV**
$\dfrac{dE}{dz}$	1.54 eV/nm	1.33 eV/nm	1.19 eV/nm

Table 6.3: **Bethe energy loss per unit path length values.**

These values allow a calculation of the generation rate per unit volume of electron-hole pairs in a TEM foil. It may be assumed that dE/dz is constant and the average energy deposited by each electron passing through the foil is 130eV. The average energy lost by the incident electron beam in generating an electron-hole pair, ε, has been shown to be approximately three times the bandgap energy [11]. For the purposes of this investigation it is adequate to make the assumption

that ε=10eV. The average number of electron-hole pairs generated by a single electron of energy 100keV passing through 100nm of GaN is therefore approximately 13. A typical CTEM electron flux of 10^{18} e·s^{-1}cm^{-2} would therefore generate approximately 10^{19} e-h^{+} pairs s^{-1}cm^{-2} throughout a foil thickness of 100nm. This is equivalent 10^{24} e-h^{+} pairs s^{-1}cm^{-3}.

(c) Discussion of Excitation Conditions

The average energy deposited by a single electron of energy 80-120keV has been shown (Table 6.3) to be ~1.5eV/nm in GaN. This value reduces by 30% as the electron energy is increased from 80 to 120keV due to the decrease in electron-solid interaction cross-section as the electron energy is increased. Under typical TEM beam current conditions this rate of energy deposition would yield an electron-hole pair generation rate of approximately 10^{24} e-h^{+} pairs s^{-1}cm^{-3}. This is a high carrier density in comparison to typical PL and SEM-CL operating conditions which are typically <10^{18} cm^{-3}. Studies of GaN taken under high excitation conditions have shown the spectra to be influenced by the effects of inelastic exciton-exciton scattering and electron-hole plasma emission [7, 12-17]. The results of these calculations will be discussed further in the following sections.

6.4 Spectral Features of GaN and In$_x$Ga$_{1-x}$N

6.4.1 Spectral features of c-plane In$_x$Ga$_{1-x}$N /GaN on (0001) Sapphire

Figure 6.2 shows a STEM-CL spectrum from a cross-section TEM specimen made from the In$_{0.1}$Ga$_{0.9}$N single QW sample described in Table 6.1. The spectrum was acquired with the STEM probe scanning an area containing the GaN layer and the QW. The integration time at each monochromator position was two seconds, a time much greater than the STEM duty cycle.
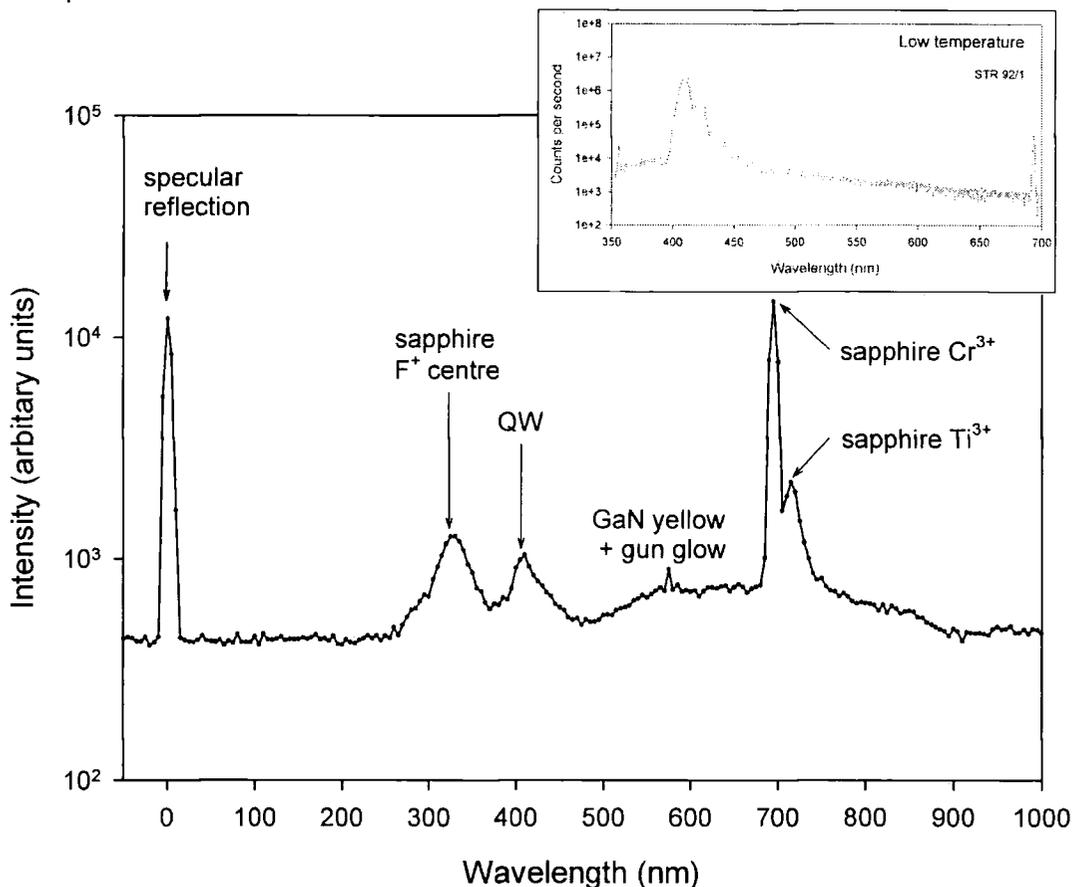
Figure 6.1: **STEM-CL spectrum of In$_{0.1}$Ga$_{0.9}$N single quantum well (100kV beam energy, cooled to 100K). Inset shows a PL spectrum of the sample[1].**

Figure 6.1 is typical of spectra collected in both STEM and CTEM modes. The spectrum is rich in features which have been attributed to the sapphire substrate. This is surprising as the spectrum was acquired from a GaN epitaxial layer containing an In$_{0.1}$Ga$_{0.9}$N QW. Spectral features attributed to the In$_{0.1}$Ga$_{0.9}$N

---

[1] PL measurements performed by P. Dawson, UMIST.

/GaN structure are less dominant in the spectrum. The peak at 410nm is attributed to the single $In_{0.1}Ga_{0.9}N$ QW and is in the same position as the QW peak seen in PL[2] spectra of the same sample (STEM-CL monochromatic images presented in Chapter 7 confirm the 410nm emission originates from the expected position of the QW in the foil). A broad peak can be seen in the range 480-660nm. This is attributed to GaN yellow emission [18] and 'gun glow' (see Section 5.2.4). There is evidence of a small shoulder at 360nm on the broad peak labelled sapphire F^+ (colour) centre. This is possibly attributable to a GaN near band edge feature such as emission due to the recombination of free excitons [7, 19]. The PL spectrum of this sample revealed the near band edge feature to be several orders of magnitude lower than the QW emission which is consistent with this observation. However, the near band edge is clearly defined in PL spectra with no sapphire luminescence peaks obscuring it. The origins of the sapphire luminescence seen in Figure 6.1 will now be discussed.

The sapphire luminescence will be discussed in four paragraphs. The first will address the physical origins of spectral features seen in sapphire, the second will discuss some of the differences between PL and (S)TEM-CL spectroscopy, and the third the effects of sample geometry. In the final paragraph mechanisms to account for the observation of spectral features characteristic of sapphire during illumination of only the GaN layer are considered.

Sapphire emission at 694nm is routinely observed in SEM-CL and PL studies and is due to the Cr^{3+} doublet [20] (692.0nm and 693.4nm). It could not be resolved with the gratings used in this work. On the low energy side of this doublet, the peak at 715nm has been attributed to Ti^{3+} [21]. A broad peak at 330nm and a less intense peak at 415nm have been previously observed in neutron and electron bombarded sapphire [22-25] and are attributed to an F^+ centre (an oxygen vacancy which has trapped a single electron) and an F centre (an oxygen vacancy containing two trapped electrons), respectively. Under electron irradiation the peak at 415nm is reported to be much weaker than the 330nm F^+ centre peak [24, 26]. This suggests that the peak seen in Figure 6.2 at 330nm is due to an electron irradiation induced F^+ centre. Whilst this peak has been previously observed in TEM-CL spectra [27] it is not usually observed in PL and SEM-CL studies of epitaxial layers grown on sapphire. Possible explanations for this are now described.

---

[2] PL measurements performed by P. Dawson, UMIST.

Lee and Crawford [22] discovered that light of wavelength 258nm was needed to produce emission in the band centred at 330nm. As PL studies of GaN are often performed using the 334nm line of an Ar^+ laser or the 325nm line of a HeCd laser the exciting photons would be insufficiently energetic to yield F^+ centre emission at 330nm. However, in SEM-CL, electron energies are enough to excite sapphire F^+ centre luminescence. It is possible that its absence is due to the threshold energy for the introduction of the F^+ centre being between 30keV and 80keV (the minimum operating voltage for TEM-CL). Geometrical reasons for the absence of the F^+ centre peak in SEM-CL are now discussed.

Most of the samples investigated in this study were prepared as cross-sectional TEM foils. The geometry of such a foil is a wedge with the epitaxial layer at the thinnest end and substrate making up the thick end of the wedge (as described in Section 4.3). In comparison to experiments on plan view samples (which are usually used in PL and SEM-CL) two major differences are; a) the volume ratio of epitaxial layer to substrate is lower in cross-section, and b) luminescence from the substrate can escape directly to the surface from a cross-sectional foil rather than having to travel through the epitaxial layer to escape. In the case of the sapphire/GaN system, F^+ centre luminescence emitted from a sapphire substrate would be absorbed rapidly by a GaN epitaxial layer due to the high absorption coefficient of semiconductors at above band gap energies.

The final aspect to consider is why spectral features specific to sapphire are observed when only the GaN layer is illuminated. A number of different mechanisms for the excitation of the sapphire substrate have been considered:

a)   Electrons in the tails of the Gaussian electron beam shape; the energy loss of a 100keV electron passing through a 100nm thick foil is on average ~100eV. However, if an electron in the Gaussian tail of the primary beam was to be completely stopped in a thicker (substrate) section of the wedge the whole 100keV would be available for e-h+ pair generation,

b)   Deflected primary electrons and fast secondary electrons; fast secondary electrons and primary electrons deflected such that they entered the substrate laterally would lose all their energy inside the specimen (assuming no further large angle scattering). As described in (a) it would only take approximately one in a thousand such scattering events to deposit the same energy in

the substrate as was deposited in the area under direct electron beam illumination,

c)   <u>X-rays</u>; bremsstrahlung and characteristic X-rays generated in the specimen and inside the microscope pole piece will excite luminescence away from the region excited by the primary beam [28],

d)   <u>Surface recombination</u>; whilst not an excitation issue, this will suppress luminescence from the epitaxial layer under investigation as a greater proportion of available free carriers will recombine at the surface of a thin specimen as opposed to a thicker section (this is discussed in greater detail in Chapter 7). This may account for strong substrate luminescence with only weak excitation of the substrate.

The effect of these four factors has not been evaluated quantitatively in this study.   However, greater understanding of the relative contribution of these factors would be valuable and might perhaps be the subject of further study.

To investigate the hypothesis that the sapphire F^+ centre peak would be absorbed by a GaN layer, a plan view specimen was prepared and spectra were obtained with the substrate facing away from the CL collection mirror (spectrum A) and the substrate facing the mirror (spectrum B). The two spectra are plotted together in Figure 6.2.
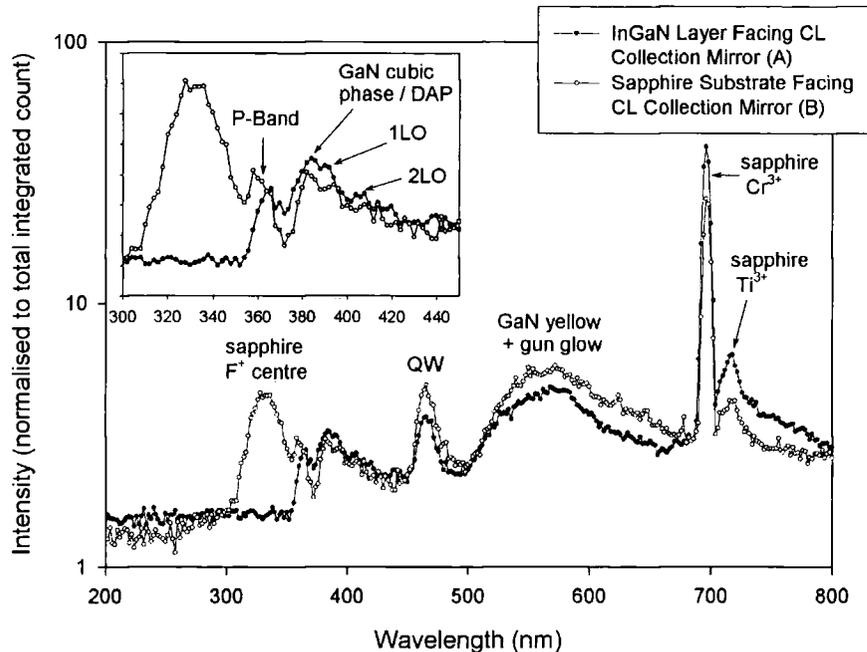
Figure 6.2: **TEM-CL spectra of In$_{0.2}$Ga$_{0.8}$N 8QW plan view foil (100kV electron beam, cooled to 100K, CTEM acquisition)**

Figure 6.2 does indeed confirm that the sapphire F$^+$ centre peak is absorbed by ~1µm of GaN. The inset to Figure 6.2 shows there are also slight differences to the near band edge luminescence for the two spectra with the peak centred at 360-365nm appearing to be at a higher energy in spectrum B. This may be attributed to the influence of the F$^+$ centre peak creating an apparent blue shift due to peak overlap. Comparison of Figure 6.2 to 6.1 shows near band edge features in the spectra from the plan view foil which are not seen in the cross-sectional foil and a different QW position. The QW position (465nm) in figure 6.2 is as expected from PL performed on the same specimen[3]. However, the near band edge features seen deserve further discussion.

It is suggested that the stronger near band edge features seen are due to the larger volume of GaN being excited in the plan view foil. From the literature it is known that the dominant spectral feature in epitaxial GaN layers at a temperature of 100K and low excitation density would be due to free exciton recombination at 355-356nm [7, 19]. Spectrum A, however, exhibits a peak starting at 355nm and rising to a peak at 365nm. In studies using high PL

---

[3] PL performed by R. Pecharroman-Gallego, Department of Physics, University of Strathclyde.

excitation densities[4] this feature has been observed and is sometimes referred to as the 'P' line. Hvam and Ejder [13] identified this emission band at 359.1 and 359.6nm in highly excited GaN (excitation intensity of 2.5MW cm^{-2}) at a temperature of 2K, attributing it to inelastic exciton-exciton scattering. As the temperature was increased to 77K and the free exciton luminescence increased (due to the thermal dissociation of bound excitons) the P-band luminescence was observed to increase, giving support to the proposed mechanism. Cingolani *et al* [14] observed a shift in the P-band luminescence to lower energy (363nm) and a broadening of the FWHM as the excitation intensity was increased to 10MW cm^{-2}. Considering the large number of carriers expected to be generated in TEM-CL the near band edge feature at 355-365nm in Figure 6.2 is tentatively attributed to the GaN P-band. Further investigation into dependence of this line on beam current would help to clarify this.

The emission at 385nm has been previously attributed to cubic phase inclusions [18]; it is also within the spectral range of DAP transitions (380-390nm). There is some evidence of phonon replicas [6] in spectrum A suggesting that the peak is due to a DAP transition.

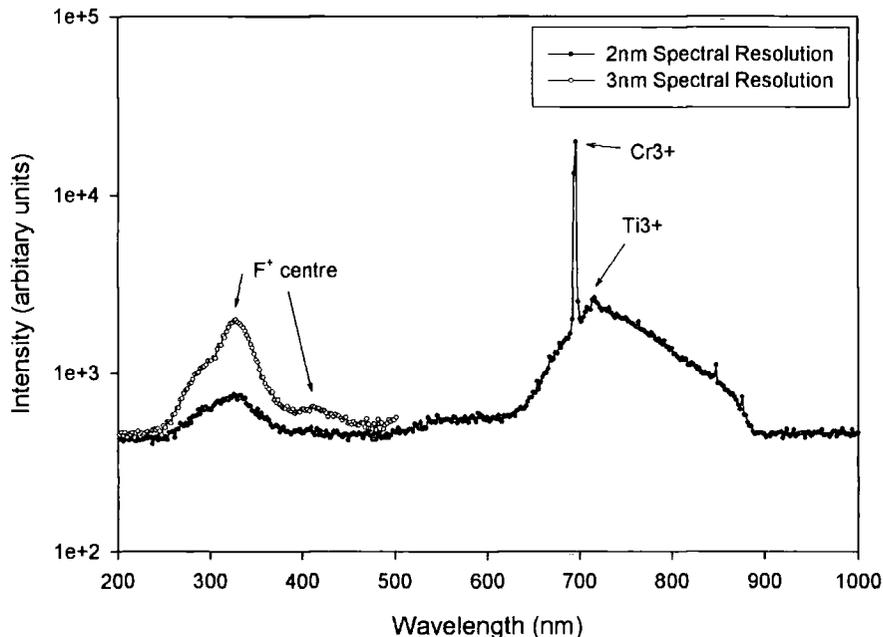**Figure 6.3:**   **TEM-CL spectra of bulk sapphire substrate material (100kV electron beam, cooled to 100K).**

---

[4] The transition to a high excitation regime is broadly considered to take place at a free carrier density of 10^{18} cm^{-3}.

Figure 6.3 shows TEM-CL spectra of a flake from a bulk sapphire substrate recorded in order further to investigate the origins of peaks assigned to the substrate. Since the sample was in bulk form the high CL intensity allowed spectra to be recorded at high spectral resolution (2 and 3nm). Both the impurity, F^+ and F centre peaks are present. The presence of the F^+ centre peaks in both bulk and ion beam thinned samples makes it unlikely that such centres are an artefact of TEM specimen preparation.

6.4.2 Spectral features of M-Plane GaN/LiAlO$_2$
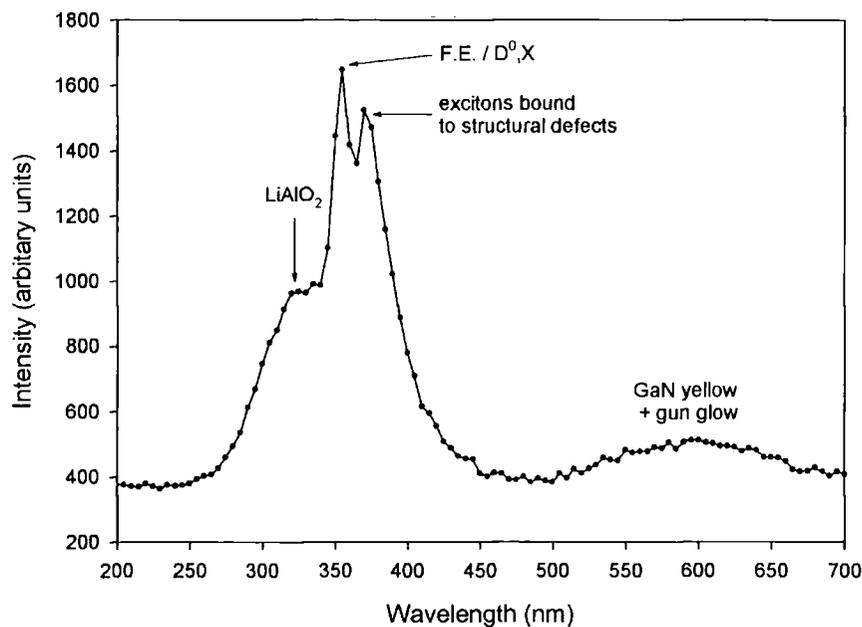
Figure 6.4: TEM-CL spectrum of M-plane GaN epilayer (100kV electron beam, cooled to 100K).

Figure 6.4 shows a typical TEM-CL spectrum taken from a cross-sectional M-plane GaN sample (Table 6.1). The sharp peak at 355nm and the broad peak centred at 600nm are similar to those seen in c-plane GaN and are attributed to free exciton recombination and GaN yellow luminescence respectively. The peak seen at 370nm has been previously attributed to excitons bound to structural defects such as stacking faults or dislocations [2, 29-31]. An investigation into the origins of this peak is presented in Chapter 8.

A peak in a position similar to that identified in 6.4.1 as the sapphire F⁺ centre can be seen in Figure 6.4 at 3.7eV (335nm). Whilst there is little detailed spectroscopy of $LiAlO_2$ in the literature, studies have identified absorption bands in $LiAlO_2$ with similar physical origins to the F⁺ centre absorption band in sapphire [32]. Figure 6.5 shows a TEM-CL spectrum of bulk $LiAlO_2$ taken under conditions identical to those in Figure 6.4. The inset to Figure 6.5 is a SEM-CL spectrum[5] taken from a similar $LiAlO_2$ substrate prior to sample growth.
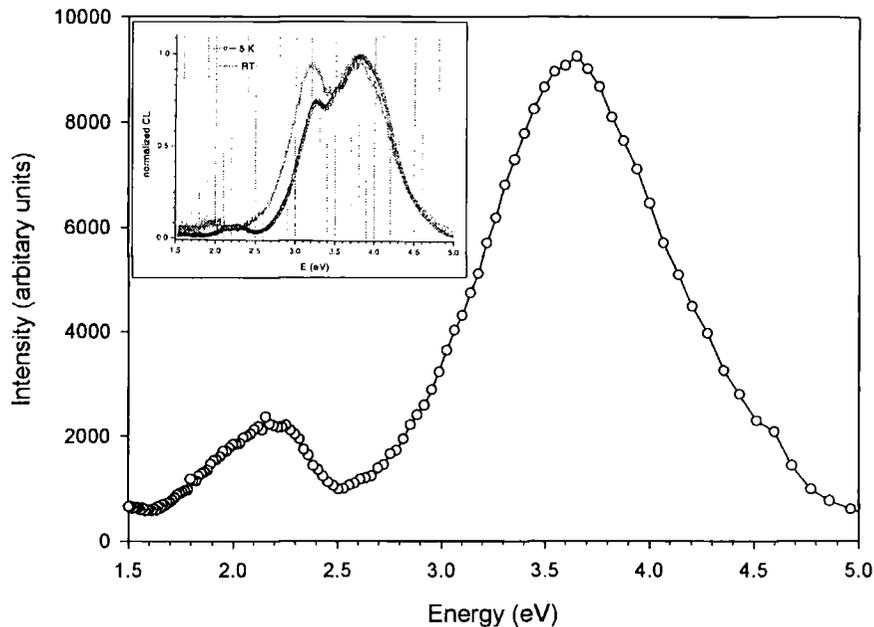
Figure 6.5: **TEM-CL spectrum of LiAlO₂ substrate (100kV electron beam, cooled to 100K). Inset shows a SEM-CL spectrum[5] of a similar substrate.**

Figure 6.5 shows a broad band centred on 3.65eV (340nm) with a less intense band centred at 2.2eV (563nm). The SEM-CL shows the dominant broad band to be centred on 3.8eV (326nm) with a secondary peak at 3.2eV (388nm). The 3.2eV (388nm) emission reduces in intensity relative to the 3.8eV (326nm) as the temperature is changed from room temperature to 5K. This peak is not seen in the TEM-CL spectrum. It might be conjectured that this may be due to some process occurring at higher electron energies that suppresses the 3.2eV (388nm) peak or promotes the 3.8eV (326nm) peak. However, no physical basis for this presumption is suggested.

---

[5] SEM-CL provided courtesy of Achim Trampert at the Paul-Drude Institute, Berlin

It is worth noting that the $LiAlO_2$ substrate material proved to be extremely unstable when illuminated by 80-120keV electrons. It could be seen to move and even crack within seconds of illumination. Carbon, gold coating and liquid nitrogen cooling made no observable difference. Reducing the beam current was effective to some extent, but the current needed to be reduced to almost unusable levels before the material became stable enough for imaging to be attempted.

6.5 Beam Degradation of CL

Electron beam induced degradation of CL has been observed in a number of different III-V and II-VI semiconductors during TEM-CL studies [33-38]. The observed degradation has been attributed to either the creation of non-radiative centres such as point defects, or to the destruction of luminescence centres [34]. Through a simple recombination centre model Ohno *et al* [37] described the degradation and calculated a threshold electron energy for the displacement of atoms from the crystal lattice by displacement or knock-on damage [39]. In the following sections electron beam degradation data are analysed for the panchromatic CL emission from an $In_{0.1}Ga_{0.9}N$ 2QW, the monochromatic emission from an $In_{0.1}Ga_{0.9}N$ SQW and the $LiAlO_2$ substrate discussed in the previous section.

6.5.1 GaN/In$_x$Ga$_{1-x}$N Beam Degradation

Figure 6.6 shows panchromatic-CL degradation curves as a function of time from the $In_{0.1}Ga_{0.9}N$ double quantum well structure described in Table 6.1. The degradation was recorded in both STEM and CTEM modes at operating voltages of 80, 100 and 120kV, using a CTEM beam of diameter 1μm and a 10nm STEM probe scanning an area of approximately 1μm^2. Care was taken to select an unexposed section of foil for each measurement.

Figure 6.6: **Electron beam induced degradation of the panchromatic CL emission versus time from an $In_{0.1}Ga_{0.9}N$ double quantum well in STEM and CTEM modes (cooled to 100K).**

In Figure 6.6 the measured CL emission in CTEM mode can be seen to degrade to around half of its initial intensity over ten minutes. However, only a small reduction in emission is seen in STEM mode. Beam current measurements presented in Table 6.2 suggest that this effect is due to effects of electron dose. Whilst the current density in the illuminated area is approximately two orders of magnitude higher when comparing a static 10nm STEM probe to a 1μm CTEM beam, the total dose in STEM is two orders of magnitude lower than for CTEM when the STEM scan area is the same as the area illuminated by the CTEM beam. This suggests that specimen damage can be avoided by initially investigating newly prepared foils and collecting spectra in STEM mode before using CTEM for diffraction contrast imaging. Further analysis of the CL degradation will now be considered in terms of electron dose rather than time as shown in Figure 6.7.
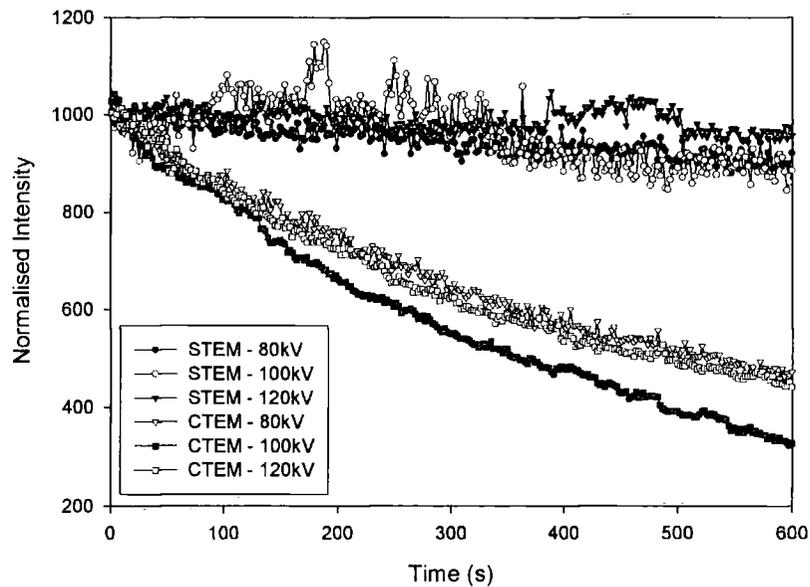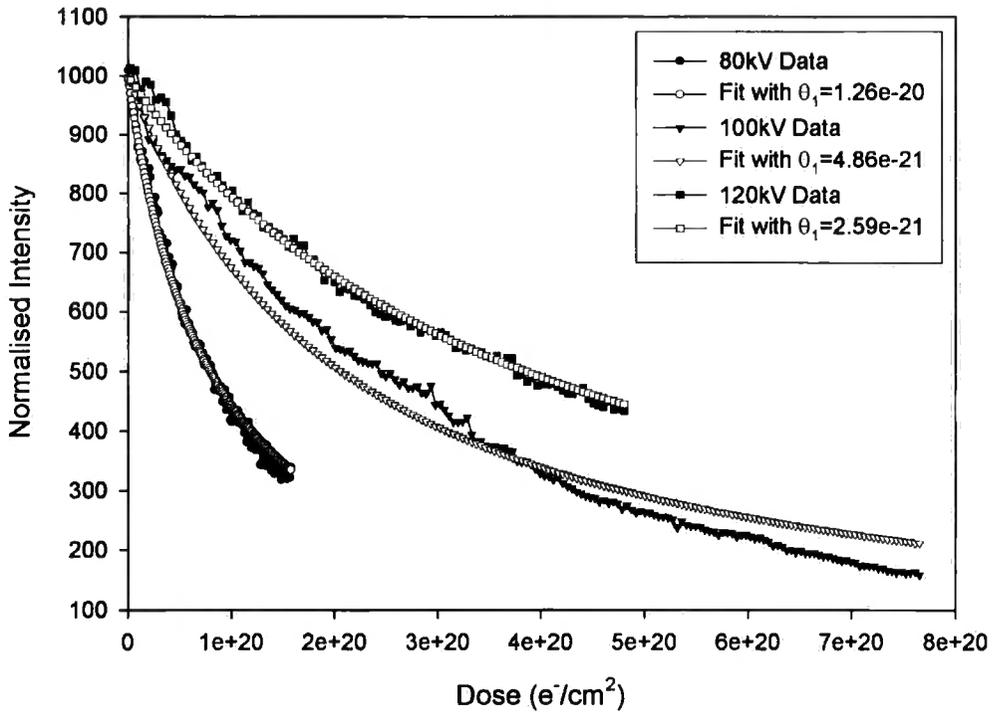
Figure 6.7: **Electron beam induced degradation of the panchromatic CL emission versus dose from an $In_{0.1}Ga_{0.9}N$ double quantum well in CTEM modes (cooled to 100K). Fits to Equation 6.3 are shown with θ_1 values listed in Table 6.4.**

It is reported that CL emission intensity, I_{CL}, is well described by the following function [38]:

$$I_{CL} = \frac{1}{1 + \theta_1 D}$$

(6.3)

where θ_1 is a fit parameter and D is the dose. Figure 6.7 shows the CTEM data from Figure 6.6 fitted to this function on an I_{CL} vs dose plot. The plot shows a good fit between Equation 6.3 and the experimental data. A trend is also noted with the degradation occurring more rapidly as the electron beam energy falls from 120keV to 80keV.

The physical origin of Equation 6.3 can be explained by a recombination-centre model [6]. If the radiative recombination efficiency is, η, then:

$$\eta = \frac{\tau}{\tau_{rr}} = \frac{1}{1 + \frac{\tau_{rr}}{\tau_{nr}}}$$ (6.4)

where τ, τ_{rr}, and τ_{nr} are the minority carrier lifetime, the radiative recombination lifetime, and the non-radiative recombination lifetimes respectively. Making the simplifying assumption that the material contains one type of radiative and multiple non-radiative recombination centres then:

$$\eta = \frac{1}{1 + \frac{\sum_i N_{nr(i)} \sigma_{nr(i)}}{N_{rr} \sigma_{rr}}}$$ (6.5)

where N_{rr} and $N_{nr(i)}$, are the densities of radiative and the ith non-radiative recombination centres; σ_{rr} and $\sigma_{nr(i)}$, are the radiative and i^{th} non-radiative capture cross sections; and V_{th} is the carrier thermal velocity, these being related by $\tau = (N\sigma V_{th})^{-1}$. Making the assumption that $\sigma_{nr(i)}/N_{rr}\sigma_{rr}$ remains constant during irradiation then $N_{nr(i)} = \varepsilon_{(i)} D$ where $\varepsilon_{(i)}$ is the rate of increase of the ith non-radiative centre with dose. Therefore we may deduce that:

$$\theta_1 = \frac{\sum_i \sigma_{nr(i)} \varepsilon_i}{N_{rr} \sigma_{rr}}$$ (6.6)

where θ_1 is the experimental fit parameter in Equation 6.3. The fits in Figure 6.7 therefore support the hypothesis that CL degradation is caused by the incident electron beam introducing non-radiative centres into the material. However, the trend of reduced CL degradation rate with increased beam energy seen in Figure 6.7 still needs to be explained.

	80keV	100keV	120keV
θ_1	1.26×10^{-20} cm²	4.86×10^{-21} cm²	2.59×10^{-21} cm²

Table 6.4: **θ_1 degradation parameters from figure 6.7.**

The discussion of the beam degradation results so far has taken into account the electron dose. It does not, however, take into account the variation

in electron beam-solid interaction cross-section with beam energy. In Section 6.3 (excitation conditions) the energy deposition per unit depth was calculated and shown to be 15% greater at 80keV than at 100keV and 30% greater at 80keV than at 120keV. As can be seen from the tabulated θ_1 values in Table 6.4 the differences in energy deposition rates brings the θ_1 values closer together, but does not explain the more rapid degradation at 80keV.

Comparison with more extensive measurement of θ_1 versus beam energy (Ohno *et al* [38]) for (Ga,In)P is instructive: Ohno's data shows a threshold energy for displacement damage. Below this energy the θ_1 values reported by Ohno et al are similar to those in Table 6.4. Above this energy the θ_1 values are typically of the order of 10^{-19} cm^2 and increase rapidly with beam energy. This suggests that further analysis of the electron beam degradation of GaN would be of interest to determine the threshold value for displacement damage in GaN.
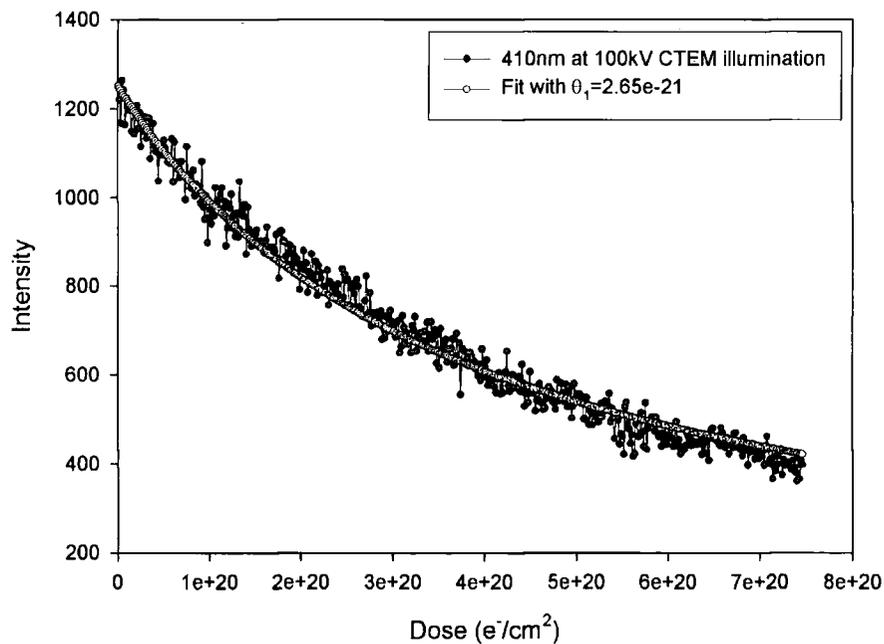
Figure 6.8: **CTEM degradation of In$_{0.1}$Ga$_{0.9}$N single quantum well emission at 410±10nm (100kV electron beam, cooled to 100K).**

The decay of the monochromatic QW emission from an In$_{0.1}$Ga$_{0.9}$N SQW was also investigated as shown in Figure 6.8. The decay curve is well described by Equation 6.3 with a θ_1 value of 2.65×10^{-21} cm^2. This is similar to the panchromatic θ_1 values and shows that there is no need to be concerned about the QW CL decaying faster than the overall CL emission.

6.5.2 Beam Degradation of LiAlO₂

In this section the degradation of the CL from the LiAlO₂ substrate discussed in Section 6.4.2 is reported.

Figure 6.9 shows the decay of the CL emission from the LiAlO₂ centred at 340±20nm. This spectral range contains the majority of the CL intensity (as is detectable by the CL collection system) from the LiAlO₂ (see Figure 6.5). Spectra taken after electron exposure revealed no evidence of peak shifting, only a decline in intensity.
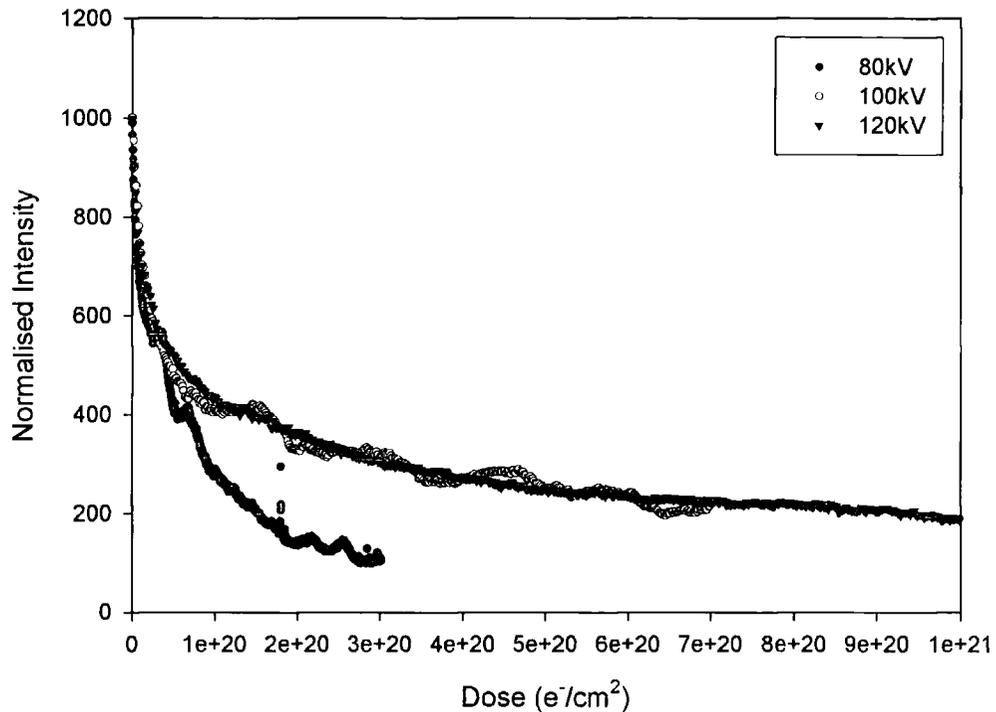
Figure 6.9:   CTEM degradation of LiAlO₂ CL at 340±20nm (cooled to 100K).

The decay curves in Figure 6.9 are characterised by an initial rapid decay followed by a slower rate of decay after a dose of around 2.5×10^{20} electrons/cm². The data was not well described by Equation 6.3. A better fit was found using a logarithmic function; but since this does not relate to a physical model it will not be described further. It is also noted that sample drift resulting from the instability of LiAlO₂ under the electron beam presents a possibly large error. Further study into the behaviour of this important substrate material would be of benefit.

6.6 Conclusions

Calculations based upon single and multiple scattering assumptions have been used to investigate the energy deposited in a GaN TEM foil by an electron beam of energy 80-120keV. It was then demonstrated that the energy deposition rate is high enough to allow an electron-hole plasma to form. Evidence of this plasma was seen in the GaN near band edge region with CL emission characteristic of free exciton interactions as described in Section 6.4.1.

C-plane GaN/$In_xGa_{1-x}N$ QW structures grown on sapphire and M-plane GaN epilayers grown on $LiAlO_2$ were investigated. A broad CL emission band at 330nm was seen in spectra taken from cross-sectional c-plane GaN TEM foils and was identified as the sapphire F^+ centre peak. The F^+ centre consists of an oxygen vacancy which has trapped a single electron and is thought to be formed through electron beam damage. This peak was observed when the substrate was not directly illuminated and is thought to be excited through secondary processes such as x-ray emission or fast secondary electrons. Spectra taken from both the substrate and epilayer side of a plan view TEM foil showed the F^+ centre peak was absorbed by ~1μm of GaN.

CL emission from GaN/$In_xGa_{1-x}N$ epilayers was observed to degrade under illumination from 80-120keV electrons. At the electron dose levels investigated (up to 10^{21} e-/cm^2) the degradation process was shown to be consistent with the introduction of non-radiative recombination centres. The rate of CL degradation was shown to be of a similar magnitude at beam energies of 80-120keV. Monochromatic CL emission from an $In_{0.1}Ga_{0.9}N$ SQW was shown to degrade at a similar rate to panchromatic CL. The lower STEM dose rate in comparison to that of CTEM was demonstrated to degrade the CL from GaN at a much slower rate and is therefore recommended for initial specimen investigations and spectral acquisition/imaging before diffraction contrast imaging.

6.7 References

1.   Waltereit, P., O. Brandt, M. Ramsteiner, A. Trampert, H.T. Grahn, J. Menniger, M. Reiche, and K.H. Ploog, *M-plane GaN(1-100) Grown on γ-LiAlO₂(100): Nitride Semiconductors Free of Internal Electrostatic Fields*, Journal of Crystal Growth **227-228** (2001) 437-441.

2.   Sun, Y.J., O. Brandt, U. Jahn, T.Y. Liu, A. Trampert, S. Cronenberg, S. Dhar, and K.H. Ploog, *Impact of Nucleation Conditions on the Structural and Optical Properties of M-Plane GaN(1-100) Grown on γ-LiAlO₂*, Journal of Applied Physics **92** (2002) 5714-5719.

3.   Deatcher, C.J., C. Liu, S. Pereira, M. Lada, A.G. Cullis, Y.J. Sun, O. Brandt, and I.M. Watson, *In Situ Optical Reflectometry Applied to Growth of Indium Gallium Nitride Epilayers and Multi Quantum Well Structures*, Semiconductor Science and Technology **18** (2003) 212-218.

4.   Hurst, P., P. Dawson, S.A. Levetas, M.J. Godfrey, I.M. Watson, and G. Duggan, *Temperature Dependent Optical Properties of InGaN/GaN Quantum Well Structures*, Physica Status Solidi B **228** (2001) 137-140.

5.   Pereira, S., E. Pereira, E. Alves, N.P. Barradas, K.P. O'Donnell, C. Liu, C.J. Deatcher, and I.M. Watson, *Depth Profiling InGaN/GaN Multiple Quantum Wells by Rutherford Backscattering: The Role of Intermixing.*, Applied Physics Letters **81** (2002) 2950-2952.

6.   Yacobi, B.G. and D.B. Holt, *Cathodoluminescence Microscopy of Inorganic Solids*, (Plenum Press, New York, 1990).

7.   Monemar, B., *Optical Properties of GaN*, in *Gallium Nitride (GaN) I*, J.I. Pankove and T.D. Moustakas, (Academic Press, San Diego, 1998).

8.   Bethe, H.A. and J. Ashkin, *Passage of Radiations Through Matter*, in *Experimental Nuclear Physics*, E. Segre, (John Wiley & Sons, Inc., New York, 1953).

9.   Krane, K.S., *Introductory Nuclear Physics*, (John Wiley & Sons, Inc., New York, 1988).

10.   Joy, D.C., *Monte Carlo Modeling for Electron Microscopy and Microanalysis*, (Oxford Univeristy Press, Inc., New York, 1995).

11.   Klein, C.A., *Bandgap Dependence and Related Features of Radiation Ionization Energies in Semiconductors*, Journal of Applied Physics **39** (1968) 2029-2038.

12.   Dai, R., W. Zhuang, K. Bohnert, and C. Klingshirn, *Photoluminescence and Gain Spectroscopy of Highly Excited Epitaxial GaN-Layers*, Zeitschrift fur Physik B - Condensed Matter **46** (1982) 189-192.

13.   Hvam, J.M. and E. Ejder, *New Emission Line in Highly Excited GaN*, Journal of Luminescence **12/13** (1976) 611-615.

14. Cingolani, R., M. Ferrara, and M. Lugara, *Electron-Hole Plasma Generation in Gallium Nitride,* Solid State Communications **60** (1986) 705-708.

15. Kurai, S., A. Kawabe, T. Sugita, S. Kubo, Y. Yamada, T. Taguchi, and S. Sakai, *Excitonic Emissions under High Excitation of Hexagonal GaN Single Crystal Grown by Sublimation Method,* Japanese Journal of Applied Physics **38** (1999) L102-L104.

16. Dhar, S., U. Jahn, O. Brandt, P. Waltereit, and K.H. Ploog, *Influence of Exciton Localization on the Quantum Efficiency of GaN/(In,Ga)N Multiple Quantum Wells Grown by Molecular-Beam Epitaxy,* Applied Physics Letters **81** (2002) 673-675.

17. Jahn, U., S. Dhar, O. Brandt, H.T. Grahn, K.H. Ploog, and I.M. Watson, *Exciton Localization and Quantum Efficiency - A Comparative Cathodoluminescence Study of (In,Ga)N/GaN and GaN/(Al,Ga)N Quantum Wells,* Journal of Applied Physics **93** (2003) 1048-1053.

18. Salviati, G., N. Armani, C. Zanotti-Fregonara, E. Gombia, M. Albrecht, H.P. Strunk, M. Mayer, M. Kamp, and A. Gasparotto, *Deep Level Related Yellow Luminescence in P-Type GaN Grown by MBE on (0001) Sapphire,* MRS Internet Jounal of Nitride Semiconductor Research **5S1** (2000) W11.50.

19. Song, J.J. and W. Shan, *Optical Properties and Lasing in GaN,* in *Group III Nitride Semiconductor Compounds,* B. Gil, (Oxford University Press, Oxford, 1998).

20. Garlick, G.F.J., *Luminescent Materials,* (Oxford University Press, London, 1949).

21. Chapoulie, R., C. Capdupuy, M. Schvoerer, and F. Bechtel, *Cathodoluminescence and Crystal Growth of Sapphire,* Physica Status Solidi A **171** (1999) 613-621.

22. Lee, K.H. and J.H. Crawford, *Electron Centers in Single-Crystal Al_2O_3,* Physical Review B **15** (1977) 4065-4070.

23. Lee, K.H. and J.H. Crawford, *Luminescence of the F Center in Sapphire,* Physical Review B **19** (1979) 3217-3221.

24. Draeger, B.G. and G.P. Summers, *Defects in Unirradiated a-Al_2O_3,* Physical Review B **19** (1979) 1172-1177.

25. Caulfield, K.J. and R. Cooper, *Luminescence from Electron-Irradiated Sapphire,* Physical Review B **47** (1993) 55-61.

26. Ghamnia, M., C. Jardin, L. Martinez, M. Bouslama, and P. Durupt, *Electronic Spectroscopy (AES, EELS) and Cathodoluminescence (CL) for a-Al_2O_3 Characterization,* Vacuum **48** (1997) 129-134.

27. Tanabe, T., S. Muto, and S. Tohtake, *Development of New TEM Specimen Holder for Cathodoluminescence Detection,* Journal of Electron Microscopy **515** (2002) 311-313.

28. Williams, D.B. and C.B. Carter, *Transmission Electron Microscopy - Spectrometry*, (Plenum Press, New York, 1996).

29. Rieger, W., R. Dimitrov, D. Brunner, E. Rohrer, O. Ambacher, and M. Stutzmann, *Defect-Related Optical Transitions in GaN*, Physical Review B **54** (1996) 17596-17602.

30. Eckey, L., J.-C. Holst, P. Maxim, R. Heitz, A. Hoffmann, I. Broser, B.K. Meyer, C. Wetzel, E.N. Mokhov, and P.G. Baranov, *Dynamics of Bound-Exciton Luminescences from Epitaxial GaN*, Applied Physics Letters **68** (1996) 415-417.

31. Wetzel, C., S. Fischer, J. Kruger, E.E. Haller, R.J. Molnar, T.D. Moustakas, E.N. Mokhov, and P.G. Baranov, *Strongly Localized Excitons in Gallium Nitride*, Applied Physics Letters **68** (1996) 2556-2558.

32. Auvray-Gely, M.H., A. Perez, and A. Dunlop, *Electron Paramagnetic Resonance and Optical Absorption Studies of Irradiated Lithium Aluminate*, Philosophical Magazine B **57** (1988) 137-148.

33. Yamamoto, N., *Characterization of Crystal Defects by Cathodoluminescence Detection System Combined with TEM*, Transactions of the Japan Institute of Metals **31** (1990) 659-665.

34. Mitsui, T., N. Yamamoto, K. Takemoto, and O. Nittono, *Cathodoluminescence and Electron Beam Irradiation Effect of Porous Silicon Studied by Transmission Electron Microscopy*, Japanese Journal of Applied Physics **33** (1994) L342-L344.

35. Ohno, Y. and S. Takeda, *Study of Electron-Irradiation-Induced Defects in GaP by In-situ Optical Spectroscopy in a Transmission Electron Microscope.*, Journal of Electron Microscopy **45** (1996) 73-78.

36. Mitsui, T. and N. Yamamoto, *Deep Level Emission in ZnS Caused by Elecron Beam Irradiation Studied by Cathodoluminescence Measurement System*, Japanese Journal of Applied Physics **37** (1998) L1390-L1392.

37. Ohno, Y. and S. Takeda, *Optical Properties of Anti-Phase Boundaries and Frenkel-Type Defects in CuPt-Ordered GaInP Studied by Optical Spectroscopy in a Transmission Electron Microscope*, Institute of Physics Conference Series **164** (1999) 175-178.

38. Ohno, Y., Y. Kawai, and S. Takeda, *Vacancy-Migration-Mediated Disordering in CuPt-Ordered (Ga,In)P Studied by In Situ Optical Spectroscopy in a Transmission Electron Microscope*, Physical Review B **59** (1999) 2694-2699.

39. Williams, D.B. and C.B. Carter, *Transmission Electron Microscopy - Basics*, (Plenum Press, New York, 1996).

Chapter 7

STEM-CL Imaging of Quantum Wells

7.1 Introduction

Models for and evidence of localisation of luminescence from $In_xGa_{1-x}N$ QW's are reviewed in detail in Section 3.5. A number of authors [1-3] attribute this localisation to a degree of InN-GaN segregation occurring within the QWs. Contrary to this view Albrecht *et al's* STEM-CL imaging [4] revealed no evidence of inhomogeneity in the CL emission from $In_{0.1}Ga_{0.9}N$ QWs already shown to exhibit nanometer scale indium clustering, hence providing evidence for a model whereby $In_xGa_{1-x}N$ optical properties are governed by atomic short range order, rather than nanometer indium clustering.

In this chapter STEM-CL images from electron transparent $In_{0.1}Ga_{0.9}N$ QW samples are presented. The effect that specimen thickness would have on the contrast seen in CL images is investigated and a model is developed to predict the expected CL intensity from a region of particular thickness. By correlating the transmitted intensity in STEM mode to the specimen thickness through the dynamical theory of electron diffraction, the expected CL emission can be compared to the observed CL emission. This process allows contrast due to thickness to be eliminated leaving only the contrast due to material effects.

Panchromatic and monochromatic imaging, and line-scans, are utilised to investigate the CL emission from $In_{0.1}Ga_{0.9}N$ SQWs.

7.2 STEM-CL Imaging

Results presented in this chapter are taken from cross-sectional TEM foils prepared from the same MOVPE-grown $In_{0.1}Ga_{0.9}N$ SQW wafer (details in Table 6.1). STEM-CL imaging of MQW samples showed similar contrast features to the SQW. However, there is an advantage to be gained by using a SQW over a MQW sample for the unambiguous interpretation of CL line scans, therefore SQW results have been used throughout this chapter for consistency.
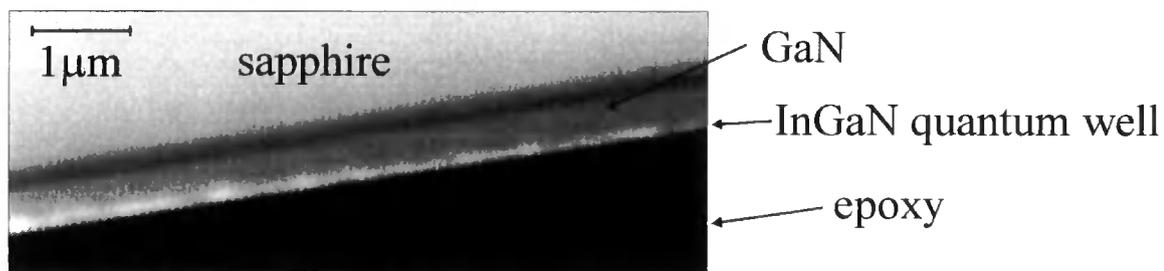
Figure 7.1: Panchromatic STEM-CL image (100kV beam, cooled to 100K).

Figure 7.1 shows a panchromatic STEM-CL image of an $In_{0.1}Ga_{0.9}N$ SQW as described above. A region of brighter contrast can be seen from the outermost surface of the GaN where the SQW is located. Monochromatic STEM-CL imaging shows this bright contrast to be due to emission at 410nm, in agreement with the emission wavelength of the SQW as determined by PL[1]. Closer inspection of Figure 7.1 shows that the bright CL emission from the SQW appears to be inhomogeneous on a sub-micron scale. In the following analysis the effect that foil thickness may have on this contrast is evaluated and discussed along with other factors which may affect the homogeneity of CL emission.

---

[1] PL measurements performed by P. Dawson, UMIST.

7.3 Thickness Dependence of STEM Signal: Model and Experiment.

In this section an equation for transmitted electron intensity versus thickness is written for the case of STEM imaging with weak diffraction contrast. Fitting this equation to experimental data obtained from wedge shaped samples enabled the thickness of a given point on a sample to be evaluated.

The dynamical theory of electron diffraction [5] describes wavefunctions in the crystal lattice as two Bloch waves periodic with the lattice. Bloch wave 1 is defined as being localised at nodes between atomic positions and wave 2 is localised at atomic positions and is therefore strongly scattered. The interference of these waves with one another, see Figure 7.2, gives rise to thickness fringes. When Bloch wave 2 is de-selected it appears to be effectively absorbed. The remaining Bloch wave is less strongly scattered and forms the image when the crystal is relatively thick.

The following formulae for the transmitted intensity, *T*, and the reflected intensity, *R*, have been derived for the two beam case [6]:

$$T = \frac{e^{-\mu_0 z}}{2(1+w^2)}\left[(1+2w^2)\cosh\frac{\mu_g z}{\sqrt{1+w^2}} + 2w\sqrt{1+w^2}\sinh\frac{\mu_g z}{\sqrt{1+w^2}} + \cos(2\pi\frac{\sqrt{1+w^2}}{\xi_g}z)\right] \qquad (7.1a)$$

$$R = \frac{e^{-\mu_0 z}}{2(1+w^2)}\left[\cosh\frac{\mu_g z}{\sqrt{1+w^2}} - \cos(2\pi\frac{\sqrt{1+w^2}}{\xi_g}z)\right] \qquad (7.1b)$$

In which $\mu_g = \frac{2\pi}{\xi_g'}$, $\mu_0 = \frac{2\pi}{\xi_0'}$, w is the deviation from the Bragg condition, z is the specimen thickness, ξ_g is the extinction distance in the material, ξ_0' is the mean absorption distance and ξ_g' is the anomalous absorption distance. At the reflecting position ($w = 0$) the difference between the two absorption coefficients is a maximum and the effect is most extreme when $\xi_g' = \xi_0'$, i.e. letting the parameter $(\xi_0'/\xi_g') = x = 1$. This condition implies that the absorptive power is

distributed in the crystal lattice like delta functions at the atomic positions. For electrons it has often been assumed that $\xi'_g = \xi'_0$ and $(\xi_g / \xi'_g) = y = 0.1$ in calculations of diffraction contrast.
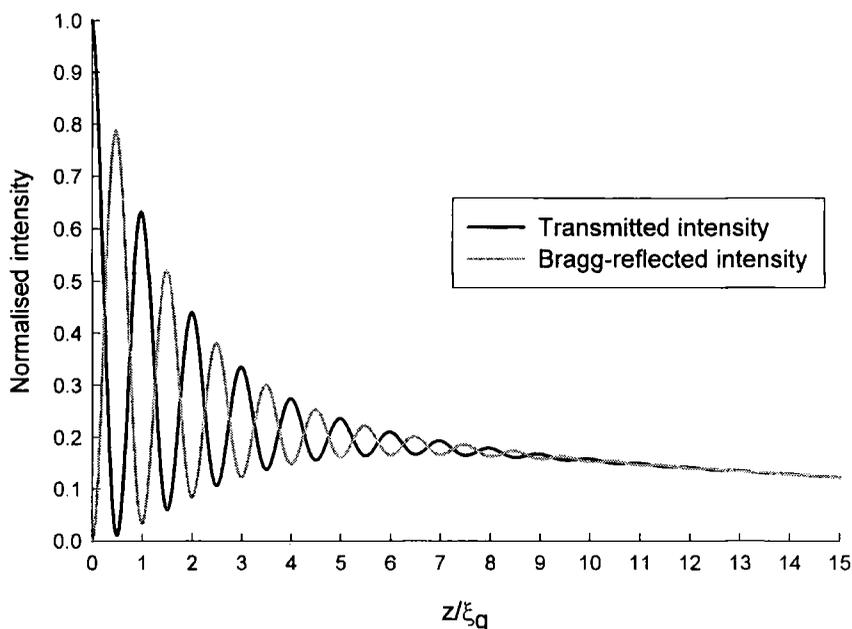
Figure 7.2: **Transmitted and diffracted electron intensities calculated as a function of thickness using Equation (7.1), (x = 0.9, y = 0.075).**

Figure 7.2 shows the relationship between the reflected and transmitted waves as described by Equation 7.1. The detected STEM intensity in the microscope is not made up purely of direct beam electrons because of the collection angle of the detector and deviation from the two beam condition. A factor, *r*, is now introduced to allow for a fraction of the diffracted beam to be added to the direct beam to simulate real intensities. The total intensity recorded by an on-axis STEM detector is therefore the transmitted intensity, *T*, plus a fraction, *r*, of the reflected intensity, *R*:

$$I = T + rR \tag{7.2}$$

In this work a relationship between the thickness and observed CL intensity was determined experimentally as follows:

1. A uniform wedge was identified from smooth STEM contrast and periodic extinction contours.

2. The intensity versus position on the wedge was measured (in practice the intensity from strips of equal thickness was summed to reduce statistical noise).

3. The intensity profile along the wedge was fitted to Equation 7.2.

4. Each cycle of oscillatory contrast corresponds to an extinction distance. Hence the fitting allows the thickness of the wedge to be estimated at each position.

In practice the STEM imaging requirements for the fitting procedures are contradictory. (i) It is desirable to eliminate diffraction contrast due to defects and bending so as to isolate thickness-only dependent intensity changes. This can be achieved by monitoring combined intensities of direct and diffracted waves; (ii) to carry out the fitting, oscillatory thickness fringes should be present in the intensity profile but the contrast is weakened in the combined direct/diffracted beam images.

Figure 7.3(a) shows a STEM image of the region selected for the above calibration procedure. Figure 7.3(b) shows the corresponding intensity profile fitted to Equation 7.2 using $x = 0.9$, $y = 0.075$ and $r = 0.9$, i.e. 100% of the direct and 90% of the diffracted wave intensities. Although the oscillatory contrast was weak the envelope plus residual fringe contrast contains enough information to make a fit. The thickness for each position along the sample is based on this fit. As can be seen in Figure 7.2 the rate of change of intensity with thickness decreases rapidly with increasing thickness. If the error in the thickness is based upon counting statistics ($\sqrt{N}$) from the STEM intensity this will result in a low error for thin specimens and higher error for thick specimens.

(a)

(b)
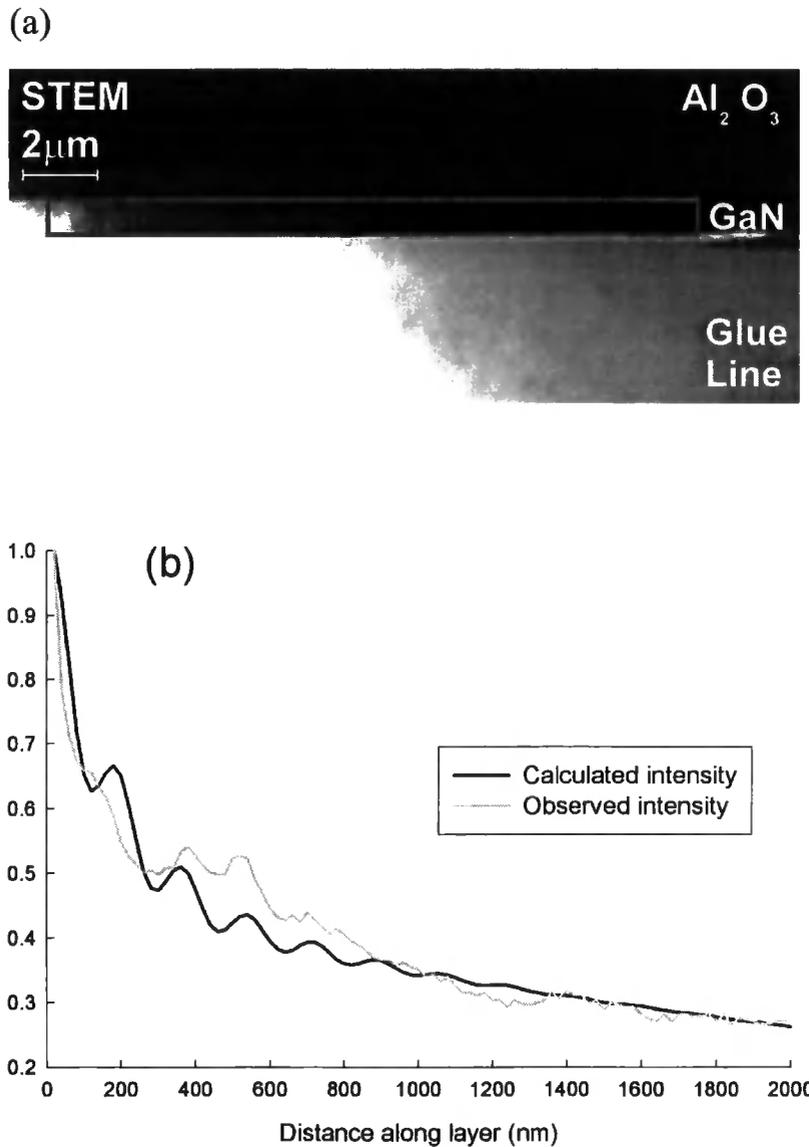
Figure 7.3: **Transmitted electron intensity for a GaN wedge-shaped foil. (a) 120kV STEM image of GaN, (b) Calculated and recorded transmitted electron intensity along the GaN layer.**

7.4 Thickness Dependence of CL: Model

A model of the CL intensity expected from thin foils is now presented that takes into account the relationship of CL intensity to excess carrier density, surface recombination and the generation function.

Cathodoluminescence emission results from the radiative recombination of excess carriers between participating states. The total CL emission, L_{CL}, is

94

linearly dependent on the excess carrier density, Δn, as shown in Equation 7.3 [7]:

$$L_{CL}(r) = \int_V f \frac{\Delta n(r)}{\tau_{rr}} d^3 r \qquad (7.3)$$

where, τ_{rr} is the radiative recombination lifetime, and f is a correction parameter for losses in the CL detection process. 'f accounts for the efficiency of the photomultiplier, the transmission of the monochromator, reflection and absorption in the sample (see Chapter 5). Here it has been assumed that these terms are constant across the area scanned.

In very thin specimens surface recombination is important in CL emission [7]. The surface recombination rate can be described as:

$$s\Delta n = D\left|\frac{\partial \Delta n}{\partial z}\right|_{z=0} \qquad (7.4)$$

where s is the surface recombination velocity, and D is the diffusion coefficient. The solution of Equation 7.4 by van Roosbroeck [8] shows the loss due to surface recombination scales as exp(-z/L), where L is the minority carrier diffusion length. This implies that all the carriers generated at the surface of the semiconductor are lost to surface recombination whereas this reduces to approximately one third at a depth of one diffusion length.

Since a wide range of thicknesses needs to be considered it is also necessary to model the generation of carriers. In this analysis the depth dependent generation rate has been evaluated using the empirical depth-dose formula by Everhart and Hoff [9]:

$$g(u) = 0.60 + 6.21u - 12.40u^2 + 5.69u^3 \qquad (7.5)$$

where $u = z/R_e$ and z is the depth of the sample, R_e is the range of the electron penetration, in this case calculated by the Kanaya and Okayama method [10].

(a)

(b)
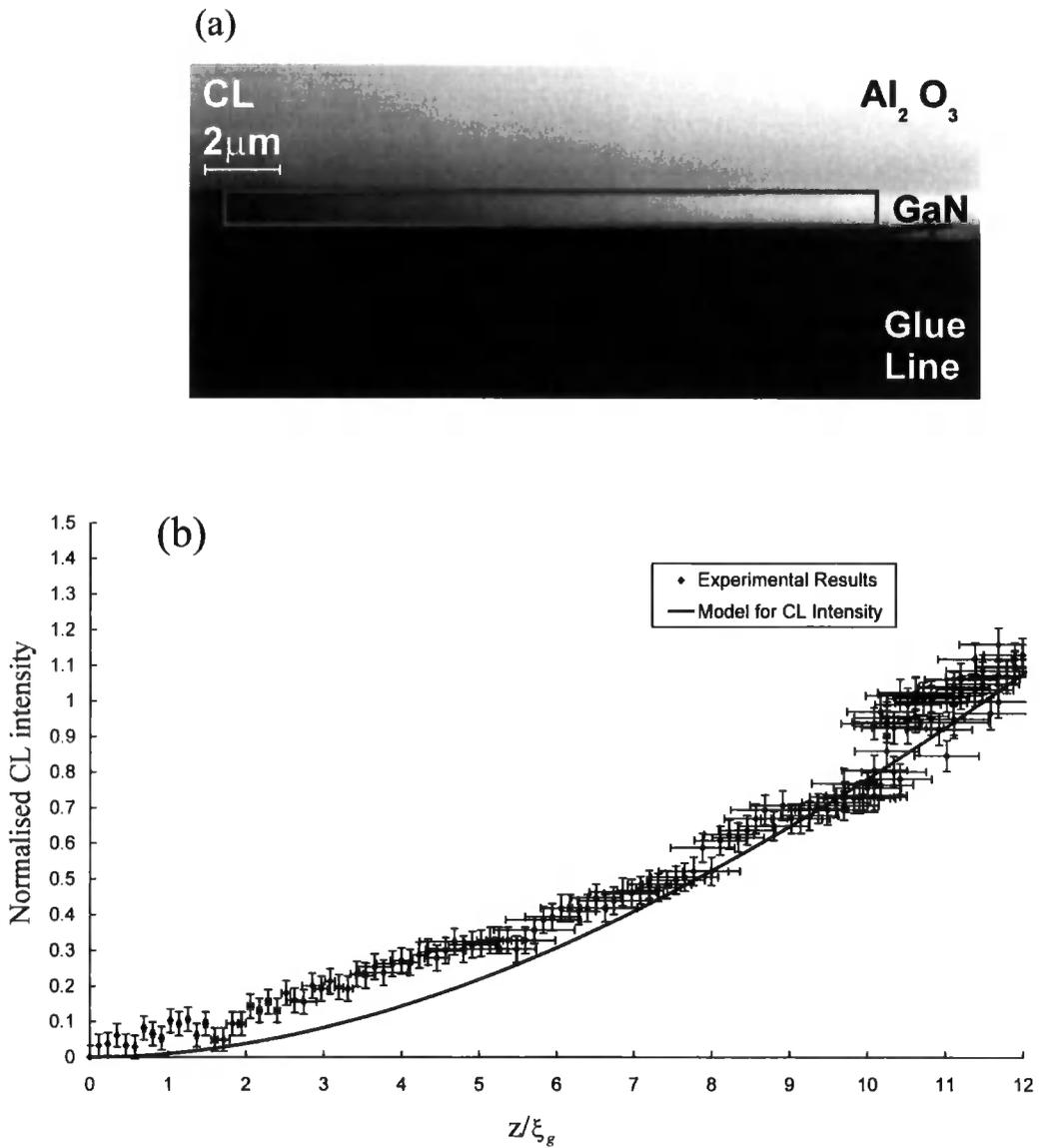
Figure 7.4: **Panchromatic cathodoluminescence of the GaN wedge shown in Figure 2(a). (a) CL image, (b) CL linescan of the intensity along the GaN layer comparing the analytical model (solid line) and the experimental data.**

The product of the loss due to surface recombination and the local generation rate was evaluated numerically at incremental thicknesses. In these calculations the minority carrier diffusion length was taken to be 0.5μm this being the median value from the literature [11-18]. The modelled CL emission for specimens of varying thickness was evaluated numerically and is plotted in Figure 7.4.

7.5 Thickness Dependence of CL: Comparison of Model with Experiment

Figure 7.4(b) shows the comparison of the CL generation model with the experimental data plotted as CL intensity, L_{CL} vs z/ξ_g. The thickness was estimated using the data in Figure 7.3(b) whilst the experimental values of L_{CL} were extracted from Figure 7.4(a) along the wedge section indicated. As for the STEM intensities, the CL values used were summed for each wedge thickness to reduce noise. These values are plotted with their associated counting errors. Horizontal error bars represent the estimated error in thickness as described in Section 7.3.

The general shapes of the experimental and modelled forms of L_{CL} versus thickness are in agreement. In the next section this relationship is used to normalise a CL image for thickness using the STEM intensity as a reference signal.

7.6 Panchromatic Imaging of $In_{0.1}Ga_{0.9}N$ Quantum Wells

7.6.1 Normalisation of Images

The technique of using the STEM intensity to infer the absolute sample thickness and hence the expected CL has been used to re-scale and interpret the luminescence contrast from an $In_{0.1}Ga_{0.9}N$ quantum well. This has been done in two directions, both across the well (Figure 7.5) and along the well (Figure 7.6).
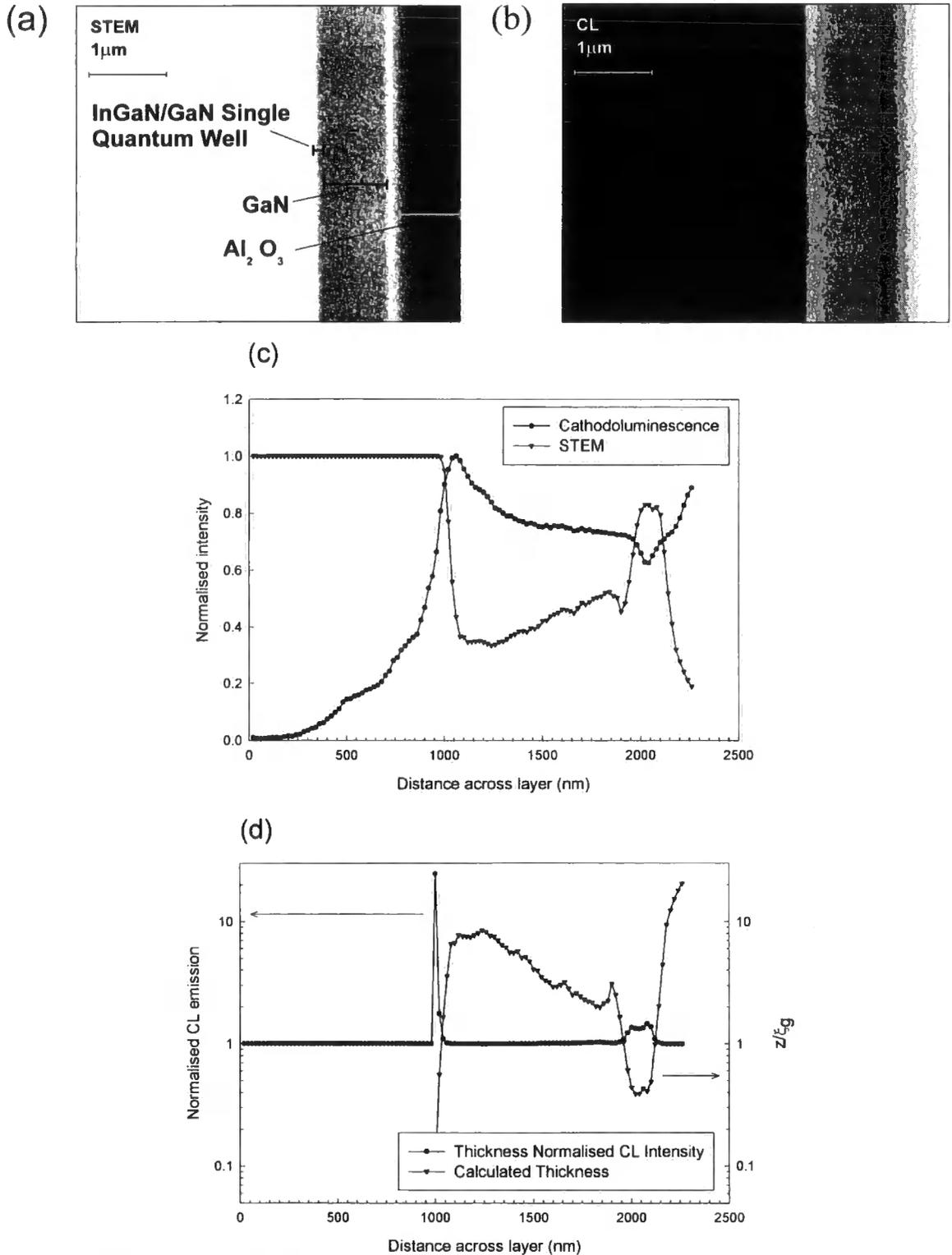
Figure 7.5: **Normalisation of the CL image intensity for thickness variation in a GaN/GaN/Al$_2$O$_3$ structure. (a) STEM image of cross-sectional In$_{0.1}$Ga$_{0.9}$N quantum well in GaN, (b) panchromatic CL image of (a), (c) CL and STEM line scans across the sample, (d) calculated specimen thickness and CL intensity normalised using the thickness-intensity relation in Figure 7.3(b).**

Figure 7.5(a) shows a STEM image of a cross section of an $In_{0.1}Ga_{0.9}N$ quantum well on GaN, and Figure 7.5(b) shows the corresponding panchromatic CL image. Figure 7.5(c) shows line-scans of the STEM and CL intensity running across Figures 7.5(a) and 7.5(b) respectively. Each point on the line-scans is the sum of each vertical row of pixels in their respective images. The CL line-scan reaches a peak value at the position of the quantum well and declines down towards the interface between the GaN and sapphire substrate. The STEM line-scan shows maximum transmission with the beam off the sample which rapidly decreases to a local minimum value (representing increased thickness) on the edge of the GaN layer before increasing towards the interface between the GaN and sapphire. (The decreased thickness at the GaN/sapphire interface is thought to result from preferential thinning of the GaN nucleation layer).

Figure 7.5(d) shows the calculated thicknesses (see Section 7.3) across the layer and the CL intensity values expected for these thicknesses from the model in Section 7.4, the latter being normalised by dividing the experimental value by the intensity expected from calculation. Deviation from unity indicates contrast effects that are not thickness artefacts at the position of the quantum well and to a lesser degree at the interface between the GaN and the sapphire substrate. Since the normalisation process is for GaN, enhanced normalised luminescence from the quantum well (here by a factor of x12) is expected. The normalisation implicitly assumes that the foil thickness at the quantum well position is the same as in the adjacent GaN. Errors arising from diffraction contrast at the quantum well are expected to be negligible since the well width (2.5nm) is small compared to the probe width (~10nm). However, the increased value of the normalised luminescence at the interface region between the GaN and the sapphire could be attributed to some property of the nucleation layer itself. But since the model for the CL intensity slightly underestimates the observed CL emission for very thin sections (see Figure 7.4(b)) this systematic error may account for the apparent enhanced luminescence of this layer.
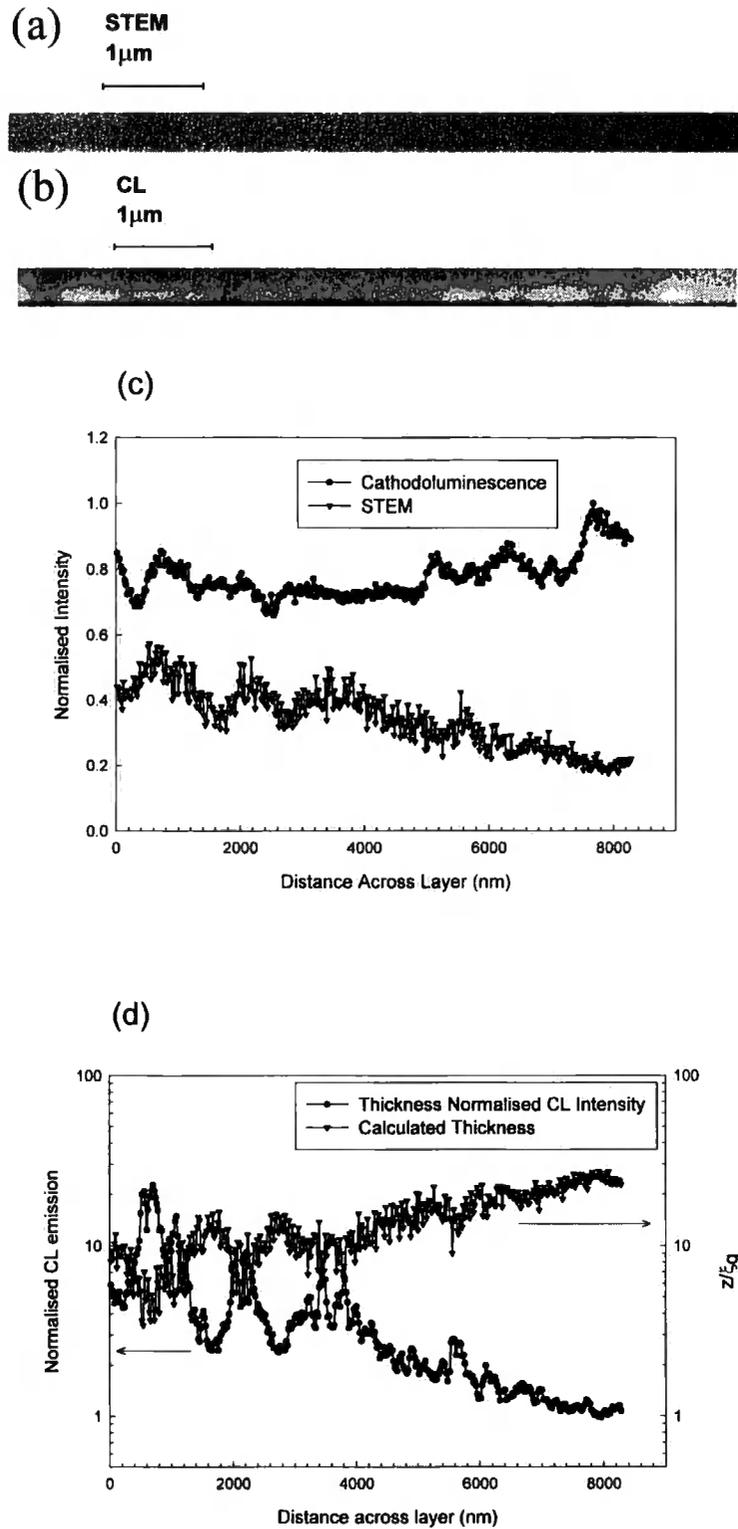
Figure 7.6: **Normalisation of the variation in CL emission along the length of a $In_{0.1}Ga_{0.9}N$ quantum well. (a) STEM image along the length of the quantum well, (b) panchromatic CL image of (a), (c) CL and STEM line scans along sample, (d) calculated specimen thickness and CL intensity normalised using the thickness-intensity relation in Figure 7.3(b).**

A similar normalisation process was used to assess the contrast along the length of a quantum well as shown in Figure 7.6. While the STEM image of Figure 7.6(a) shows some variation in thickness, the CL image (Figure 7.6(b)) shows strong zones of contrast with a length scale of ~0.7μm. In order to normalise the contrast from the $In_{0.1}Ga_{0.9}N$ quantum well, the thickness variation of the TEM foil at the well position was estimated using the STEM image intensity from the GaN barrier. The inferred GaN thickness variation is shown in Figure 7.6(d) – the thickness increases from the left to the right of the image. The result of normalising the CL line scan in Figure 7.6(c) is shown in Figure 7.6(d).

7.6.2. Discussion

Application of the technique developed for the normalisation of STEM-CL images for the effects of thickness has shown that contrast observed in QW emission on a scale of ~0.7μm is not solely a function of thickness. Errors in the normalisation might be expected to occur due to uncertainties in the thickness of the foil as determined from STEM intensity and from underestimation of the CL intensity by the model for thin samples. Both can be seen in Figure 7.4(b). In the application of this process to $In_{0.1}Ga_{0.9}N$ QWs in GaN it has been necessary to evaluate the thickness of the GaN and to assume that the foil in the well position is the same.

Possible causes of CL contrast from a uniformly luminescent sample are surface contamination or artefacts of sample preparation. A common surface contaminant is a carbon-rich, polymerised film formed through the radiation damage of adsorbed hydrocarbon molecules on the specimen surface [6]. Inspection of Figure 7.1 shows that the GaN luminescence appears uniform whilst the QW at the epilayer's surface exhibits inhomogeneous contrast. If it is supposed, therefore, that the cause of CL contrast is not contamination of a uniform sample, then it is possible that it results from a non-uniform sample. This non-uniformity may take the form of luminescence 'hot spots' in the material which have been selected in the TEM foil. Comparison of the experimental and normalised CL intensities (Figures 7.6(c) and (d)) gives some insight into the distribution of these hot spots in the plane of the quantum well: Since the intensities of the main peaks in the CL image are comparable, each may be

assumed to be due to *one* hot spot contained in the thickness of the TEM foil. Normalisation of the image for thickness effects emphasises the peaks on the left over the ones on the right, since while both represent the result of excitation of a similar 'hot spot', the ones on the left are embedded in a thinner part of the TEM foil.

To investigate further the phenomena of non-uniform QW luminescence monochromatic imaging and line-scans have been utilised in the following section.

7.7 Monochromatic Analysis of $In_{0.1}Ga_{0.9}N$ QWs

7.7.1 Monochromatic Imaging

Monochromatic imaging affords the possibility of spatially resolving the luminescent centres emitting at particular wavelengths. Moving from a regime of panchromatic to monochromatic imaging results in a much lower count rate; the available signal can be adjusted by increasing or decreasing the spectral resolution. For this reason slightly thicker sections of the TEM foil were investigated. The increased thickness also resulted in a smaller dependence of the CL emission on changes in foil thickness, therefore the normalisation process has not been applied to the images and line-scans in this section.

An additional factor to account for is integration time. During spectral acquisition with a resolution of 5nm integration times of 1-5s were typical. The *Link ISIS* software has a maximum integration time of 0.01 seconds/pixel for CL imaging - operationally a maximum integration time much greater than this would be impractical as a 500 pixel square image takes approximately 40 minutes to acquire with a 0.01s integration time. To work around this experimental limitation it was necessary to set the monochromator slits at 1mm, corresponding to 21.6nm dispersion.

(a)

(b) 405nm
2μm

(c) 410nm
2μm

(d) 415nm
2μm

Intensity

1200
1100
1000
900
800
700
600
500

370 380 390 400 410 420 430 440 450 460 470
Wavelength (nm)
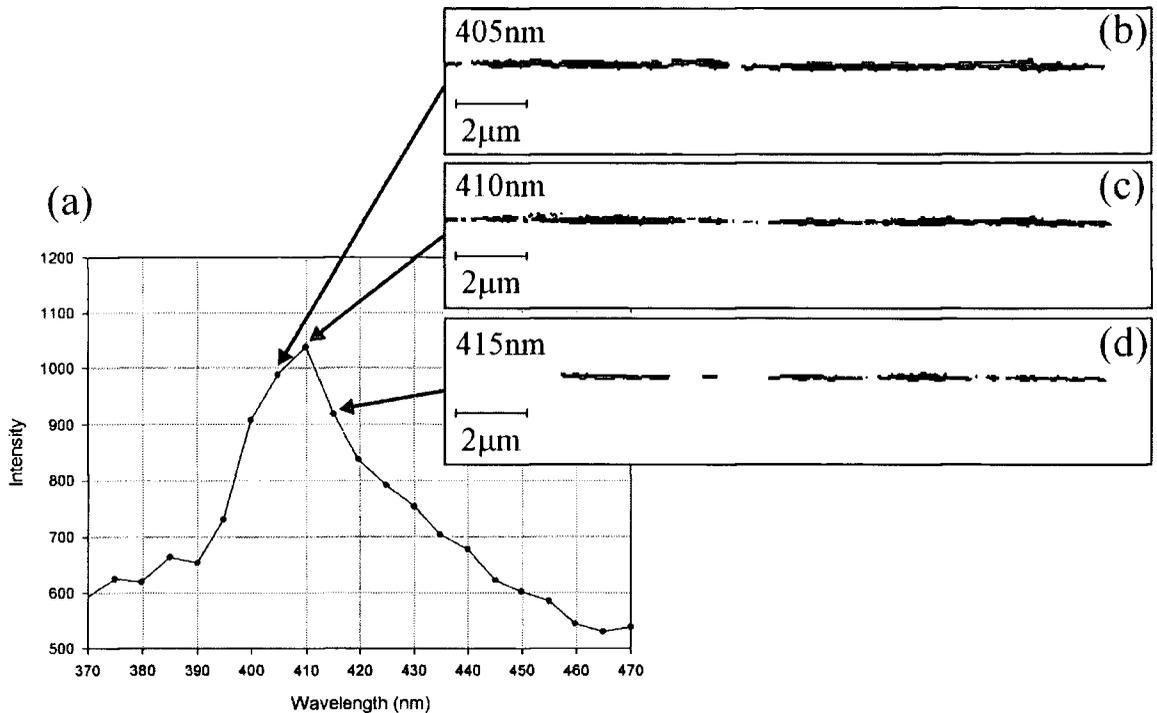
Figure 7.7: **STEM-CL spectrum taken from an area centred on an $In_{0.1}Ga_{0.9}N$ SQW. Monochromatic images of the same area are shown in b, c, and d. The image contrast has been inverted from the conventional sense for ease of viewing (black = CL intensity) and the images have been thresholded for clarity.**

Monochromatic images were recorded with the spectrometer centred on the peak QW emission wavelength of 410nm as shown in Figure 7.7(c). Images taken with centre wavelengths of 405 and 415nm are also shown. Attempts to record images with the spectrometer centred at ±10nm from the peak QW emission (QW_λ) were unsuccessful due to lack of signal. The images shown in Figure 7.7 have been processed to remove noise, and the gain and contrast have been adjusted equally for each image. Intensity line-scans along the images are shown in Figure 7.8. Inspection of the micrographs in Figure 7.7 and the line-scans in Figure 7.8 highlights some regions where there is strong CL emission at all three wavelengths. The line scans taken at 405nm and 410nm have similar intensity, and while they have the same general shape there are slight differences between them. That taken at 415nm shows reduced intensity and further shape differences.
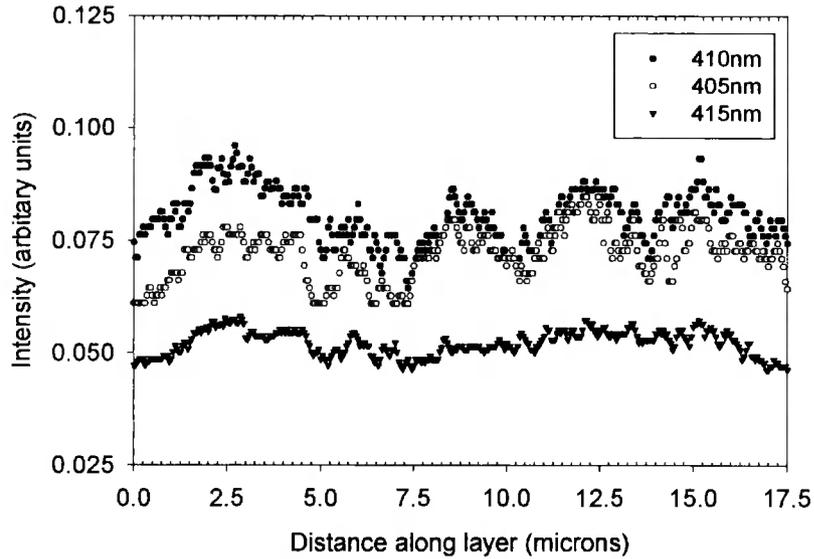
Figure 7.8: **Intensity profiles along the monochromatic CL images of the QW shown in Figure 7.7 recorded at 405nm, 410nm and 415nm.**

To aid the interpretation of these results it is necessary briefly to discuss the effects that the resolution of the spectrometer had on the observations.
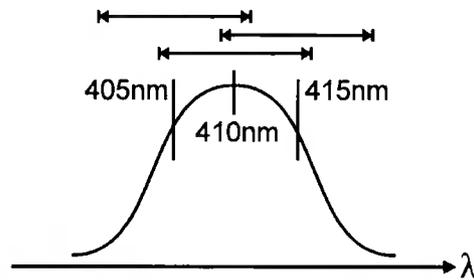
Figure 7.9: **Diagram showing the transmission range of the spectrometer with the different centre wavelengths selected for the images in Figure 7.7, QW_λ=410nm.**

As can be seen in Figure 7.9 all three monochromatic images in Figure 7.7 have a contribution from QW_λ. Hence only features common to all three monochromatic micrographs are unambiguously due to 410nm emission. The differences in fine detail in the intensity line scans may be attributed to localised QW luminescence at non peak wavelengths. Furthermore, since Figures 7.7(b) and 7.7(d) differ, the luminescent features responsible for CL at $QW_\lambda\pm5nm$ are distributed asymmetrically about the peak of the QW emission. Having identified an asymmetrical distribution of luminescence about the QW peak this

distribution will be further investigated by utilising monochromatic scans along the length of the QWs.

7.7.2 Monochromatic Line-Scans

It is possible to circumvent the software imposed maximum integration time of 0.01 seconds in STEM-CL imaging by using line-scans for which there is no preset limit on the integration time. In practice the risk of sample drift limits the length of time available for consecutive line scans to around 30 minutes. Allowing for six scans and 200 data points per scan results in an integration time of 1 second – two orders of magnitude above that available for monochromatic imaging. The downside of monochromatic line-scans is the problem of aligning the scan parallel to the QW. This was achieved by acquiring a panchromatic STEM-CL image of the area to be investigated and using the contrast from the QW to define the path of the line-scan. Calculations show that misalignment in the programmed path of the line-scan is likely to yield less than a 10nm variation in the relative position of the QW and the electron probe over a 2µm scan, i.e. less than the image width.

Figure 7.10 shows monochromatic line scans taken along the length of a QW with a spectral resolution of 10nm. The spectral *separation* of the line scans in Figure 7.10 has been increased from the 5nm used in Figure 7.7 to 10nm so that each scan is spectrally distinct from those adjacent. The line scan at 410nm is the most intense and exhibits fluctuations in intensity on a length scale of ~200nm. The peak to peak variation is a maximum of 110 counts which is well above a $\sqrt{N}$ counting error for the data. However, the line scan at 420nm exhibited a maximum peak to peak variation of 60 counts and the remaining scans had a typical peak to peak variation of 30 counts. These peak to peak variations are only slightly larger than the associated $\sqrt{N}$ counting errors on the data, suggesting that the features seen in the line scans at 400nm and 430nm may be attributable to statistical noise.
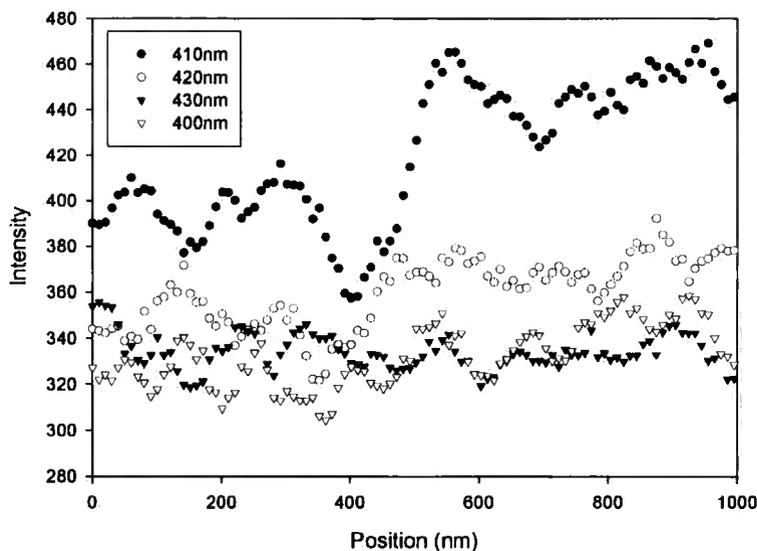
Figure 7.10: Monochromatic line scans taken along the length of an In₀.₁Ga₀.₉N SQW, QWλ=410nm.

Inspection of the line shapes in Figure 7.10 shows no consistent correlation or anti-correlation between the QW line-scan and the scans at ±10nm or between the scans at ±10nm themselves. This experiment was performed a number of times with a similar lack of correlation evident in each case. Attempts to investigate line-scans at wavelengths 5nm either side of the QW emission were unsuccessful as the further reduction in monochromator slit width necessary to work with a 5nm spectral resolution resulted in too great a drop in count rate. Factors which could account for the differences in localised luminescence observed will now be discussed.

7.7.3 Discussion

It is now discussed whether the results support any particular mechanism for non-uniform QW luminescence. Ternary composition and well thickness are considered separately.

To investigate the effect that fluctuation in the In content of the QW would have on emission wavelength, the data recorded by Martin et al [19] for CL peak energy E, in eV, versus In composition in $In_xGa_{1-x}N/GaN$ epilayers ($0<x<0.23$) was used:

$$E = [(3.398 \pm 0.006) - (3.91 \pm 0.05)x] \qquad (eV) \qquad (7.6)$$

106

Equation 7.6 gives the CL peak energy for $In_xGa_{1-x}N$ epilayers, however for QWs the peak emission energy is also a function of well thickness. Despite this Equation 7.6 can be used to give the relative shift in emission resulting from a variation, δx, in In content in a well of fixed width. Hence it may be calculated that a decrease in the QW emission wavelength of 5nm would result from a variation in In content of $\delta x = 0.01$ or approximately 10% for the samples investigated.

Considering well thickness, data presented for $In_{0.1}Ga_{0.9}N$ SQWs by Chichibu et al [20] shows a linear change of PL peak energy with QW thickness over the range 2.9eV (428nm) to 3.1eV (400nm). The gradient of this is 0.05eV/nm. This demonstrates that a change in QW thickness of 0.75nm would be required to account for a 5nm shift in the peak QW emission from 410nm. There is no evidence that QW thickness fluctuations of this size exist in these specimens. However, the uniformity of PL peak wavelength from the wafers investigated is reported to be high indicating good QW integrity, but this could be explained by compensatory changes to both the well thickness and indium mole fraction. Quantum confinement in the direction of the electron beam is judged to be unlikely.
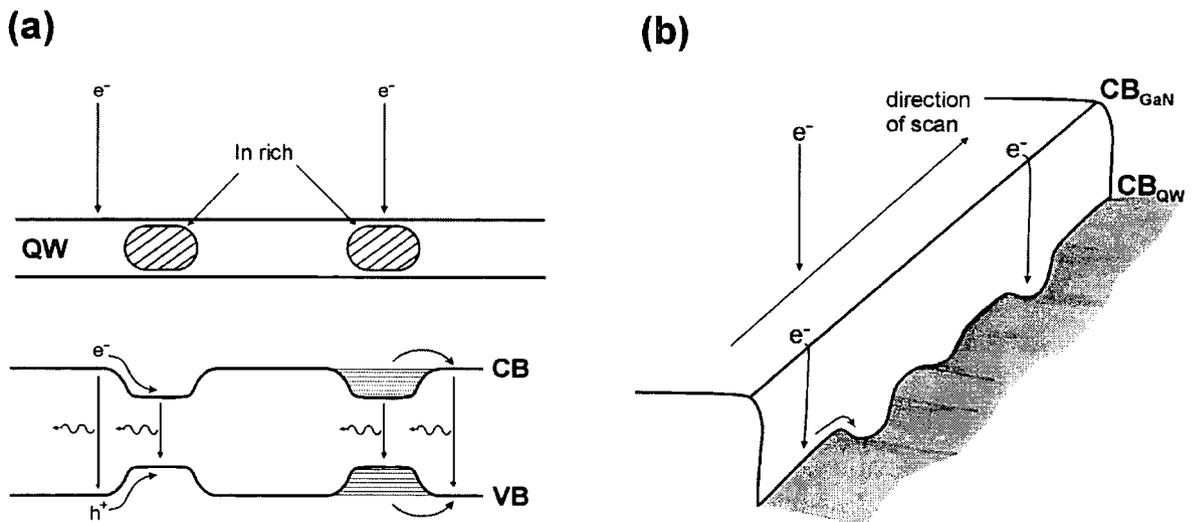

Figure 7.11: **Mechanisms for radiative transitions in an In rich region with (a) an electron beam scanning along a QW, and (b) an electron beam scanning parallel to a QW.**

Figure 7.11(a) shows possible recombination paths for a scenario where the QW contains In rich regions and the electron beam scans across such a region. As the electron beam approaches the In rich region it is able to capture some of the carriers, thereby causing emission at two principal wavelengths. If the electron beam directly excites the In rich region it would be necessary for all the states within the deeper well to be filled before carriers could 'spill over' into the rest of the QW. It should also be considered what would happen if the beam were not exactly aligned with the QW. Figure 7.11(b) shows a representation of the effect of the electron beam travelling parallel to the QW, but generating carriers in the barrier (GaN) which then diffuse towards the QW. If these carriers fall into the QW they may behave in a similar manner to that described in Figure 11(a). If radiative recombination were indeed described by this model then we would expect to observe emission at both QW_λ and at wavelengths of lower energy when the electron beam was near to an In rich region. When an In rich region was directly excited we would expect to see strong emission at wavelengths of lower energy than QW_λ with a smaller level of emission from QW_λ.

Inspection of Figures 7.8 and 7.10 reveals no systematic evidence of this type of behaviour. Low CL intensity and the necessity to disperse spectrally what signal there is results in a poor signal to noise ratio yields which make interpretation of the data difficult. However, the evidence would appear to support the conclusion that there is little evidence of regions of higher than average In content along the length of the QW. Fluctuations on a length scale of less than the 10nm probe size would not be detected in the STEM-CL apparatus used.

7.8 Conclusions

In this chapter a model was developed to predict the expected CL intensity from a region of particular thickness thus allowing CL images taken from electron-transparent wedge specimens to be corrected for thickness contrast artefacts. The foil thickness was estimated using the dynamical formulation of the relationship between the thickness and the transmitted electron intensity. For a given thickness the CL intensity was calculated using the Everhart-Hoff depth-dose function and also taking into account surface recombination losses.

Experimental CL images were normalised by dividing by the calculated CL value at each point.

Application of this normalisation method to GaN buffer layers with $In_{0.1}Ga_{0.9}N$ quantum wells revealed discontinuous luminescence characterised by bright regions on the scale of ~0.7μm. It is suggested that these regions of bright CL contrast are the result of 'hot spots' in the material which have been isolated in the TEM foil, rather than being a uniform property of the quantum wells.

Monochromatic imaging and line scans were utilised to investigate the localised spectral properties of these hot spots. Low CL intensity made measuring CL emission within narrow wavelength bands subject to significant counting errors. No statistically significant contrast in CL was observed with a wavelength greater than 10nm above or below the peak of QW emission, QW_λ. Regions with high CL intensity at QW_λ also exhibited high CL intensity at QW_λ ±10nm. A variation in QW emission of this magnitude may be accounted for by a variation of ±0.02 in the In mole fraction or a change in the QW width of ±1.5nm. However, variation in In mole fraction or QW width does not necessarily explain the variation in CL intensity along the QW on the length scale of ~200nm seen in monochromatic line-scans, or of ~0.7μm seen in monochromatic imaging. If the cause of the bright luminescence in these 200-700nm wide 'hot spots' were In clusters forming traps then an increase in luminescence at lower energy at the expense of emission at QW_λ may be expected. No evidence of this was found. In the next Chapter the effects of threading dislocations on the non-uniformity of QW CL is investigated.

7.9 References

1. Martin, R.W., P.R. Edwards, R. Pecharroman-Gallego, C. Liu, C.J. Deatcher, I.M. Watson, and K.P. O'Donnell, *Light Emission Ranging From Blue to Red From a Series of InGaN/GaN Single Quantum Wells*, Journal of Physics D: Applied Physics **35** (2002) 604-608.

2. Kawakami, Y., Y. Narukawa, K. Sawada, S. Saijyo, S. Fujita, S. Fujita, and S. Nakamura, *Recombination Dynamics of Localized Excitons in Self-Formed InGaN Quantum Dots*, Materials Science & Engineering B **50** (1997) 256-263.

3. O'Donnell, K.P., J.F.W. Mosselmans, R.W. Martin, S. Pereira, and M.E. White, *Structural Analysis of InGaN Epilayers*, Journal of Physics: Condensed Matter **13** (2001) 6977-6991.

4. Albrecht, M., V. Grillo, J. Borysiuk, T. Remmele, H.P. Strunk, T. Walther, W. Mader, P. Prystawko, M. Leszczynski, I. Grzegory, and S. Porowski, *Correlating Compositional, Structural and Optical Properties of InGaN Quantum Wells by Transmission Electron Microscopy*, Institute of Physics Conference Series **169** (2001) 267-272.

5. Hirsch, P.B., A. Howie, R.B. Nicholson, D.W. Pashley, and M.J. Whelan, *Electron Microscopy of Thin Crystals*, (Spottiswoode, Ballantyne & Co. Ltd., London and Colchester, 1965).

6. Reimer, L., *Transmission Electron Microscopy, Physics of Image Formation and Microanalysis*, (Springer-Verlag, Heidelberg, 1984).

7. Yacobi, B.G. and D.B. Holt, *Cathodoluminescence Microscopy of Inorganic Solids*, (Plenum Press, New York, 1990).

8. Roosbroeck, W.V., *Injected Current Carrier Transport in a Semi-Infinite Semiconductor and the Determination of Lifetimes and Surface Recombination Velocities*, Journal of Applied Physics **26** (1955) 380-391.

9. Everhart, T.E. and P.H. Hoff, *Determination of Kilovolt Electron Energy Dissipation vs Penetration Distance in Solid Materials*, Journal of Applied Physics **42** (1971) 5837-5846.

10. Kanaya, K. and S. Okayama, *Penetration and Energy-Loss Theory of Electrons in Solid Targets*, Journal of Physics D: Applied Physics **5** (1972) 43-58.

11. Gonzalez, J.C., K.L. Bunker, and P.E. Russell, *Minority-Carrier Diffusion Length in a GaN-Based Light-Emitting Diode*, Applied Physics Letters **79** (2001) 1567-1569.

12.   Rosner, S.J., E.C. Carr, M.J. Ludowise, G. Girolami, and H.I. Erikson, *Correlation of Cathodoluminescence Inhomogeneity With Microstructural Defects in Epitaxial GaN Grown by Metalorganic Chemical-Vapor Deposition.*, Applied Physics Letters **70** (1997) 420-422.

13.   Sugahara, T., H. Sato, M. Hao, Y. Naoi, S. Kurai, S. Tottori, K. Yamashita, K. Nishino, L.T. Romano, and S. Sakai, *Direct Evidence that Dislocations are Non-Radiative Recombination Centers in GaN*, Japanese Journal of Applied Physics **37** (1998) L398-L400.

14.   Zhang, X., P. Kung, D. Walker, J. Piotrowski, A. Rogalski, A. Saxler, and M. Razeghi, *Photovoltaic Effects in GaN Structures With p-n Junctions*, Applied Physics Letters **67** (1995) 2028-2030.

15.   Chernyak, L., A. Osinsky, H. Temkin, J.W. Yang, Q. Chen, and M.A. Khan, *Electron Beam Induced Current Measurements of Minority Carrier Diffusion Length in Gallium Nitride*, Applied Physics Letters **69** (1996) 2531-2533.

16.   Bandic, Z.Z., P.M. Bridger, E.C. Piquette, and T.C. McGill, *Minority Carrier Diffusion Length and Lifetime in GaN*, Applied Physics Letters **72** (1998) 3166-3168.

17.   Bridger, P.M., Z.Z. Bandic, E.C. Piquette, and T.C. McGill, *Correlation Between the Surface Defect Distribution and Minority Carrier Transport Properties in GaN*, Applied Physics Letters **73** (1998) 3438-3440.

18.   Chernyak, L., A. Osinsky, G. Nootz, A. Schulte, J. Jasinski, M. Benamara, Z. Liliental-Weber, D.C. Look, and R.J. Molnar, *Electron Beam and Optical Depth Profiling of Quasibulk GaN*, Applied Physics Letters **77** (2000) 2695-2697.

19.   Martin, R.W., P.R. Edwards, K.P. O'Donnell, E.G. Mackay, and I.M. Watson, *Microcomposition and Luminescence of InGaN Emitters*, Physica Status Solidi A **192** (2002) 117-123.

20.   Chichibu, S.F., A.C. Abare, M.P. Mack, M.S. Minsky, T. Deguchi, D. Cohen, P. Kozodoy, S.B. Fleischer, S. Keller, J.S. Speck, J.E. Bowers, E. Hu, U.K. Mishra, L.A. Coldren, S.P. DenBaars, K. Wada, T. Sota, and S. Nakamura, *Optical Properties of InGaN Quantum Wells*, Materials Science & Engineering B **59** (1999) 298-306.

Extended Defects In Gallium Nitride

8.1 Introduction

The aims of this chapter are to use TEM-CL to investigate the effect of extended defects on the luminescent properties of $In_xGa_{1-x}N$ QWs and GaN epitaxial layers. Statistical analysis methods are used to investigate the distribution of extended defects in GaN epilayers. $In_xGa_{1-x}N$/GaN QW structures grown in the conventional [0001] (c-plane) direction, and GaN epitaxial layers grown in the more unusual [1-100] (M-plane) direction are investigated. M-plane GaN epilayers are of interest since this orientation is non-polar and offers the possibility of growing QWs free from the spontaneous polarization that is present in c-plane GaN [1].

In the first part of this chapter STEM-CL images of $In_xGa_{1-x}N$/GaN SQWs are correlated with diffraction contrast TEM imaging to investigate the effects of threading dislocations on the non-uniformity of QW CL emission seen in Chapter 7. The spatial statistical distribution of threading dislocations observed in a TEM foil is analysed in one dimension (1D) and the relationship between threading dislocations and the so-called V-defect or V-pit is discussed. A two dimensional

(2D) statistical analysis of V-pit distributions in $In_xGa_{1-x}N$/GaN MQWs is then presented.

In the second part luminescence associated with basal plane stacking faults in M-plane GaN grown on γ-LiAlO$_2$ is investigated using TEM-CL spectroscopy and line-scans.

8.2 Statistical Methods Used in this Chapter

8.2.1 Analysis of Dislocation Distributions in 1D

A number of statistical methods have been reported for the analysis of one dimensional distributions [2]. However these are not necessarily directly applicable to the task of analysing the occurrence of threading dislocations in a TEM foil. This is because TEM foils are typically wedge shaped, so that there is greater probability of seeing a threading dislocation in projection in a thicker section of the wedge than a thinner section. This complicates the analysis as the occurrence of a threading dislocation in the thinnest section of the wedge should be statistically more heavily weighted than a dislocation in the thicker section. However, moving to thicker sections of the wedge brings problems of electron beam penetration and the risk of underestimating dislocation densities as some dislocations will be masked by others in the projection. With these problems in mind a weighted autocorrelation method has been created to assess whether there is any correlation between the threading dislocations observed. The analysis method has been coded in *FORTRAN* and is listed in Appendix A4. The data preparation necessary and subsequent analysis performed by the 1D autocorrelation statistical analysis tool is listed below:

1. A montage of TEM diffraction contrast images moving along the length of the epitaxial layer was produced.
2. The position of each dislocation was recorded together with the approximate thickness of the layer at each position estimated from thickness fringes.
3. The dislocation distribution was mapped on to a line of unit length.
4. The thickness value associated with each dislocation was normalised so that the dislocation in the thinnest section of foil

had an associated value of 1 and the dislocation in the thickest an associated value of x_{max}, where x_{max} is the relative increase in thickness between the two dislocations.

5. The thickness values associated with each dislocation were then inverted and multiplied by x_{max}. The dislocation in the thinnest section of the foil now has an associated thickness of x_{max}, and the dislocation in the thickest section has an associated thickness of 1. (This is the data format for the code listed in Appendix A4.)

6. The unit length was then divided up into a number of bins, in effect the resolution of the analysis.

7. The distance between each dislocation and every other dislocation, and also the product of the thickness values associated with each dislocation correlation was calculated. This product was added to the appropriate bin for the correlation distance. The whole process was repeated for every dislocation in the distribution.

8. The data held within the bins was normalised by dividing by a distribution calculated using a large number of randomly generated data points.

9. The normalised 1D autocorrelation function was plotted as a histogram.

A random distribution of dislocations would yield an autocorrelation function with a value of unity at all separations. Whilst a peak at a certain separation would indicate a tendency for the dislocations to be separated by that distance, ie ordering of some form.
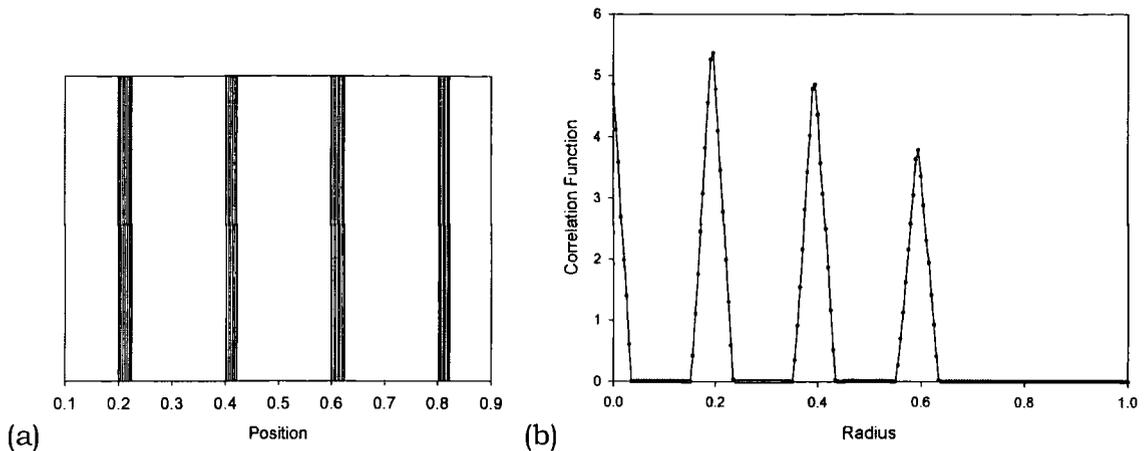
Figure 8.1: **Synthetic 1-D array of clusters on a normalised field (a), 1D correlation function analysis for the clustered data (b).**

Figure 8.1 shows the application of the 1D autocorrelation function to synthetic clustered data. Spacing within each cluster is 0.001. A peak at a radius spacing of 0 is representative of the intra-cluster distances. The peaks at 0.2, 0.4 and 0.6 are due to the separation of the clusters, whilst anti-clustering is represented by minima in the correlation function. The width of the peaks is a function of the width of the clusters themselves.

8.2.2 Analysis of Dislocation Distributions in 2D

In this work four methods of analysing 2D distributions quantitatively have been used. These methods have been successfully applied to the analysis of dislocation distributions in II-VI compounds previously [2-5]. The four tests are a nearest neighbour analysis, comparison with a Poisson distribution, radial autocorrelation function, and spatial autocorrelation function. All four tests were performed using *FORTRAN* routines these being listed in Appendix A.

Nearest neighbour analysis. This test assesses the extent to which a distribution is clustered or ordered through the distribution parameter R_n,

$$R_n = 2d \sqrt{\frac{n}{A}} \qquad (8.1)$$

where d is the mean distance between nearest neighbours, n is the number of points in the study area of size A [6]. A R_n value of unity indicates

randomness, $R_n<1$ clustering, and $R_n>1$ ordering. For a distribution containing a minimum of 500 points the effective thresholds for clustering and ordering are 0.85 and 1.15 respectively [6]. Synthetic distributions of clustered, random and ordered data are show in Figure 8.2 together with R_n values.

(a)　　　　　　　　　　　　(b)

(c)　　　　　　　　　　　　(d)
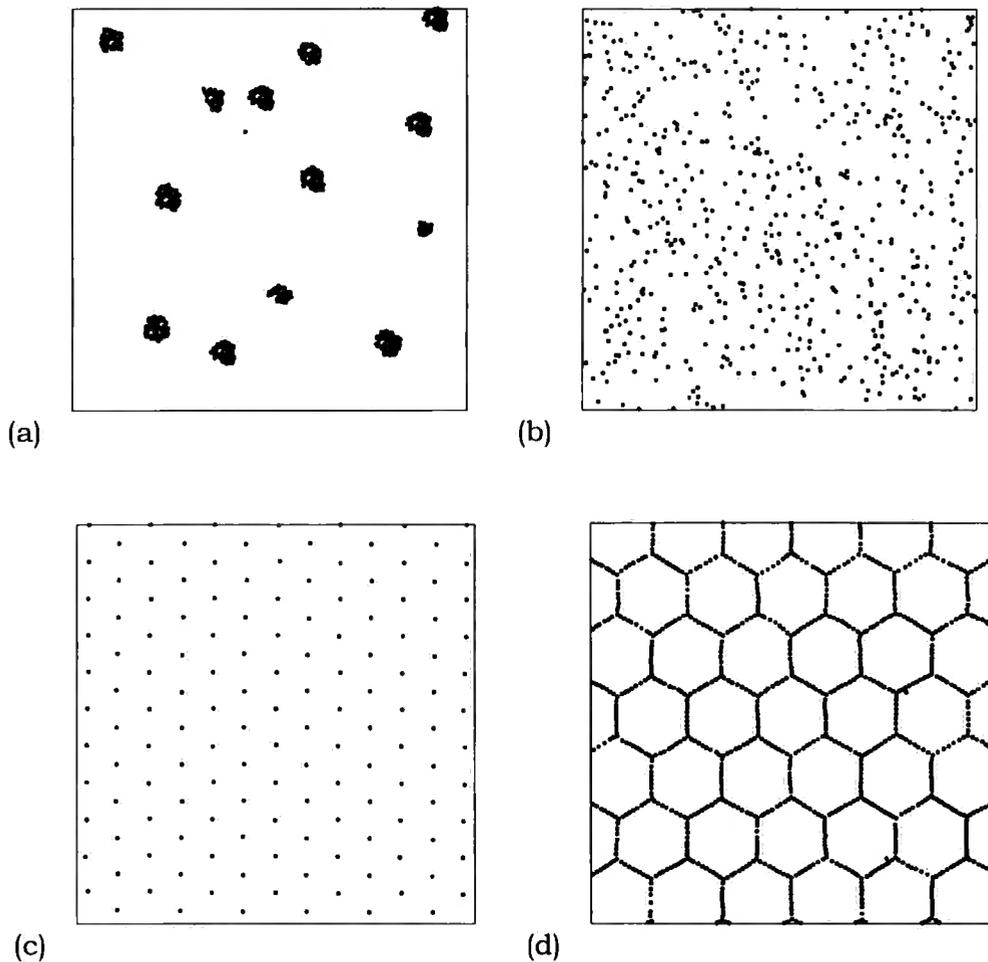
Figure 8.2: **Synthetic point distributions. R_n values for the clustered (a), random (b), hexagonal ordered (c), and honeycomb ordered (d) distributions are 0.22, 0.99, 2.13, and 0.62 respectively.**

Comparison to a Poisson distribution: By mapping a point distribution onto a grid made up of sections of equal area a frequency histogram of the occupancy of each section can be constructed. If the original distribution is random this histogram will tend to a Poisson distribution. Comparison of experimental data to a Poisson distribution allows the degree of randomness to be

evaluated. If the mean number of points expected to occur in an interval is λ, then the probability, *P(r)*, that an integer number of points, *r*, occur in that interval is given by,

$$P(r)=\exp(-\lambda)\frac{\lambda^r}{r!}$$

(8.2)

A chi-squared test is used to compare the observed distribution with a Poisson distribution using the null hypothesis that the real and Poissonian data belong to the same distribution.

Radial Autocorrelation Function. This function assesses radial correlations between points in a data set. The radial distribution is calculated by taking each point in turn and using it as a centre point for generating a radial density distribution and normalising by dividing by a curve generated for random data. The frequencies at each radial distance for random data are plotted on a histogram as shown in Figure 8.3(a). Randomly distributed data will give a radial distribution function of unity at all radii. This can be seen in Figure 8.3(b) where the radial correlation function is distributed closely around unity at radii values up to 1. At radii above 1 the radial correlation function deviates from unity. This is due to a smaller number of data points in the corners of the square which can participate in long range radial correlations. Peaks in the histogram indicate enhanced clustering at specific radii. This is demonstrated in Figure 8.3(c) where a random point distribution has been overlaid with clustered data. This clustering is manifested in a short range intercluster correlation at low radius and longer range intracluster correlations. A number of features can be seen in the autocorrelation function (Figure 8.3(d)) for the honeycomb distribution shown in Figure 8.2(d). The peak at low radius (<0.1) is due to short range intercluster correlations. The longer range correlations with periodicity of approximately 0.16 are due to correlations between the hexagonal planes in the honeycomb distribution
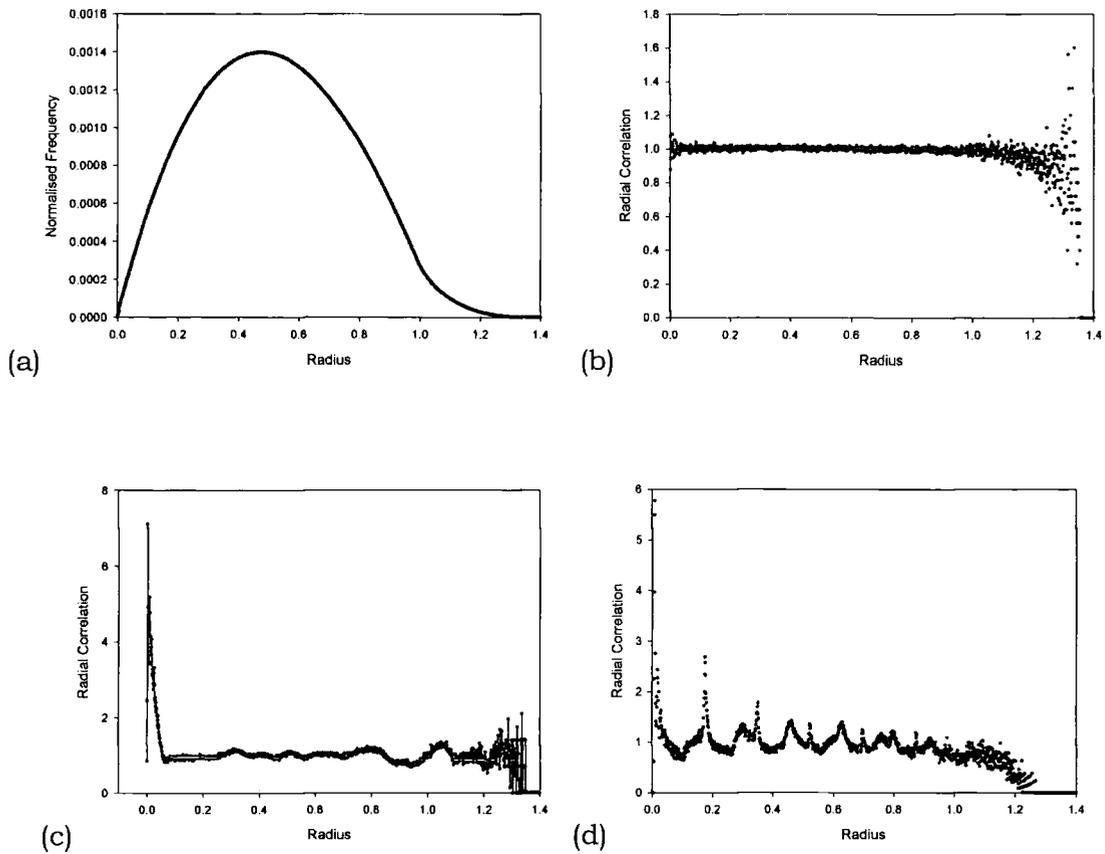
Figure 8.3: **(a) Radial correlation frequencies generated using 100,000 data points, (b) radial correlation function for a random distribution of 5000 points, (c) radial correlation function for a random distribution overlaid with a second distribution containing clusters of points, and (d) radial correlation function for the honeycomb structure shown in Figure 8.2(d).**

Spatial Distribution Function. The spatial distribution function is used to study any spatial and directional relationship in a set of data points. As in all the other statistical tests used the data is initially mapped onto a unit grid. The distribution is calculated by taking each point in turn and subtracting its x,y coordinates from those of each and every other point in the distribution. Thus each point will yield n-1 translational vectors, where n is the number of points in the distribution. Therefore the total number of translational vectors will be $n(n$-1). The unit square is divided up into a number of bins; a count is recorded in each bin for every translational vector that falls within the boundaries of that bin. This spatial distribution function is normalised by dividing by a function generated using random point positions and displayed as a contour map with x,y axes and greyscale colouring representing intensity. Due to excessively long

calculation times using this method the spatial distribution has only been calculated for resultant vectors falling in the positive quadrant.

(a)　　　　　　　　　　　　　　(b)
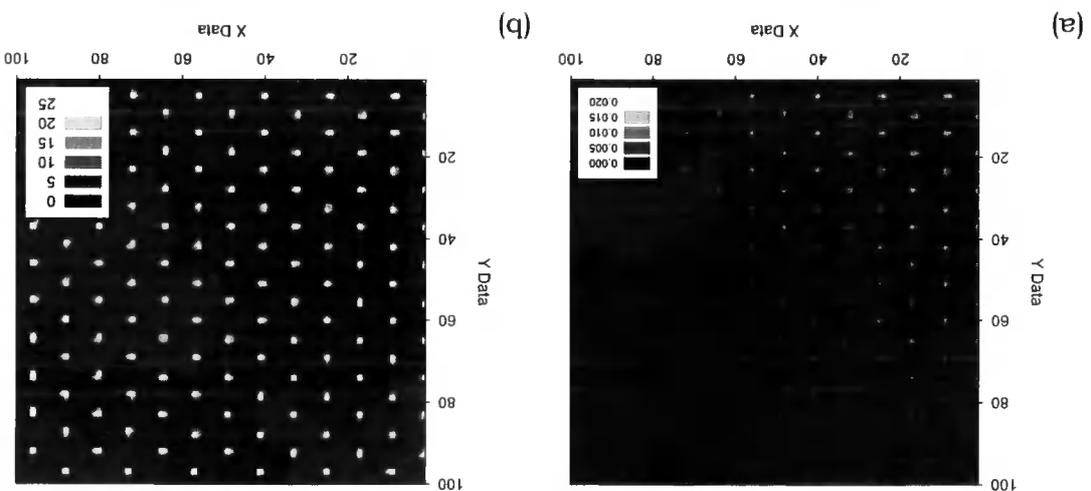
Figure 8.4:　Spatial distribution function calculated from a hexagonal matrix of points, (a) unnormalised, (b) normalised by dividing by the function for a random distribution.

Figure 8.4 demonstrates the effectiveness of the spatial distribution function at highlighting directional relationships in a set of points and the necessity of normalising the distribution function. Both Figure 8.4(a) and (b) were calculated from an identical hexagonal distribution of points. In Figure 8.4(a) the short range correlation between points in the grid is strong; however the longer range correlations are weaker as the number of correlations at larger separations are less frequent. Dividing the distribution in Figure 8.4(a) by a distribution created from a large number of random data points highlights all spatial correlations which would not be expected from a random distribution. This can be seen in Figure 8.4(b).

8.3 Samples Used in this Chapter

The samples investigated in this chapter are listed in Table 8.1 below.

Sample	Epilayer structure	Substrate	Growth Method	Summary Growth Details
M-plane GaN epilayer	500nm epilayer	γ-LiAlO$_2$ (100)	PAMBE (Paul-Drude Institute, Berlin)	750°C substrate temperature, constant nitrogen flux [7, 8]
In$_{0.1}$Ga$_{0.9}$N SQW	1μm GaN buffer layer, 2.5nm In$_x$Ga$_{1-x}$N QW, 15nm GaN capping layer. (x=0.101±0.015) [9]	c-plane sapphire	MOVPE (Institute of Photonics, University of Strathclyde)	20nm GaN nucleation layer at 540°C, GaN buffer layer at 1140°C, In$_x$Ga$_{1-x}$N QW grown at 832°C [10, 11]
STR94	1μm GaN buffer layer, 10 period MQW In$_x$Ga$_{1-x}$N 9.4nm superlattice period, 15nm GaN capping layer. (x=0.101±0.015)	c-plane sapphire	MOVPE (Institute of Photonics, University of Strathclyde)	MQW growth temperature 832°C, GaN buffer layer grown at 1170°C [10]
STR204	1μm GaN buffer layer, 10 period MQW In$_x$Ga$_{1-x}$N 10.0nm superlattice period, 15nm GaN capping layer. (x=0.1)	c-plane sapphire	MOVPE (Institute of Photonics, University of Strathclyde)	MQW growth temperature 860°C, GaN buffer layer grown at 1170°C [10]
STR241	1μm GaN buffer layer, 14 period MQW In$_x$Ga$_{1-x}$N, 2.4nm well thickness, 7.3nm barrier thickness , 15nm GaN capping layer. (x=0.091)	c-plane sapphire	MOVPE (Institute of Photonics, University of Strathclyde)	As STR 204

Table 8.1:   Specimen structure and growth details.

8.4 c-plane GaN

8.4.1 Threading Dislocations in c-plane GaN

Wurtzite GaN grown on the basal plane of sapphire is characterised by a large density of threading dislocations of the order of $10^{10}cm^{-2}$. Edge, screw and mixed character threading dislocations have been identified in GaN epitaxial layers, with edge dislocations being the dominant type [12]. The edge dislocations are characterised with Burgers vectors, **b**=1/3<2-1-10>, with the line direction perpendicular to the Burgers vector in the [0001] direction. Pure screw dislocations are characterised by a line direction and Burgers vector along the [0001] direction, whilst mixed dislocation have Burgers vectors given by **b**=1/3<11-23>.

The origin of these dislocations may be better understood by considering the nucleation layer method used for epitaxial GaN growth. The use of a GaN buffer layer grown at low temperature (~500°C) was demonstrated by Nakamura as a technique for improving the quality of GaN films [13], and is routinely used in the growth of GaN epitaxial layers [14]. The nucleation layer is composed of cubic, hexagonal and amorphous GaN [15, 16]. Akasaki et al [17] proposed a nucleation mechanism whereby the nucleation layer crystallizes into columnar crystals during annealing at ~1000°C. When GaN growth was then resumed at the higher temperature GaN islands formed on top of the crystals in the buffer layer. These islands would laterally overgrow the nucleation layer forming regions of high quality GaN of size 50nm to 1μm. Differences in orientation of these islands as they coalesced would generate threading dislocations. This is shown in Figure 8.5(a) where rotation about the [0001] direction results in tilt boundaries and (b) where rotation about [*uvt*0] results in twist boundaries [18].
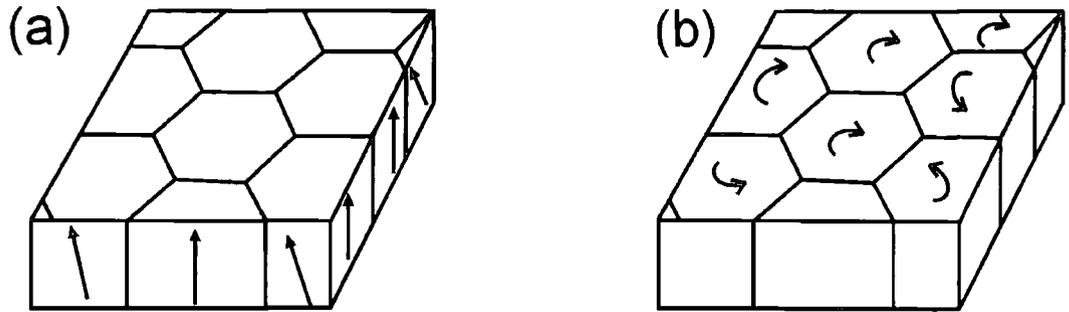
Figure 8.5: **GaN columnar structure model based upon island growth on a low temperature nucleation layer. Variations in the orientation of the crystals can occur due to (a) tilt and (b) twist.**

GaN based light emitting structures have been shown to have quantum efficiencies as high as 4% despite dislocation densities of the order of 10^{10}cm^{-2} [19, 20]. Evidence demonstrating that dislocations act as nonradiative recombination centres [21-25] shows that an understanding of the formation mechanism of dislocations and their role as nonradiative recombination centres is important for the development of higher power GaN based devices and laser diodes. TEM-CL measurements performed by Albrecht *et al* [25] showed that dislocations (**b**=1/3<11-20>) introduced into GaN single crystals by indentation act as nonradiative recombination centres. Cherns *et al* [24] showed that reduced CL from an In$_x$Ga$_{1-x}$N SQW was correlated to regions associated with threading edge dislocations.

V-shaped surface pits were identified in GaN [21] and In$_x$Ga$_{1-x}$N/GaN QW structures [23, 24] and shown to be directly correlated to regions of low CL contrast. The surface pits were shown to be associated with screw and mixed dislocations. However, the dark CL contrast observed from the pits in the In$_x$Ga$_{1-x}$N QW structure [23] could be attributed to the absence of the QW from the pit facets rather than from the dislocation at the base of the pit. TEM images of V-pits observed in an In$_x$Ga$_{1-x}$N MQW sample are shown in Figure 8.6.
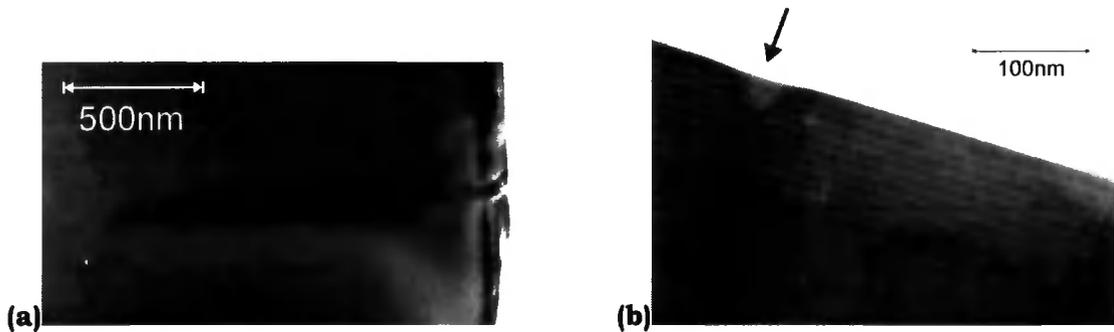
Figure 8.6: Cross-sectional TEM micrographs of c-plane InGaN/GaN MQW structure, (a) a threading dislocation can be seen crossing the MQW, g=[0002], (b) MQWs in cross section. V-shaped region indicated may be due to the partial intersection of a V-pit, g=[0002].

The V-pit is routinely observed in $In_xGa_{1-x}N$/GaN QW structures and is also known as an inverted hexagonal pyramid or hexagonal pinhole [26]. Figure 8.7 shows the structure of the V-pits with a hexahedron cone with the six sidewalls on <1-101> planes and a dislocation connected to the vertex of the cone. In cross-section this structure appears as an open 'V' shape.
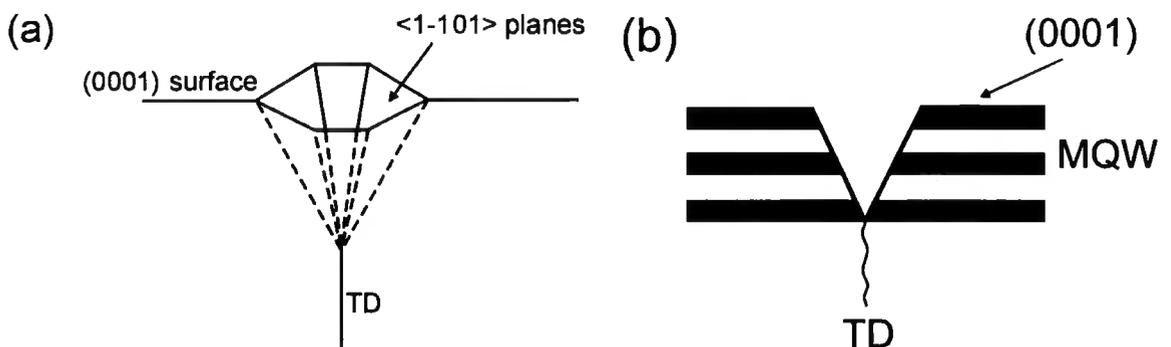
Figure 8.7: Diagramatic representation of the V-pit formed from a dislocation terminating at a hexahedron cone in the (0001) surface, (b) cross-sectional view of a V-pit forming at an InGaN/GaN interface.

Chen *et al* [27] report that in MOVPE grown material the V-pit can be associated with threading dislocations of screw, edge and mixed character. A similar finding is reported with an increased nucleation probability at mixed dislocations in comparison with pure edge dislocations [28]. The open surface (0001) width of the V-pit increases with the depth of the pit. For example, the average size of pit was reported to increase from ~10nm on the surface of a three QW sample to ~25nm on the surface of five QWs [27]. Northrup and Neugebauer [26] propose that In acts as a differential surfactant, reducing the energy of the

(10-11) surface relative to the (0001) surface, thus promoting the formation of (10-11) faceted dislocation pits on the (0001) surface. Alternative methods of V-pit formation include those by Liliental-Weber *et al* [29] who propose that the pits are initiated by an impurity complex such as oxygen and silicon or more recently by Miraglia *et al* [30] who propose that pitting is caused by dislocations interfering with step flow, particularly at low temperatures.

8.4.2 Effect of Threading Dislocations on QW Luminescence

The effect of the threading dislocations on the CL from the $In_{0.1}Ga_{0.9}N$ SQW described in Table 8.1 has been investigated by recording a panchromatic STEM-CL image from a cross-sectional TEM foil and then creating a montage of CTEM images along the epitaxial layer. The position of all dislocations passing through the QW was noted and these were aligned with a CL intensity line scan taken along the length of the STEM-CL image. This can be seen in Figure 8.8 where (a) and (b) are bright field (**B**=[11-20]) TEM images, (c) is a bright field (**B**=[11-20]) CTEM image montage, (d) is a panchromatic STEM-CL image, and (e) shows a CL intensity line scan along the length of the QW with the position of all dislocations crossing the QW marked.

In the CTEM montage in Figure 8.8(c) a bright region between the GaN epilayer and the sapphire substrate can be seen. This effect is thought to be due to preferential thinning of the low temperature GaN nucleation layer during Ar^+ milling. Thickness fringes can be seen in the thinner sections of the wedge (towards the left of the image). These have been used to estimate the relative thicknesses of different sections of the wedge for the analysis in Section 8.4.3.

The STEM-CL image seen in Figure 8.8(d) was recorded in panchromatic mode. The luminescence from the GaN epilayer increases uniformly in brightness from left to right as the thickness of the wedge increases. However, the luminescence from the QW varies in intensity in a non-uniform manner. The necessity of using the thinnest part of the foil for analysis meant that monochromatic imaging was not possible due to the weakness of the signal; this was discussed in greater detail in Section 7.7.1. The CL intensity line-scan was taken by selecting a long, thin section of Figure 8.8(d) containing the QW and vertically integrating the resultant bitmap. The overall shape of the line-scan (Figure 8.8e) is an increasing trend as the thickness of the foil increases. As

described in Section 7.4 the CL increases super-linearly with increasing thickness due to decreasing losses to surface recombination as a percentage of the total.
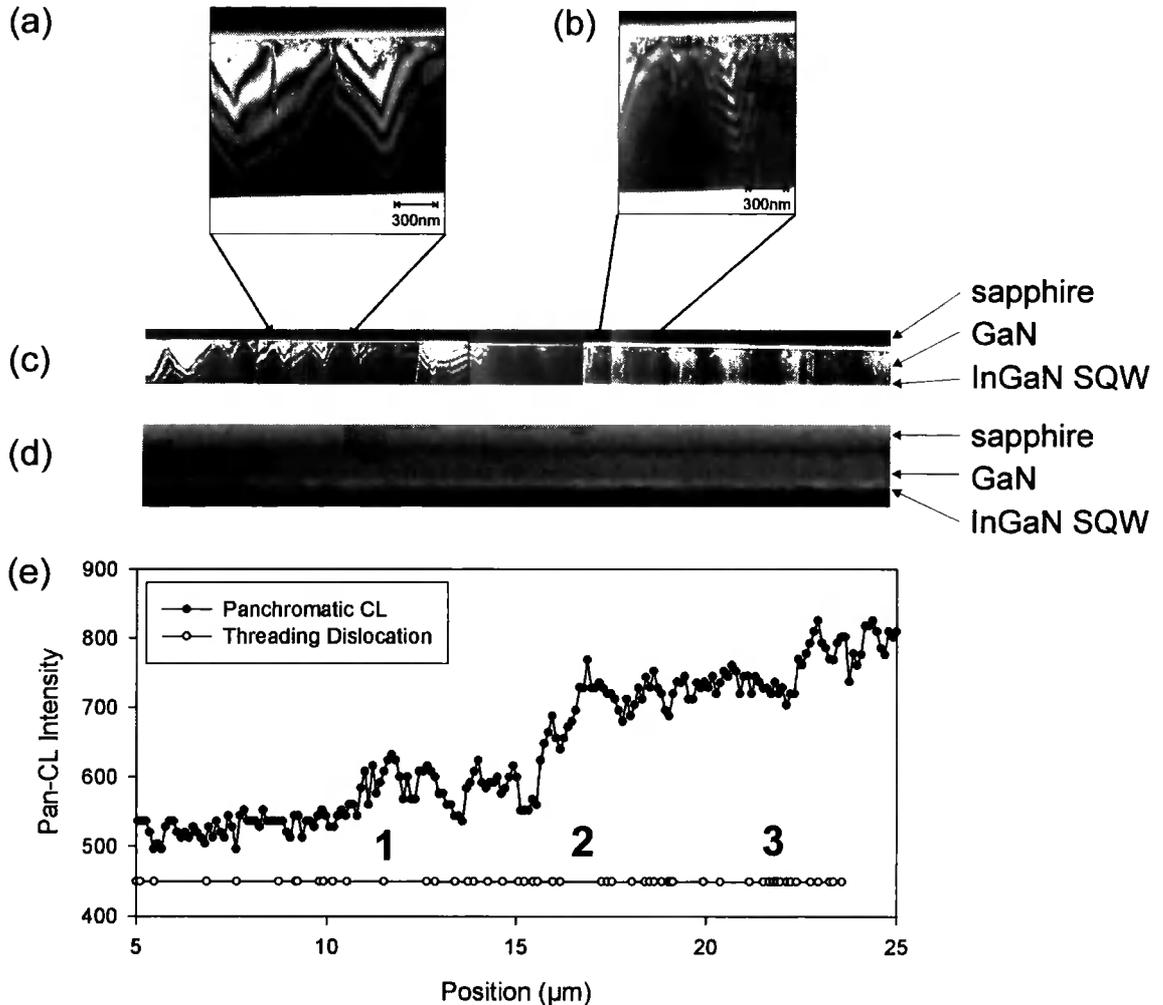
Figure 8.8: **(a), (b) Bright field (B=[11-20]) TEM images, (c) montage of TEM images, B=[11-20], (d) panchromatic STEM-CL image of the area in (c), (e) intensity line-scan of QW luminescence and dislocation positions.**

Three regions have been highlighted in Figure 8.8(e). Regions 1 and 2 contain only one or two dislocations within an approximately 1µm length of the QW. Inspection of the CL line-scan in these regions shows the CL reaches local maxima at these positions. Region 3 contains a high density of dislocations which appear marginally to suppress the associated CL. However with the increasing trend in CL intensity with distance along the layer in mind the suppression of the CL intensity is more marked than it appears. Dislocation

quenching of QW luminescence is consistent with reports [24, 25] that threading dislocations act as non-radiative recombination centres.

Inspection of the dislocation distribution shown in Figure 8.8(e) shows the dislocations to appear slightly clustered and anti-clustered on a length scale of approximately 2μm. To investigate this further a statistical analysis of the distribution in Figure 8.8(e) and those obtained from similar montages is now considered.

8.4.3 Analysis of Dislocation Distributions

Montages of diffraction contrast CTEM images running along the length of epitaxial GaN/In$_{0.1}$Ga$_{0.9}$N SQW foils were taken for two samples prepared from the same wafer. Unlike the analysis in Section 8.4.2 a dislocation was logged if it appeared anywhere in the epilayer's thickness, not just when it impinged on the QW. The dislocation distributions were analysed using the 1D autocorrelation function described in section 8.2.1 and are shown in Figure 8.9.
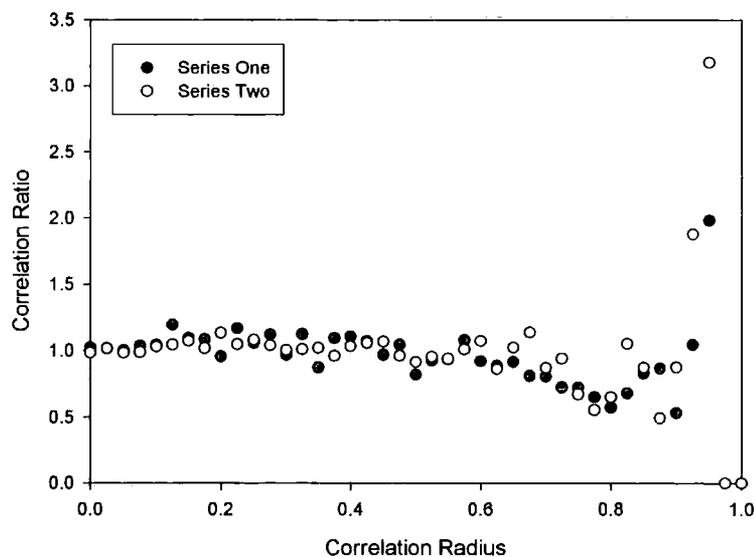
Figure 8.9: **Correlation function analysis of two linear dislocation distributions (series one and two) taken from In$_{0.1}$Ga$_{0.9}$N/GaN SQWs.**

The 1D autocorrelation functions are similar in shape showing small deviations about unity at radii up to 0.7. Beyond this they decline to around 0.5 at a radius of 0.8 and there is considerable scatter as they approach a radius of 1. This is thought to be due to there being a smaller number of data points

which are separated by the larger radii hence giving greater statistical noise; this is seen also in Figure 8.3(b). The decline at 0.8 indicates an anti-correlation at this radius which corresponds to a separation of 15µm. Physically this would indicate a smaller than expected number of dislocations separated by this distance. However, this finding should be viewed with caution as the number of data points analysed (series one, 82 points, and series two, 94 points) is very low. Ordinarily 500 points or more are recommended for the autocorrelation analysis. In this analysis, however, it is not possible to increase the number of data points as the data collection is limited by the penetration power of the TEM beam and difficulties in resolving individual dislocations in thicker sections of a TEM foil due to the projection of a large density of dislocations on to a plane.

8.4.4 Discussion

The 1D correlation function shown in Figure 8.9 shows there is no strong clustering of dislocations in the distributions analysed. This is in contradiction to other studies [18] where dislocation clusters with a separation of 0.3µm were observed and attributed to the misalignment of GaN crystallites at the nucleation layer/buffer layer interface. However, the small number of dislocations in the distributions analysed casts doubt on the statistical significance of the test. In the next section larger numbers of dislocations are investigated by extending the analysis to the surface of an $In_xGa_{1-x}N/GaN$ QW structure through the investigation of V-pits as secondary evidence for the presence of dislocations.

8.4.5 Analysis of V-Pit Distribution

AFM and SEM are effective, non destructive, tools for mapping the surface morphology of materials. As described in section 8.4.1 the structure of a V-pit is an open hexagonal cone with a threading dislocation at the vertex. Therefore by mapping the occurrence of V-pits it should be possible to investigate the correlations between threading dislocations on relatively large length scales. However, it is worth noting at this point that whilst V-pits have been shown to always have a threading dislocation at the vertex, all threading dislocations do not terminate in a V-pit [27].

Wafers of 10 and 14 period $In_xGa_{1-x}N$ MQWs (see Table 8.1 for growth details) were investigated using AFM and the 10 period MQW was also investigated using SEM. Previous studies of these samples have revealed surface pitting with a similar structure to V-pits [31]. The AFM mapping was performed by Chaowang Liu[1] using a *Digital Instruments Multimode Nanoscope IIIa* operating in tapping mode with an etched silicon tip. The SEM was performed using a *JEOL JSM-IC848* SEM in secondary electron mode using *GW Printerface* for image acquisition. The data was collected in the following manner:

1. Overlapping SEM images were taken with a magnification high enough to resolve individual surface pits.
2. The individual frames were used to create a montage of a large area of the surface.
3. The pit positions were marked on an overlaid acetate sheet.
4. The acetate was scanned as a 1-bit bitmap and the pit positions were logged using the *Visual Basic* routine given in Appendix A5.
5. The pit position pattern was broken down into a number of smaller regions containing 500-1000 pits.
6. Each region was mapped onto a unit grid for analysis using the statistical tests described in section 8.2.2.

Figures 8.10 to 8.13 show the results of the statistical tests for pit distributions taken using AFM from two 10 period MQW samples, using SEM from one of the 10 period MQW samples, and AFM from a 14 period MQW sample. For each sample the original AFM or SEM image is shown together with the pit distribution mapped on to a unit grid. The radial autocorrelation function, the spatial correlation function, and comparison to a Poisson distribution are shown together with summary statistics of the data.

---

[1] C.liu@strath.ac.uk, Institute of Photonics, 106 Wolfson Centre, 106 Rottenrow, Glasgow, G4 0NW

Figure 8.10: Summary of statistical tests applied to the 10 period $In_{0.1}Ga_{0.9}N/GaN$ MQW STR94. (a) AFM image courtesy of Chaowang Liu, *Institute of Photonics, University of Strathclyde*, (b) Point distribution mapped on to a unit square, (c) spatial correlation function, (d) radial correlation function, (e) comparison to Poisson distribution, (f) summary of numerical data.

STR204 - 10 period MQW grown at 860°C

(a) AFM Image

(b)

(c) Spatial Correlation Function

(d) Radial Correlation Function

(e) Comparison to Poisson Distribution

- Experimental Prob.
- Poisson Prob.

(f)

R_N	1.05862
Number of points	1296
Chi-squared total	0.373323165
DOF	19
Prob. Random	>99%
Unit square side	7619nm
Feature density	2.23E+09 cm^2

Figure 8.11: Summary of statistical tests applied to the 10 period $In_{0.1}Ga_{0.9}N/GaN$ MQW STR204. (a) AFM image courtesy of Chaowang Liu, *Institute of Photonics, University of Strathclyde*, (b) Point distribution mapped on to a unit square, (c) spatial correlation function, (d) radial correlation function, (e) comparison to Poisson distribution, (f) summary of numerical data.

STR204 - 10 period MQW grown at 860°C

(a) SEM Image

(b)

(c) Spatial Correlation Function

(d) Radial Correlation Function

(e) Comparison to Poisson Distribution

- Experimental Prob.
- Poisson Prob.

(f)

R_N	1.18528
Chi-squared total	0.171791017
DOF	12
Prob. Random	>99%
Number of points	474
Unit square side	4290nm
Pit density	$2.58E+09cm^2$

Figure 8.12:   Summary of statistical tests applied to the 10 period $In_{0.1}Ga_{0.9}N/GaN$ MQW STR204. (a) SEM image (b) Point distribution mapped on to a unit square, (c) spatial correlation function, (d) radial correlation function, (e) comparison to Poisson distribution, (f) summary of numerical data.

STR241 - 14 period MQW grown at 860°C

(a) AFM Image

(d) Radial Correlation Function

(b)

(e) Comparison to Poisson Distribution

(c) Spatial Correlation Function

(f)

R_N	1.08767
Number of points	1327
chi-squared total	0.327620515
DOF	18
Prob. Random	>99%
Unit square side	7404nm
Feature density	$2.42E+09cm^2$

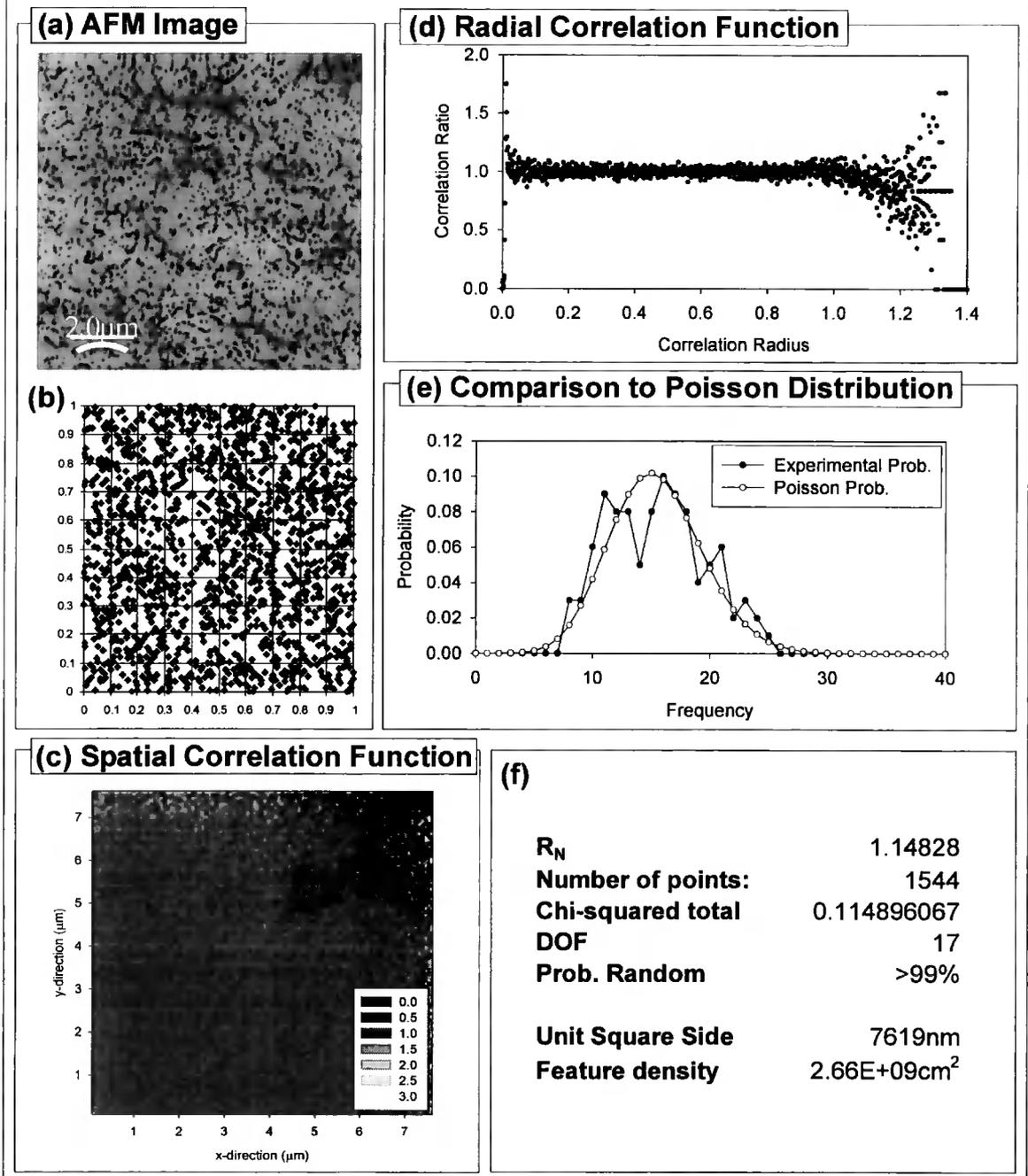**Figure 8.13:** Summary of statistical tests applied to the 14 period $In_{0.09}Ga_{0.91}N/GaN$ MQW STR241. (a) AFM image courtesy of Chaowang Liu, *Institute of Photonics, University of Strathclyde,* (b) Point distribution mapped on to a unit square, (c) spatial correlation function, (d) radial correlation function, (e) comparison to Poisson distribution, (f) summary of numerical data.
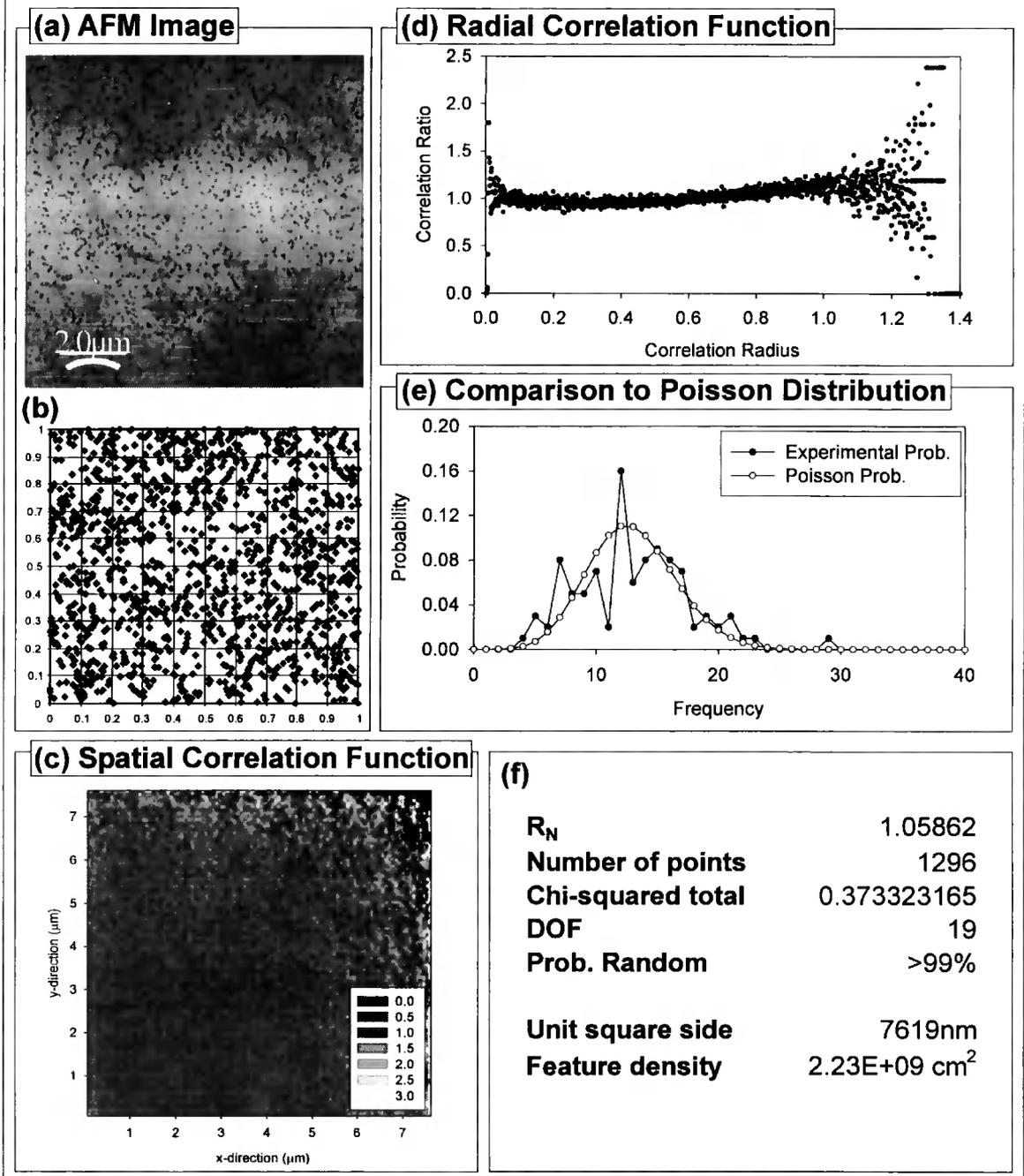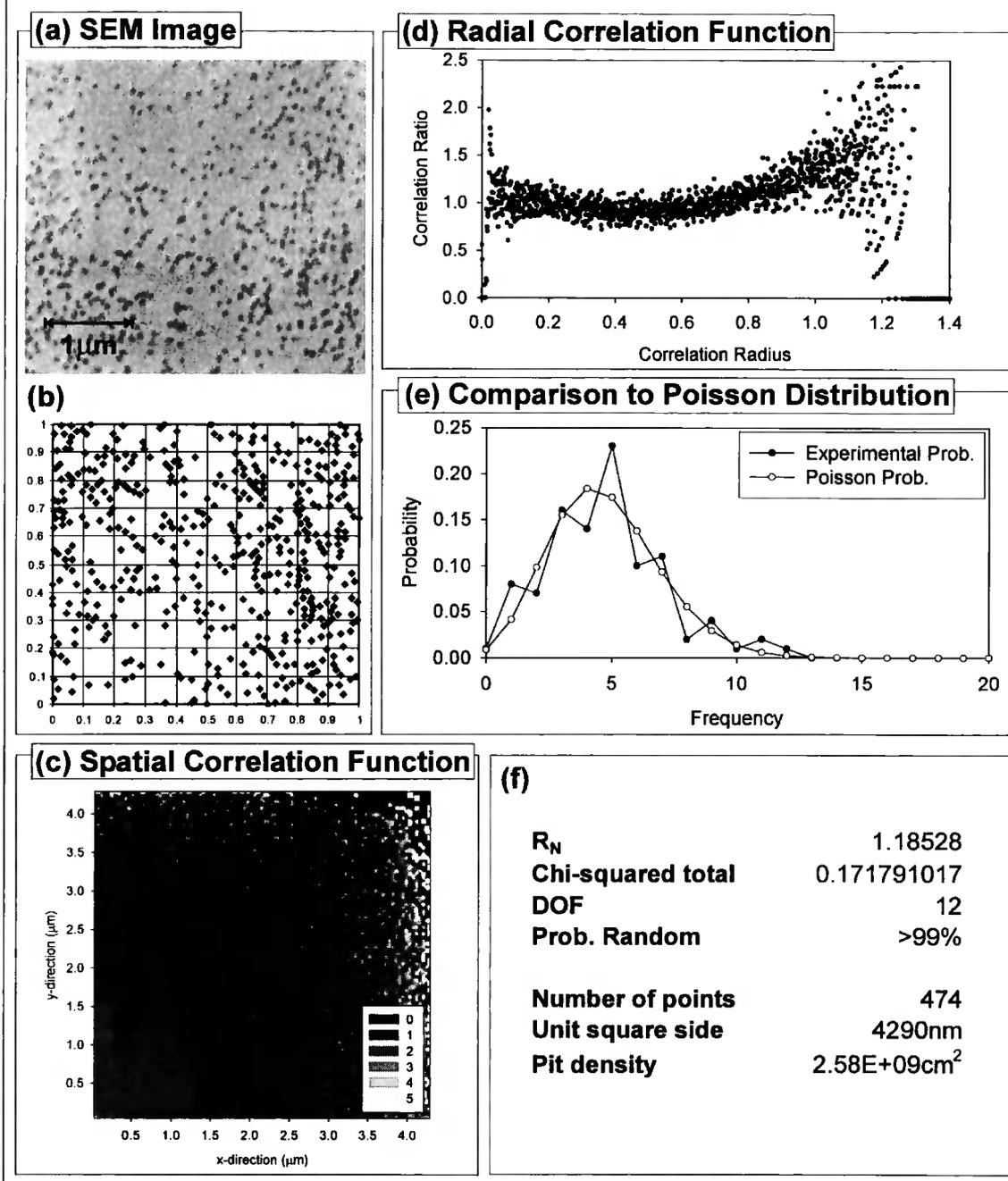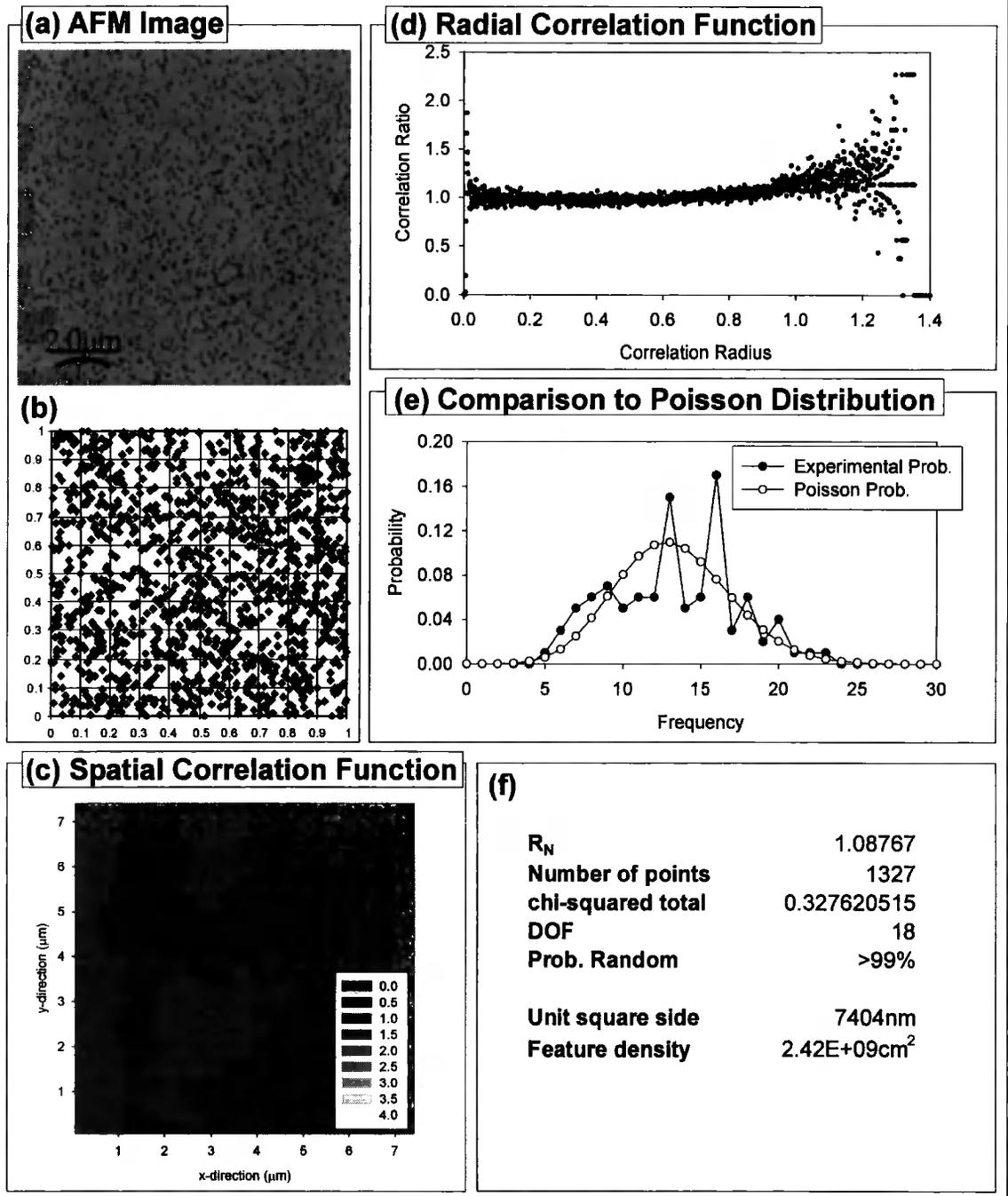
8.4.6 Analysis of Statistical Results

The numerical results of the statistical tests described in Section 8.2.2 and shown in Figures 8.10 to 8.13 are presented in Table 8.2 for comparison.

Sample	Pit Density	Distribution Parameter, R_N	Probability of Randomness	Length Scale of Observed Clustering
AFM STR94-10MQW	$2.7 \times 10^9 cm^2$	1.15	>99%	60-100nm
AFM STR204-10MQW	$2.2 \times 10^9 cm^2$	1.06	>99%	60-120nm
SEM STR204-10MQW	$2.6 \times 10^9 cm^2$	1.18	>99%	80-120nm
AFM STR241-14MQW	$2.4 \times 10^9 cm^2$	1.09	>99%	60-100nm

Table 8.2: Numerical results of the statistical tests described in Section 8.2.2 and presented in Figures 8.10-8.13.

Overall, the statistical tests performed indicate that the pit distributions seen in Figures 8.10(a) to 8.13(a) are random. However, clustering is observed on a length scale of 60-120nm. This is now discussed for each of the statistical tests.

The radial autocorrelation function has a similar shape for all four distributions. In each case there is an anti-correlation at very small radius corresponding to a separation of less than 60nm and a correlation at a separation of ~60-120nm. Beyond this the autocorrelation function is closely distributed about unity until it deviates at the higher radii values due to the smaller number of data points in the corners of the square which can participate in long range correlations. The anti-correlation at separations less than ~60nm is possibly due to the minimum identifiable pit separation. The autocorrelation function for the distribution in Figure 8.12 shows a broader distribution of points and more erratic behaviour in the tail of the function. This is due to the smaller number of data points in the distribution in comparison to the other distributions.

The probability of randomness as determined by application of the chi-squared test to the comparison of the experimental data to a Poisson distribution is greater than 99% for all four distributions. This is perhaps surprising as at first inspection the experimental distributions appear to deviate from the Poisson curve. However, the overall shape of the experimental distributions follows the

Poisson curves fairly closely and is particularly well behaved at the tails of the Poisson curves.

The spatial correlation function tests show grids of uniform intensity except in the corners where the correlation function first increases rapidly then decreases. This is thought to be due to the same effect that causes the radial autocorrelation function to deviate when the radius is greater than 1. The uniformity of the four spatial correlation functions shows there is no preferred orientation between the pits in the distributions.

The distribution parameter, R_n, for all four distributions is within the range 0.85-1.15 specified [6] for randomness. However, all the distribution parameters are greater than unity implying that there is a slight trend towards ordering in the distributions.

8.4.7 Discussion

Quantitative statistical tests for randomness showed the surface pits in 10 and 14 period $In_xGa_{1-x}N/GaN$ MQW structures to be randomly distributed on all length scales between 120nm and 7μm. Below 120nm the radial autocorrelation function identifies clustering of pits at a distance of 60-120nm. Below 60nm a fall in the radial autocorrelation function showed an absence of pits separated by this distance. This minimum resolvable feature size can be identified physically as the minimum distance two pits can be separated by before they merge during growth.

As discussed previously the relationship between V-pits, threading dislocations and the nucleation layer/buffer layer interface allows some inferences about the structure to be made from this analysis. As V-pits contain a threading dislocation at their vertices it is plausible to deduce that regions of high V-pit densities correspond to regions of high threading dislocation densities - assuming that the proportion of V-pits to threading dislocations is constant across the epitaxial layers. If regions of high dislocation density were correlated to tilt or twist boundaries in the nucleation layer/buffer layer interface [15] then it is possible that the position of surface V-pits would mark the boundaries of GaN micro-crystallites formed during the overgrowth of the GaN buffer layer as described by the model of Akasaki et al [17]. Analysis of V-pit distributions is complicated by the reported increased probability of V-pit formation from a

dislocation of mixed or screw type [28]. Therefore to evaluate the underlying structure it would be necessary to understand both the distribution of screw, mixed and edge dislocations and the relationship between the three dislocation types and the formation of V-pits.

GaN sub-grains are reported to have grain sizes in the range 50-500nm [16]. If the grain sizes were towards the bottom of this size range and the grains themselves were randomly distributed it is possible that V-pits formed by dislocations emanating from the grains would appear to be randomly distributed as the V-pits themselves can be larger than 50nm. This scenario would be consistent with the observations of randomness, but does not explain the peak of the radial autocorrelation function at 60-120nm.

The observation of clustering on the 60-120nm length scale is perhaps more consistent with there being sub-grains on the scale of ~500nm. Such clustering is possibly due to polygonisation walls. Indeed, such walls can be seen in Figures 8.10(a)-8.13(a) in which there is some indication of a cellular structure. (However this structure is not as strong as the synthetic regular honeycomb of points analysed in Figure 8.2(d).) Previous reports of similar cellular structures [31, 32] attribute the structures to misoriented grains. Such a model of dislocations propagating from grain boundaries suggests that the 'hot spots' in QW luminescence reported in Chapter 7 may correspond to regions of the QW grown above the centre of a GaN island where there is a lower density of luminescence quenching dislocations. This is not inconsistent with reports of enhanced band edge luminescence from the centre of GaN crystallites observed in plan view SEM-CL [33].

8.5 M-plane GaN

8.5.1 Stacking Faults in M-plane GaN

GaN epitaxial layers grown with M-plane (1-100) orientation on γ-LiAlO₂ benefit from the relatively low lattice mismatch of -1.4% (compression) along the [001]LiAlO₂ ∥ [11-20]GaN direction and -0.1% along the [010]LiAlO₂ ∥ [0001]GaN direction [34, 35]. Figure 8.14 shows the relative orientations of the crystallographic directions at the (1-100)ₐₐₙ, (100)ₗᵢₐₗₒ₂ interface. The epitaxial GaN films used in this work were grown by PAMBE [7, 36, 37] as described in Table 8.1. Further discussion of the GaN/LiAlO₂ system can be found in Chapter 3.
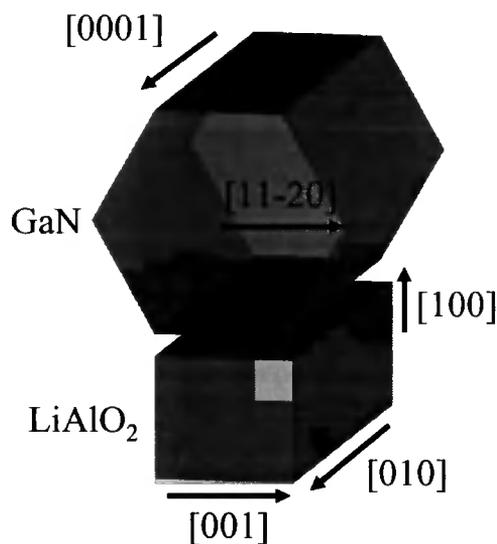
Figure 8.14: **Relative orientations of the crystallographic directions at the (1-100)ₐₐₙ, (100)ₗᵢₐₗₒ₂ interface.**

The dominant defects in M-plane GaN epilayers are reported to be intrinsic, I_2, basal plane stacking faults [38-40] that lie perpendicular to the interface and intersect the entire thickness of the layer. Figure 8.15 shows a cross sectional bright field micrograph of one of the samples. There appears to be a fairly uniform distribution of stacking faults with one area containing a high density bundle of stacking faults. The I_2 stacking fault results from slip of 1/3<10-10> in a perfect crystal:

ABABABAB... → AB**ABC**ACA...

The change to the hexagonal close packed structure from the stacking fault is equivalent to the introduction of a face centred cubic layer. Prism plane stacking mismatch boundaries are also reported on the (10-10) prism plane [8, 34]. However these are less common by a factor of 10-20 times and are not uniformly distributed. The density of threading dislocations is reported to be $<8 \times 10^8 cm^{-2}$ [8].
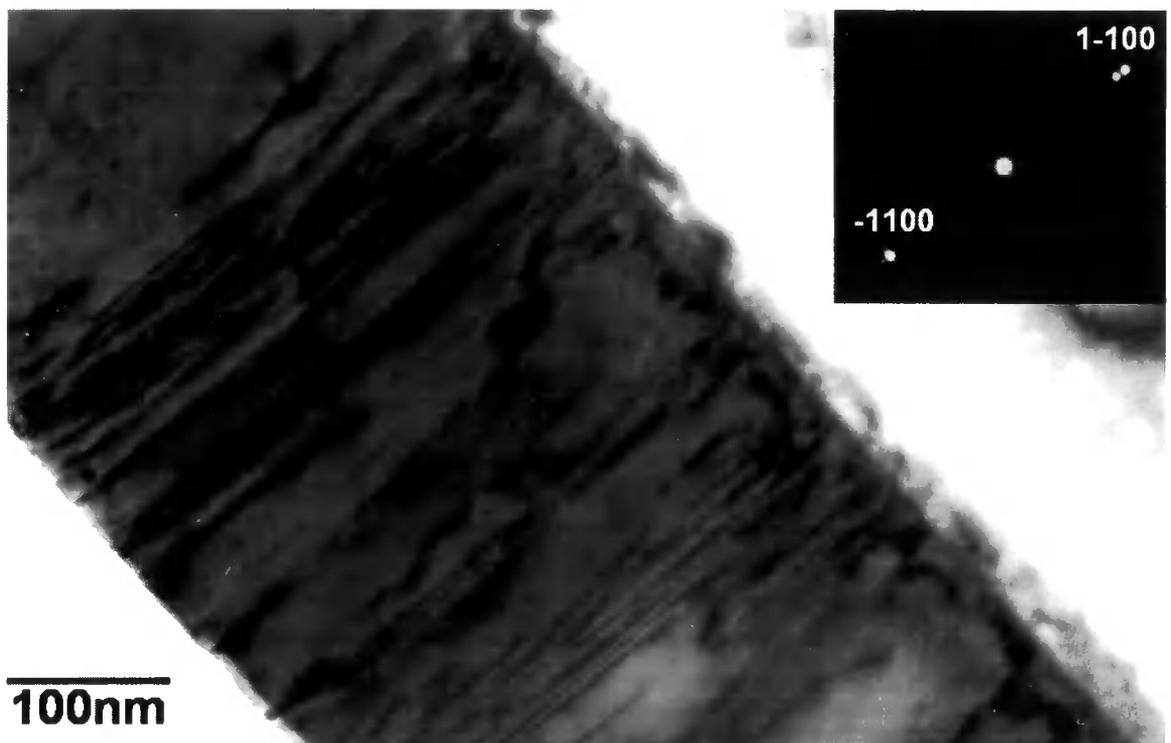
Figure 8.15: **Cross-sectional bright-field TEM micrograph near the [11-20] zone axis.**

The dominant basal plane stacking fault has no component in the [0001] direction (out of the faulted plane) and is therefore not able to relieve epitaxial strain. This suggests that the faults are related to the morphology of the substrate/epilayer interface. It is reported that bundles of basal plane stacking faults are observed where the substrate/epilayer interface is stepped [8, 38]. This is shown schematically in Figure 8.16.
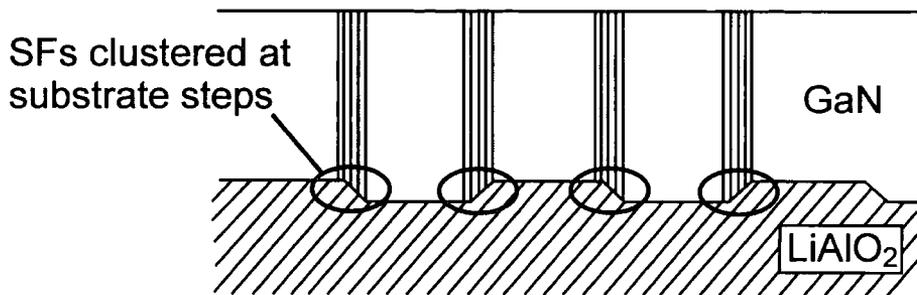
Figure 8.16: Diagram showing the proposed substrate/epilayer morphology.

Low temperature photoluminescence studies of M-plane GaN revealed a luminescence peak at 3.356eV (369.5nm). Using a combined TEM and SEM-CL study Sun *et al* [8] showed that this peak was spatially correlated with substrate roughening. Concentration of basal plane stacking faults at similar regions of substrate roughening was taken to be indirect evidence that the 3.356eV luminescence is stacking fault related. The substrate roughening is reported to take the form of periodic trenching on the substrate and was correlated with a striped pattern of ridges and trenches identified by AFM on the GaN epilayer. These ridges and trenches in turn were correlated with lines of bright CL contrast at 3.356eV in plan view SEM-CL measurements. In the next section the correlation of this luminescence to basal plane stacking faults is investigated using TEM-CL.

8.5.2 Luminescence from Stacking Faults

Cross-sectional foils[2] of M-plane GaN on LiAlO$_2$ (see Table 8.1) were investigated by TEM. Investigation by TEM from both **B**=[0001] and **B**=[11-20] revealed a high yet variable density of basal plane stacking faults, determined earlier by Trampert et al [34] to be intrinsic. As can be seen in Figure 8.15 and 8.17(c) the basal plane stacking faults are dominant. TEM investigation was hampered by the extreme sensitivity of the substrate to the electron beam. Under all but the lowest levels of observable beam currents the foil would move at a speed of several microns per second. Working at very low beam currents was

---

[2] TEM foils supplied by A. Trampert were prepared at the Paul-Drude Institute in Berlin, final Ar$^+$ milling was carried out in Durham.

beneficial. However the longer exposure times necessary somewhat mitigated the advantage gleaned by slowing down the rate of sample drift.

TEM-CL spectra were taken from the GaN epilayers using a CTEM beam focused down to a diameter of ~0.5μm. Acquisition times with a 2s integration and 5nm monochromator spectrometer step were up to 10 minutes depending on the wavelength range scanned. TEM-CL spectra taken in both **B**=[0001] and **B**=[11-20] orientations showed three main peaks. Figure 8.17(a) and (b) show typical spectra taken from these samples. The broad peak centred at 3.8eV (326.3nm) is due to the LiAlO$_2$ substrate. The peak centred near to 3.5eV (354nm) is attributed to GaN near band edge emission. The peak at 3.3-3.35eV (370.1-375.8nm) varies in relative intensity and is very consistently strongest where the density of basal plane stacking faults is greatest. This is illustrated in Figure 8.17 (a) and (b) which were recorded with the beam focused on to the areas highlighted in Figure 8.17(c).

The relationship between stacking faults and the luminescence seen at 3.3-3.35eV was further investigated by taking a line-scan of CL intensity along the centre of the GaN layer parallel to the substrate, with the spectrometer set to select the peak at 3.3eV. The line scan was taken using an electron probe formed using the STEM scanning unit and taking a CL intensity reading every 10nm. With a 2s integration time a 5μm line scan took approximately 17 minutes. Due to the lower beam currents in STEM mode (see Chapter 6 for further discussion) the CL signal was much lower so the spectral dispersion was increased to 0.1eV. Despite this large spectral dispersion the variation in stacking fault luminescence was less marked than for the CTEM spectra as the dark noise was more significant. The line-scan is shown in Figure 8.17(d) and is aligned with the montage of TEM images shown in Figure 8.17(c). There is a direct correspondence between the densities of stacking faults and the luminescence intensity maxima and minima. Inspection of the TEM montage of the GaN layer shows the stacking faults appear in bundles with a periodicity of ~0.5μm. This corresponds to the periodicity of the trenches identified in the substrate prior to growth by Sun et al [8].
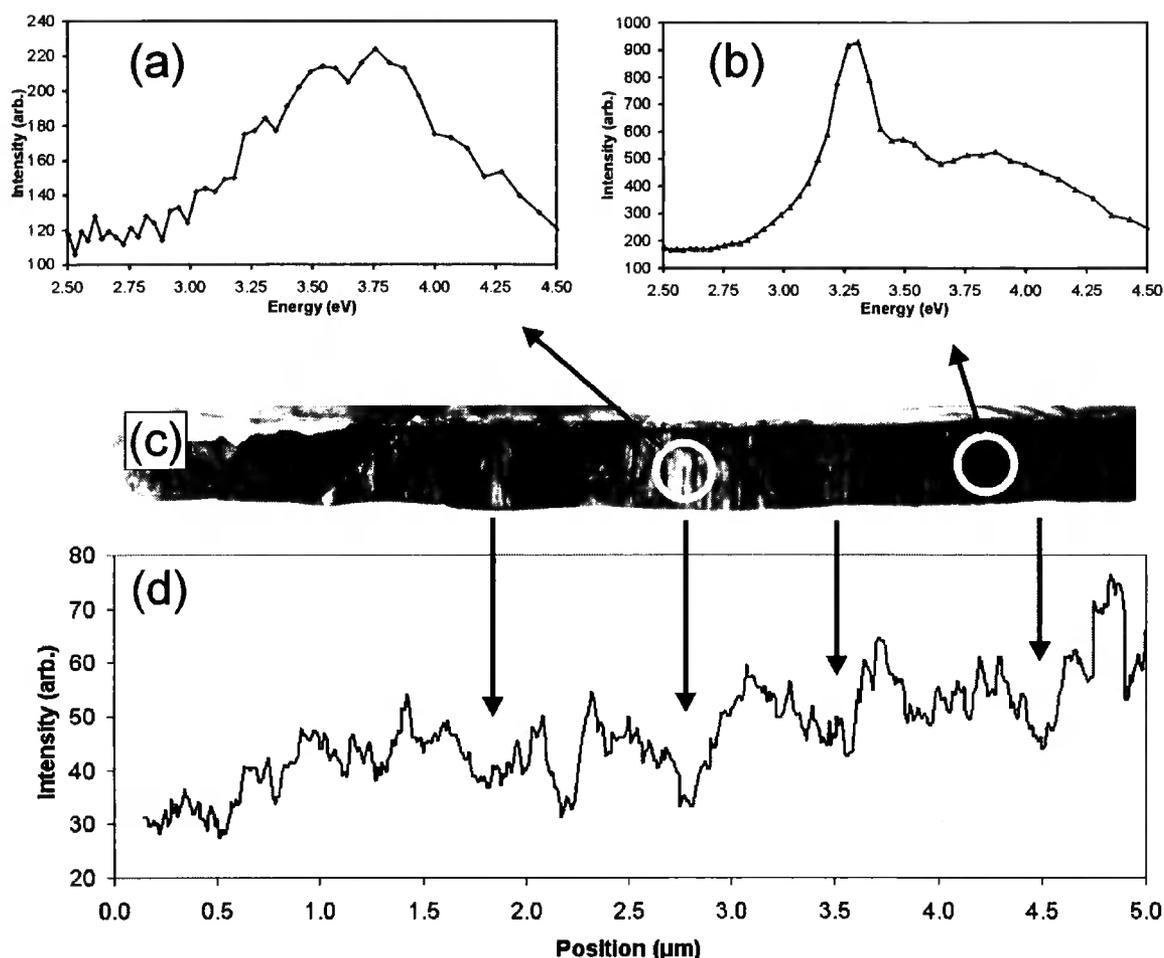
Figure 8.17: Cross-section TEM-CL investigation of M-plane GaN on LiAlO₂. (a) TEM-CL spectrum of area containing a low density of stacking faults, (b) TEM-CL spectrum of area containing a high density of stacking faults, (c) TEM montage with B=[11-20] multi-beam image, and (d) CL line-scan with spectrometer centred on 3.3eV (375.8nm).

8.5.3 Analysis and Discussion

As demonstrated in Figure 8.17 TEM-CL spectroscopy and monochromatic line-scans have established a correlation between stacking faults and 3.3eV (375.8nm) luminescence. Whilst it is possible that this emission is due to point defects and impurities accumulating in the vicinity of stacking faults there are well known models in the literature attributing the luminescence to excitons bound to the stacking faults [41-43]. The emission energy observed in this work (3.3eV) is at the lower end of the range of energies (3.3-3.4eV) at which lines have been previously attributed to excitons bound to stacking faults [44, 45]. However

the spectral resolution typically used in TEM-CL is far inferior to PL and the spectroscopy is performed at a higher temperature (nominally 100K) as opposed to 5K in PL.
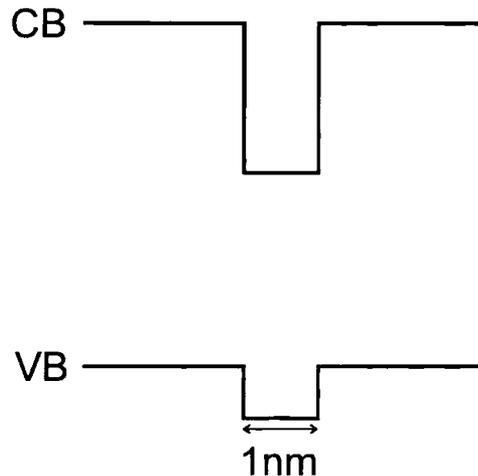
Figure 8.18: Diagram showing the type II potential well at an I₂ stacking fault in wurtzite GaN.

Stacking faults are considered to form quantum well-like regions since the stacking error is equivalent to the introduction of a thin zinc-blende layer embedded in the wurtzite matrix [8, 41, 42]. The width of the cubic layer is 2c (1.04nm) since the I_2 stacking sequence, ABABABCA-CAC..., contains two units of cubic stacking. Band structure calculations by Rebane et al [41] show that I_2 stacking faults act as quantum wells for electrons and potential barriers for holes, therefore attracting electrons to the stacking faults but repelling holes. Figure 8.18 shows the alignment of the bands to form a structure similar to a type II heterojunction. In such a structure holes may be attracted to the electron bound to the stacking faults through the Coulomb force, forming excitons bound to stacking faults (SFE). The binding energy of the SFE was estimated to be 45meV [41].

These models yielded an inter-band transition energy of 3.359eV [8, 42], assuming that the stacking faults have a spatial separation of 5nm, which was in good agreement with PL data given by Sun *et al* [8]. Whilst the stacking fault related peak seen in this work is centred at 3.3eV it covers a broad spectral range from 3.25-3.35eV at 100K. Therefore, this peak is considered to be the same as the feature studied by Sun et al [8] at 3.356eV and the direct correlation with

stacking faults presented in this work confirms Sun's earlier conclusions that it is stacking fault related luminescence.

8.6 Conclusions

Panchromatic STEM-CL imaging and diffraction contrast imaging of a cross-sectional $In_{0.1}Ga_{0.9}N$ SQW thin foil was used to investigate the effect of threading dislocations on the QW luminescence. Threading dislocations crossing the QW were shown to be associated with regions of lower QW luminescence. This observation is consistent with reports in the literature that threading dislocations in GaN can act as non-radiative recombination centres. However, no comment is made about the relative effects of edge, mixed and screw dislocations as non-radiative recombination centres.

The distributions of threading dislocations observed in CTEM micrograph montages were analysed using a one-dimensional autocorrelation function normalised to highlight spatial correlations such as clustering. Distributions of <100 dislocations revealed no significant clustering. However, the small number of dislocations in the distributions is below the optimum number ideally required for correlation analysis. This lack of clustering of dislocations is not consistent with the model whereby threading dislocations are propagated in clusters from misaligned GaN crystallites formed on the low temperature GaN buffer layer. This problem was investigated by a statistical analysis of V-pits as secondary evidence for the presence of dislocations.

Quantitative statistical tests for radial correlations, spatial correlations, and clustering were used to analyse V-pits in AFM and SEM images of the surface of 10 and 14 period $In_xGa_{1-x}N/GaN$ MQW structures. These pits were shown to be randomly distributed on all length scales between 120nm and 7μm, clustered at a distance of 60-120nm and anti-correlated below 60nm. Physically this anti-correlation was interpreted as the minimum pit separation before the pits merged. As V-pits have been shown to contain threading dislocations at their vertices the observed clustering at 60-120nm was considered to be due to clusters of threading dislocations. These clusters of threading dislocations are reported to be initiated at tilt or twist boundaries between GaN micro-crystals formed during the overgrowth of a GaN low temperature nucleation layer. As

such the observed clustering of V-pits is suggested to be the result of threading dislocations emanating from the boundaries of GaN micro-crystals forming lines of closely spaced V-pits on the surface of the MQW. A random distribution of the micro-crystals is thought to account for the randomness of the V-pits observed on a scale of 120nm to 7μm. It is suggested that the 'hot spots' in QW luminescence reported in Chapter 7 may correspond to the centre of GaN micro-crystallites where the density of dislocations is lower.

(1-100) GaN grown on (100) γ-LiAlO₂ was studied using combined diffraction contrast imaging and CL spectroscopy and monochromatic CL line-scans. Basal plane stacking faults originating from substrate roughness were shown to be distributed in periodic clusters. These basal plane stacking faults were demonstrated to be directly associated with a broad emission peak in the range 3.3-3.35eV (370.1-375.8nm) at 100K. This finding is consistent with reported SEM-CL and PL analysis revealing a peak at 3.35eV (PL at 5K) seen in samples with a high density of basal plane stacking faults.

8.7 References

1. Waltereit, P., O. Brandt, A. Trampert, H.T. Grahn, J. Menniger, M. Ramsteiner, M. Reiche, and K.H. Ploog, *Nitride Semiconductors Free of Electrostatic Fields For Efficient White Light-Emitting Diodes,* Nature **406** (2000) 865-868.

2. Durose, K., A.J.W. Yates, A. Szczerbakow, J. Domagala, Z. Golacki, and K. Swiatek, *$CdS_{(x)}Te_{(1-x)}$: Bulk Vapour Growth, Twin Formation and the Electrical Activity of Twin Boundaries,* Journal of Physics D: Applied Physics **35** (2002) 1997-2007.

3. Walker, E.M., D.J. Buckley, N.M. Boyall, K. Durose, K. Grasza, A. Szczerbakow, and W. Palosz, *Spatial Analysis of Dislocation Distribution as a Means of Assessing Crystal Growth Processes,* Institute of Physics Conference Series **169** (2001) 215-218.

4. Rose, D., K. Durose, W. Palosz, A. Szczerbakow, and K. Grasza, *Methods of Dislocation Distribution Analysis and Inclusion Identification with Application to CdTe and (Cd,Zn)Te,* Journal of Physics D: Applied Physics **31** (1998) 1009-1016.

5. Cousins, M.A., *Microstructure of Absorber Layers in CdTe/CdS Solar Cells,* PhD Thesis (2001), Department of Physics, University of Durham, Durham.

6. Waugh, D., *Geography: An Integrated Approach,* (Thomas Nelson and Sons Ltd, Hong Kong, 1990).

7. Waltereit, P., O. Brandt, M. Ramsteiner, A. Trampert, H.T. Grahn, J. Menniger, M. Reiche, and K.H. Ploog, *M-plane GaN(1-100) Grown on g-$LiAlO_2$(100): Nitride Semiconductors Free of Internal Electrostatic Fields,* Journal of Crystal Growth **227-228** (2001) 437-441.

8. Sun, Y.J., O. Brandt, U. Jahn, T.Y. Liu, A. Trampert, S. Cronenberg, S. Dhar, and K.H. Ploog, *Impact of Nucleation Conditions on the Structural and Optical Properties of M-Plane GaN(1-100) Grown on γ-$LiAlO_2$,* Journal of Applied Physics **92** (2002) 5714-5719.

9. Pereira, S., E. Pereira, E. Alves, N.P. Barradas, K.P. O'Donnell, C. Liu, C.J. Deatcher, and I.M. Watson, *Depth Profiling InGaN/GaN Multiple Quantum Wells by Rutherford Backscattering: The Role of Intermixing.,* Applied Physics Letters **81** (2002) 2950-2952.

10. Deatcher, C.J., C. Liu, S. Pereira, M. Lada, A.G. Cullis, Y.J. Sun, O. Brandt, and I.M. Watson, *In Situ Optical Reflectometry Applied to Growth of Indium Gallium Nitride Epilayers and Multi Quantum Well Structures,* Semiconductor Science and Technology **18** (2003) 212-218.

11.   Hurst, P., P. Dawson, S.A. Levetas, M.J. Godfrey, I.M. Watson, and G. Duggan, *Temperature Dependent Optical Properties of InGaN/GaN Quantum Well Structures,* Physica Status Solidi B **228** (2001) 137-140.

12.   Wu, X.H., L.M. Brown, D. Kapolnek, S. Keller, B. Keller, S.P. DenBaars, and J.S. Speck, *Defect Structure of Metal-Organic Chemical Vapor Deposition-Grown Epitaxial (0001) GaN/Al₂O₃,* Journal of Applied Physics **80** (1996) 3228-3237.

13.   Nakamura, S., *GaN Growth Using GaN Buffer Layer,* Japanese Journal of Applied Physics **30** (1991) L1705-L1707.

14.   Ponce, F.A., *Microstructure of Epitaxial III-V Nitride Thin Films,* in *GaN and Related Materials,* S.J. Pearton, (Gordon and Breach Science Publishers, Amsterdam, 1997).

15.   Mathis, S.K., A.E. Romanov, L.F. Chen, G.E. Beltz, W. Pompe, and J.S. Speck, *Modeling of Threading Dislocation Reduction in Growing GaN Layers,* Journal of Crystal Growth **231** (2001) 371-390.

16.   Qian, W., M. Skowronski, M.D. Graef, K. Doverspike, L.B. Rowland, and D.K. Gaskill, *Microstructural Characterisation of a-GaN Films Grown on Sapphire by Organometallic Vapor Phase Epitaxy,* Applied Physics Letters **66** (1995) 1252-1254.

17.   Akasaki, I., H. Amano, Y. Koide, K. Hiramatsu, and N. Sawaki, *Effects of AlN Buffer Layer on Crystallographic Structure and on Electrical and Optical Properties of GaN and Ga$_{(1-x)}$Al$_{(x)}$N (0<x<0.4) Films Grown on Sapphire Substrate by MOVPE,* Journal of Crystal Growth **98** (1989) 209-219.

18.   Ponce, F.A., *Structural Defects and Materials Performance of the III-V Nitrides,* in *Group III Nitride Semiconductor Compounds,* B. Gil, (Oxford University Press, Oxford, 1998).

19.   Lester, S.D., F.A. Ponce, M.G. Craford, and D.A. Steigerwald, *High Dislocation Densities in High Efficiency GaN-Based Light-Emitting Diodes,* Applied Physics Letters **66** (1995) 1249-1251.

20.   Nakamura, S., *III-V Nitride-Based Short-Wavelength LEDs and LDs,* in *Group III Nitride Semiconductor Compounds,* B. Gil, (Oxford University Press, Oxford, 1998).

21.   Rosner, S.J., E.C. Carr, M.J. Ludowise, G. Girolami, and H.I. Erikson, *Correlation of Cathodoluminescence Inhomogeneity With Microstructural Defects in Epitaxial GaN Grown by Metalorganic Chemical-Vapor Deposition.,* Applied Physics Letters **70** (1997) 420-422.

22.   Sugahara, T., H. Sato, M. Hao, Y. Naoi, S. Kurai, S. Tottori, K. Yamashita, K. Nishino, L.T. Romano, and S. Sakai, *Direct Evidence that Dislocations are Non-Radiative Recombination Centers in GaN,* Japanese Journal of Applied Physics **37** (1998) L398-L400.

23. Cherns, D., *The Structure and Optoelectronic Properties of Dislocations in GaN*, Journal of Physics: Condensed Matter **12** (2000) 10205-10212.

24. Cherns, D., S.J. Henley, and F.A. Ponce, *Edge and Screw Dislocations as Nonradiative Centers in InGaN/GaN Quantum Well Luminescence*, Applied Physics Letters **78** (2001) 2691-2693.

25. Albrecht, M., H.P. Strunk, J.L. Weyher, I. Grzegory, S. Porowski, and T. Wosinski, *Carrier Recombination at Single Dislocations in GaN Measured by Cathodoluminescence in a Transmission Electron Microscope*, Journal of Applied Physics **92** (2002) 2000-2005.

26. Northrup, J.E. and J. Neugebauer, *Indium-Induced Changes in GaN(0001) Surface Morphology*, Physical Review B **60** (1999) R8473-R8476.

27. Chen, Y., T. Takeuchi, H. Amano, I. Akasaki, N. Yamada, Y. Kaneko, and S.Y. Wang, *Pit Formation in GaInN Quantum Wells*, Applied Physics Letters **72** (1998) 710-712.

28. Wu, X.H., C.R. Elsass, A. Abare, M. Mack, S. Keller, P.M. Petroff, S.P. DenBaars, J.S. Speck, and S.J. Rosner, *Structural Origin of V-Defects and Correlation With Localised Excitonic Centres in InGaN/GaN Multiple Quantum Wells*, Applied Physics Letters **72** (1998) 692-694.

29. Liliental-Weber, Z., Y. Chen, S. Ruvimov, and J. Washburn, *Formation Mechanism of Nanotubes in GaN*, Physical Review Letters **79** (1997) 2835-2838.

30. Miraglia, P.Q., E.A. Preble, A.M. Roskowski, S. Einfeldt, and R.F. David, *Helical-Type Surface Defects in GaN Thin Films Epitaxially Grown on GaN Templates at Reduced Temperatures*, Journal of Crystal Growth **253** (2003) 16-25.

31. Liu, C., C.J. Deatcher, M.G. Cheong, and I.M. Watson, *Atomic Force Microscopy of InGaN-Based Structures Grown by Metal-Organic Vapour Phase Epitaxy*, Institute of Physics Conference Series, In press.

32. Youtsey, C., L.T. Romano, R.J. Molnar, and I. Adesida, *Rapid Evaluation of Dislocation Densities in N-Type GaN Films Using Photoenhanced Wet Etching*, Applied Physics Letters **74** (1999) 3537-3539.

33. Ponce, F.A., D.P. Bour, W. Gotz, and P.J. Wright, *Spatial Distribution of the Luminescence in GaN Thin Films*, Applied Physics Letters **68** (1996) 57-59.

34. Trampert, A., T. Liu, P. Waltereit, O. Brandt, and K.H. Ploog, *Interface Structure and Epitaxial Growth of M-plane GaN(1-100) on Tetragonal LiAlO$_2$(100) Substrates*, Institute of Physics Conference Series **169** (2001) 277-280.

35. Xu, K., J. Xu, P. Deng, R. Qiu, and Z. Fang, *MOCVD Growth of GaN on LiAlO$_2$(100) Substrates*, Physica Status Solidi A **176** (1999) 589-593.

36. Waltereit, P., O. Brandt, M. Ramsteiner, R. Uecker, P. Reiche, and K.H. Ploog, *Growth of M-Plane GaN(1-100) on γ-LiAlO₂(100)*, Journal of Crystal Growth **218** (2000) 143-147.

37. Waltereit, P., O. Brandt, M. Ramsteiner, A. Trampert, H.T. Grahn, J. Menniger, M. Reiche, R. Uecker, P. Reiche, and K.H. Ploog, *Growth of M-Plane GaN(1-100): A Way to Evade Electrical Polarization in Nitrides*, Physica Status Solidi A **180** (2000) 133-138.

38. Trampert, A., T.Y. Liu, and K.H. Ploog, *Defect Structure of Thin GaN Epilayers: M-Plane Versus C-Plane Growth*, Proceedings of the Fourth Symposium on Non-Stoichiometric III-V Compounds (2002) 111-118.

39. Hull, D. and D.J. Bacon, *Introduction to Dislocations*, (Pergamon Press plc, Oxford, 1984).

40. Kelly, A. and G.W. Groves, *Crystallography and Crystal Defects*, (Longman Group Ltd, London, 1970).

41. Rebane, Y.T., Y.G. Shreter, and M. Albrecht, *Stacking Faults as Quantum Wells for Excitons in Wurtzite GaN*, Physica Status Solidi A **164** (1997) 141-144.

42. Stampfl, C. and C.G.V. Walle, *Energetics and Electronic Structure of Stacking Faults in AlN, GaN, and InN*, Physical Review B **57** (1998) R15052-R15055.

43. Bandic, Z.Z., T.C. McGill, and Z. Ikonic, *Electronic Structure of GaN Stacking Faults*, Physical Review B **56** (1997) 3564-3566.

44. Grandjean, N., M. Leroux, M. Laugt, and J. Massies, *Gas Source Molecular Beam Epitaxy of Wurtzite GaN on Sapphire Substrates Using GaN Buffer Layers*, Applied Physics Letters **71** (1997) 240-242.

45. Wetzel, C., S. Fischer, J. Kruger, E.E. Haller, R.J. Molnar, T.D. Moustakas, E.N. Mokhov, and P.G. Baranov, *Strongly Localized Excitons in Gallium Nitride*, Applied Physics Letters **68** (1996) 2556-2558.

Discussion and Conclusions

9.1 Discussion and Conclusions

In this thesis the technique of (S)TEM-CL has been investigated and applied to the study of GaN epitaxial layers and $In_xGa_{1-x}N/GaN$ QW structures. The samples investigated were GaN epitaxial layers grown by MOVPE and PAMBE on sapphire and $LiAlO_2$ substrates respectively, and MOVPE grown $In_xGa_{1-x}N/GaN/Al_2O_3$ QW structures. CL collection is performed using a parabolic mirror with a small hole to allow passage of the electron beam positioned above the specimen inside the TEM pole-piece. CL is reflected out of the column by the mirror into a spectrometer/photomultiplier arrangement. The major motivation for implementing such a system is its ability to correlate spectral information with structural information from TEM. In addition limited beam broadening and a small effective carrier diffusion length (pinned by surface recombination) in a thin TEM foil gives STEM-CL a high spatial resolution making it a useful technique for investigating nanostructures. A necessary consequence of using an electron transparent specimen is a weak CL signal due to a small generation volume and large free carrier losses to surface recombination. This leads to conflicting requirements; the thicker the foil the stronger the signal, but at the expense of

spatial resolution. An additional factor to consider is beam damage. Analysis of in-situ degradation curves of panchromatic CL from GaN epilayers and $In_{0.1}Ga_{0.9}N$ QW emission under electron beam irradiation revealed a decline in the luminescence which could be described through the introduction of non-radiative recombination centres.

Spectral acquisition in the (S)TEM-CL instrument is possible in either conventional TEM mode, STEM area scan or STEM point mode. Higher beam currents and larger illumination areas in conventional TEM yield much stronger CL signals facilitating faster and/or higher resolution spectral acquisition. Working in STEM mode allows panchromatic and monochromatic images and line-scans to be performed. Weak CL emission from TEM foils means monochromatic STEM-CL imaging generally required long integration times and large spectral dispersions. Long integration times are not always possible due to sample drift; line-scans, therefore, are a useful tool for increasing integration times.

To aid interpretation of STEM-CL data it is necessary to understand the generation of CL within a polished TEM foil and the effect of thickness fluctuation in the foil. Fabry-Perot interference fringes have been observed in spectra acquired with a stationary probe. A numerical model was created to model the interference term at the collection mirror from CL generated in a thin column in the TEM foil. This allowed the interference fringe periodicity to be predicted for a given thickness and wavelength. Fitting the expected fringe periodicity to an experimentally observed spectrum allowed the foil thickness to be estimated.

Apart from interference effects, to predict the effect of thickness variation on CL intensity a model was developed to predict the expected CL intensity from a region of particular thickness using the Everhart-Hoff depth-dose function and taking into account surface recombination losses. To check this experimentally and to allow image normalisation the transmitted electron intensity in STEM was used to estimate the foil thickness using the dynamical formulation of electron diffraction. This process allowed a STEM image to be used to create an expected CL image based on the assumption that the foil is a uniform material, luminescing uniformly. Therefore, dividing the actual CL image by the expected CL image revealed underlying contrast due to the foil material rather than foil thickness variation. In practice the images to be analysed were electronically processed to create line-scans prior to normalisation.

This technique was applied to panchromatic STEM-CL imaging of MOVPE grown $In_{0.1}Ga_{0.9}N/GaN/Al_2O_3$ QWs in cross-section. These panchromatic images revealed that the CL emission from the QWs was inhomogeneous with bright regions of luminescence behaving as apparent 'hot spots' 200-700nm in width. The thickness normalisation confirmed that this inhomogeneity was an underlying property of the material and not due to foil thickness variation. Investigating this with monochromatic STEM-CL imaging and line-scans along the length of the wells revealed detectable levels of luminescence at ±10nm either side of the characteristic QW luminescence peak, QW_λ. In regions where QW_λ was bright, CL at QW_λ ±10nm and ±5nm was also observed to be bright. In regions where QW_λ was darker, CL at QW_λ ±10nm and ±5nm was also observed to be darker. Indium rich regions in the QW are often postulated to account for $In_xGa_{1-x}N$ luminescence, and the possibility of such regions causing the observed 'hot spots' was considered. Indium rich regions would result in a deepening of the QW. If such a region was directly excited by the electron beam luminescence at a wavelength greater than QW_λ would be expected. However, if a 'normal' region were directly excited it may be expected that CL at QW_λ would be observed in addition to CL at longer wavelengths from carriers moving along the QW and recombining at the regions of lower potential energy associated with indium clustering. As behaviour of this sort was not observed it is therefore suggested that large scale (>200nm) indium rich regions are not responsible for luminescent 'hot spots'.

This inhomogeneity in $In_{0.1}Ga_{0.9}N$ QW luminescence is in contradiction to the findings of Albrecht *et al* [1] who performed STEM-CL and energy selected imaging on $In_{0.2}Ga_{0.8}N$ SQWs and $In_{0.1}Ga_{0.9}N$ MQWs grown by MOVPE on dislocation free GaN single crystals. STEM-CL monochromatic mapping in cross-section revealed the QW luminescence to be homogeneously distributed on a length scale greater than 5nm (the minimum probe size). Analysis of the indium content of the wells revealed indium concentration fluctuations on a length scale of 3-9nm. This was taken as evidence that the optical properties of $In_xGa_{1-x}N$ QWs are not influenced on a nanometre scale by indium segregation, but rather, are determined by a short range order resulting from the localisation of the hole wave function at the indium atom as proposed by Bellaiche and Zunger [2]. This explanation, however, does not account for the observation of long range (>200nm) inhomogeneity seen in this study. A possible explanation for this

difference is the effect of dislocations acting as non-radiative recombination centres and as a source of epitaxial strain relief.

Comparison of panchromatic STEM-CL micrographs and montages of diffraction contrast TEM images revealed that bundles of threading dislocations suppress QW luminescence. This investigation, and literature evidence supporting the suppositition that dislocations act as non-radiative recombination centres, is given in the first part of Chapter 8. It is, therefore, possible that the observed 'hot spots' are in fact islands of luminescence surrounded by dislocations suppressing QW luminescence. (It is possible that the interaction between the dislocation strain fields and the QW have an influence on local luminescence efficiency.) This may account for the difference between these results and those of Albrecht *et al* [1], as the dislocation density in the material grown on GaN single crystals is likely to be lower than the material grown on sapphire substrates in this study. As it is only possible to evaluate a small volume of material using TEM the distribution of dislocations was evaluated across the surface of sapphire/GaN/$In_xGa_{1-x}N$ MQWs using V-pits as secondary evidence for the presence of dislocations. The distribution of V-pits was mapped using SEM and AFM, and analysed for clustering, and spatial and radial correlations using statistical tests. No long range (>200nm) clustering was found; clustering, however, on a length scale of 60-120nm was identified. This is possible due to clustering of dislocations formed from the coalescence of misaligned GaN islands during the early stages of epitaxial growth. There was no evidence of correlations between periodically separated sub-grain boundaries. This does not, however, preclude a random distribution of sub-grains in terms of both size and positions. It is, therefore, possible that the 'hot spots' correspond to regions of QW grown above the centre of a GaN island where there is a lower density of luminescence quenching dislocations. Other factors to be considered are that the inhomogeneous $In_{0.1}Ga_{0.9}N$ QW luminescence is an artefact of sample preparation, beam induced damage or surface contamination. Uniform luminescence from the GaN epilayers suggests that this is not the case but it is likely that the $In_{0.1}Ga_{0.9}N$ alloy is more susceptible to ion or electron beam damage.

Due to the spontaneous and piezoelectric polarisation of GaN in the [0001] direction, GaN epilayers grown on a non-polar plane are of interest. One of these planes is (1-100) GaN (M-plane) which may be grown on the (100) face of $LiAlO_2$

with a misfit of 0.3% in the GaN [0001] direction and 1.7% in the GaN [11-20] direction. The dominant defect type in plasma assisted MBE grown GaN layers in this orientation has been previously identified by Sun *et al* [3] as basal plane stacking faults lying perpendicular to the interface and intersecting the entire thickness of the layer. These stacking faults occur in bundles propagating from regions of roughness on the substrate. Using SEM-CL and PL Sun *et al* correlated luminescence at 3.356 eV (4K) from these samples with regions of substrate roughening. In this work TEM-CL spectroscopy and monochromatic line-scans were used to correlate luminescence at 3.3-3.35 eV (100K) with the stacking faults themselves. TEM-CL spectra from cross-sectional foils contained a peak at 3.3-3.35 eV which is consistently strongest where the density of basal plane stacking faults is greatest. A monochromatic line-scan at 3.3 eV along the centre of the GaN layer parallel to the substrate was aligned and compared against a TEM montage of the same area showing a direct correspondence between bundles of stacking faults and luminescent maxima.

The correlation of this spectral feature at 3.3-3.35 eV with stacking faults is consistent with models in the literature attributing transitions in the energy range 3.3-3.4eV to excitons bound to stacking faults. The intrinsic basal plane stacking fault in wurtzite GaN is equivalent to the inclusion of two layers of cubic stacking into the matrix. In simple terms the lower bandgap of cubic GaN means the cubic layer acts as a quantum well. Calculations such as those by Rebane *et al* [4] show this to be a type II QW such that excitons are formed with holes attracted to electrons bound in the well. Accounting for the spontaneous polarisation results in a triangular potential with a redshift of the luminescence and a transition energy of 3.359 eV [3]. This is in close agreement with the PL data from the same author. Whilst the stacking fault related peak seen in this work is centred at 3.3eV, it covers a broad spectral range (3.25-3.35 eV at 100K) and is considered to be the same as that identified by Sun *et al* [3] and is direct evidence of stacking fault related luminescence.

To the best of the author's knowledge this study is believed to be the first to report direct evidence of stacking faults acting as sites for radiative recombination in GaN.

9.2 References

1. Albrecht, M., V. Grillo, J. Borysiuk, T. Remmele, H.P. Strunk, T. Walther, W. Mader, P. Prystawko, M. Leszczynski, I. Grzegory, and S. Porowski, *Correlating Compositional, Structural and Optical Properties of InGaN Quantum Wells by Transmission Electron Microscopy*, Institute of Physics Conference Series **169** (2001) 267-272.

2. Bellaiche, L. and A. Zunger, *Effects of Atomic Short-Range Order on the Electronic and Optical Properties of GaAsN, GaInN, and GaInAs Alloys*, Physical Review B **57** (1998) 4425-4431.

3. Sun, Y.J., O. Brandt, U. Jahn, T.Y. Liu, A. Trampert, S. Cronenberg, S. Dhar, and K.H. Ploog, *Impact of Nucleation Conditions on the Structural and Optical Properties of M-Plane GaN(1-100) Grown on γ-LiAlO2*, Journal of Applied Physics **92** (2002) 5714-5719.

4. Rebane, Y.T., Y.G. Shreter, and M. Albrecht, *Stacking Faults as Quantum Wells for Excitons in Wurtzite GaN*, Physica Status Solidi A **164** (1997) 141-144.

Appendix A

Computer Code

A1 Introduction

This appendix lists the full code for all the programs used in this work. In some cases the code has not been developed solely by the author, but is based upon previously used routines. The Image Analysis and 2D Point Logging Routines running in Visual Basic were originally developed by Dr Mike Cousins, the 1D Autocorrelation Function, Nearest Neighbour Analysis, Comparison to a Poisson Distribution, and Radial Autocorrelation functions have been developed over a number of years by the author, Andrew Yates, Deborah Buckley, Eddie Walker, and Dr Ken Durose. The Fabry-Perot Simulation and Spatial Correlation Function routines have been newly developed for this work.

A2 Image Analysis

This image analysis routine to obtain position intensity data from greyscale bitmaps is described in Section 4.7 and is used extensively in Chapter 7. The code is designed to run in *Visual Basic*.

```
Dim arr() As Long

Private Sub Command1_Click()

ReDim arr(1 To Picture1.ScaleWidth)


For j = 1 To Picture1.ScaleHeight

    For i = 1 To Picture1.ScaleWidth
        arr(i) = arr(i) + (Picture1.Point(i, j) /
65536)
        Next i

Next j

Open "C:\My Documents\My PhD\Term
7\23 October 2002\scan1-edited-
20June02.txt" For Output As #1
```

```
For i = 1 To Picture1.ScaleWidth
    Print #1, i, arr(i)
Next i
End Sub

Private Sub Form_Load()


Form1.Picture1.Picture = LoadPicture("C:\My
Documents\My PhD\Term 7\23 October
2002\scan1-edited-20June02.bmp")

Form1.Show

Picture1.ScaleMode = 3
End Sub
```

A3 Fabry-Perot Simulations

The Fabry-Perot Simulations described in Section 5.4.3 were performed using *Microsoft Excel* for numerical calculations controlled by a *Visual Basic* macro, listed below, to automate the data handling.

```
Sub ThicknessIntegrals()
'
'
' Macro written 21 May 2002, N. Boyall
'

    Do
        Sheets("Integral calcs").Select
        Range("E3").Select
        Range("E3") = ActiveCell.Value + 10
        Range("C3").Select
        Selection.Copy
        Sheets("Wavelength Data").Select
        Range("B6").Select
        Selection.PasteSpecial Paste:=xlValues,
Operation:=xlNone, SkipBlanks:= _
        False, Transpose:=False
        Range("A7").Select

    Do

        Selection.Copy
        Sheets("Integral calcs").Select
        Range("C4").Select
        Selection.PasteSpecial Paste:=xlValues,
Operation:=xlNone, SkipBlanks:= _
        False, Transpose:=False
        Call Angles
```

```
        Range("M12").Select
        Selection.Copy
        Sheets("Wavelength Data").Select
        Selection.Offset(0, 1).Select
        Selection.PasteSpecial Paste:=xlValues,
Operation:=xlNone, SkipBlanks:= _
        False, Transpose:=False
        Selection.Offset(1, -1).Select
        Loop Until ActiveCell.Value = Empty

    Sheets("Wavelength Data").Select
    Range("B6:B2006").Select
    Selection.Copy
    Do
        ActiveCell.Offset(0, 1).Select
    Loop Until ActiveCell.Value = Empty
    ActiveCell.Select
    Selection.PasteSpecial Paste:=xlValues,
Operation:=xlNone, SkipBlanks:= _
        False, Transpose:=False


    Sheets("Integral calcs").Select
    Loop Until Range("E3") = 50

    Application.ScreenUpdating = True
End Sub
Sub Integrals()
```

```
' Integrals Macro
'
   'Application.ScreenUpdating = False


   Do

      Sheets("Wavelength Data").Select
      ActiveCell.Select
      Selection.Copy
      Sheets("Integral calcs").Select
      Range("C4").Select
      Selection.PasteSpecial Paste:=xlValues,
Operation:=xlNone, SkipBlanks:= _
      False, Transpose:=False
      Call Angles
      Range("M12").Select
      Selection.Copy
      Sheets("Wavelength Data").Select
      ActiveCell.Offset(0, 1).Select
      Selection.PasteSpecial Paste:=xlValues,
Operation:=xlNone, SkipBlanks:= _
      False, Transpose:=False
      ActiveCell.Offset(1, -1).Select
      Loop Until ActiveCell.Value = Empty

   'Application.ScreenUpdating = True

End Sub
```

```
Sub Angles()

   Dim Dummy As Integer
   Dim Dummy2 As Double

   Application.ScreenUpdating = False
   Sheets("Integral Calcs").Select
   Range("F10") = 8
   'F10 is set to 8 so as not to run the
calculation too close to the critical angle so r
isn't too great
   Dummy = 0
   Dummy2 = 0

   Do

      Dummy = Range("F10")
      Dummy = Dummy + 1
      Range("F10") = Dummy
      Dummy2 = Dummy2 + Range("K12")


      Loop Until Range("F10") = Range("F9")
- 6
   ' -6 covers the angle not collected from the
hole in the CL mirror


   Range("M12") = Dummy2
   'Application.ScreenUpdating = True

End Sub
```

A4 1D Autocorrelation Function

The following *FORTRAN* code is used to perform the one-dimensional radial correlation function described in Section 8.2.1. The data is read into the program in *Unit22* in x,z form where x is the position on the unit line, and z is the associated thickness for each data point. This program calculates a new normalisation file each time it is run. The correlation function is outputted in *Unit44*.

```
program radial

integer n,c,freq(2,1100), l, m, k, nx, xc, p, v,
xr, nbins,j
real x,points(2,1100),a, b, pois(1100),
pro(1100),sumpro,sumpois,rand(4,25000)
double precision xb,box_width,increm,
tally(3,1100),r
character unit22*65,unit44*65,unit3*65
```

```
!22 is the data from your sample
NAMEdata.txt
unit22='D:\1_D\raw_data\1Dclustered.txt'
!44 is the main output file for the radial
correlation function
unit44='D:\1_D\Results\1DclusteredRADIAL
.txt'
!3 is the non-normalised data from radial
correlation function
unit3='D:\1_D\Results\1QW1v2chck.txt'
```

```
open (unit=22, file =unit22)
open (unit=44, file=unit44)
open (unit=3, file=unit3)

write(6,*)'enter a value for n, the number of
points'
read(*,*)n
call getdata(n,points)
call random(n,rand)
call radius(n,points,xr,tally,rand)

close(3)
close(22)
close(44)
!close(55)


stop
end


!************the subroutines***************
! getdata gets the data from file 22 and puts it
into array 'points'
subroutine getdata(n,points)
real points(2,1100)
integer n,m
write(6,*)'reading in data from file'
do m=1,n,1
 read(22,*)points(1,m),points(2,m)
end do
return
end

! prepares and returns normalised random
correlation data set
subroutine random(n,rand)
real rand(4,25000),x,xr,increm,r,s
integer n,i,a,b,m


Call random_seed
Do i=1,1000,1
   call random_number(x)
   rand(1,i)=x
end do

increm=0.005
do xr=0,1.02,increm
   i=1+nint(xr/increm)
   rand(2,i)=xr
end do

write(*,*)'calculating radial values for random
numbers'

do a=1,1000
     write(*,*)'working on point',a
  do b=(a+1),1000
    r=sqrt((rand(1,b)-rand(1,a))**2)
      do xr=0,1.02,increm
      i=nint(xr/increm)
      if((r.ge.xr).and.(r.lt.(xr+increm)))then
         rand(3,i)=rand(3,i)+1.0
         else
```

```
        end if
      end do
   end do
end do
a=0

sum=0
do s=increm,1.02,increm
!fiddled from 0,1.44 and also s/increm
   a=nint((s-increm)/increm)
    sum=sum+rand(3,a)
end do
a=0
write(*,*)'        test sum is',sum
write(*,*)' if even should be',n*((n/2)-1)+n/2
write(*,*)'  if odd should be',n*(n-1)/2

m=0
lim=nint(1.02/increm)

do m=1,lim
 rand(4,m)=real(rand(3,m)/real(sum))
end do
write(*,*)rand(1,5),rand(2,5),rand(3,5),rand(4,
5)
pause 10
return
end


!'radius' calculates the radial correlation
function

subroutine radius(n,points,xr,tally,rand)
integer a,b,n,c,lim,dummy4,j,i
real
increm,r,s,points(2,1100),tally(3,1000),xr,su
m,ref,tal(3,1100),rand(4,1000)

!defines the increment 'increm' and fills
array'tally'with radial values
increm=0.005

do xr=0,1.02,increm
  i=1+nint(xr/increm)
   tally(1,i)=xr
end do

!tally(2,0)=0.0
write(*,*)'calculating radial values etc'

do a=1,n
     write(*,*)'working on point',a
  do b=(a+1),n
    r=sqrt((points(1,b)-points(1,a))**2)
       do xr=0,1.02,increm
       i=nint(xr/increm)
       if((r.ge.xr).and.(r.lt.(xr+increm)))then

tally(2,i)=tally(2,i)+(points(2,b)*points(2,a))
        else
        end if
     end do
  end do
end do
```

```
end do
a=0
sum=0
do s=increm,1.02,increm
!fiddled from 0,1.44 and also s/increm
   a=nint((s-increm)/increm)
   sum=sum+tally(2,a)
end do

write(*,*)'      test sum is',sum
write(*,*)'  if even should be',n*((n/2)-1)+n/2
write(*,*)'   if odd should be',n*(n-1)/2

m=0
lim=nint(1.02/increm)

do m=1,lim
 tally(3,m)=real(tally(2,m)/real(sum))
 write(*,60)tally(1,m),tally(2,m),tally(3,m)
 write(3,60)tally(1,m),tally(2,m),tally(3,m)
end do
m=0
```

```
60 format(f15.6,3x,f15.6,3x,f15.6)
108 format(f15.6,',',f15.6)
do m=1,lim
! read(55,*)ref
 ref=rand(4,m)
 if (ref.eq.0.0)then
 ref=1
 end if
 !write(*,*)m
 write(44,108)tally(1,m),tally(3,m)/ref
 write(*,*)rand(4,m),ref,tally(1,m),tally(3,m)
end do

write(*,*)'increm=',0.025
write(*,*)'using n=',n,' points'

61 format(42x,f10.7)

return
end
```

A5 2D Point Logging Routine

The use of this *Visual Basic* routine is described in Secion 8.4.5 for logging the x,y coordinates of black dots on a white background. The distribution to be analysed must be provided in the form of a 1-bit bitmap.

```
Option Explicit
Type xy
   x As Integer
   y As Integer
End Type

Const MAXCENTS = 5000

Dim pic() As Integer, nocents As Integer
Dim cents(1 To MAXCENTS) As xy

Sub Get_Surrs(x As Integer, y As Integer)
Dim xp As Integer, yp As Integer
   pic(x, y) = -1
   Form1.Picture1.PSet (x, y), QBColor(13)
   nocents = nocents + 1
   cents(nocents).x = x
   cents(nocents).y = y


  On Error GoTo Errorlines1

  For yp = -1 To 1
    For xp = -1 To 1
      If pic(x + xp, y + yp) = 1 Then
Get_Surrs x + xp, y + yp
    Next xp
  Next yp
```

```
Exit Sub

Errorlines1:

 If Err = 9 Then Resume Next

 MsgBox (Error)


End Sub

Sub Load_Picture(FName As String, szx As
Integer, szy As Integer)
Dim x As Integer, y As Integer


Form1.Picture1.Picture = LoadPicture(FName)

'Form1.Width = Form1.Picture1.ScaleWidth
'Form1.Height = Form1.Picture1.ScaleHeight
+ 28
'Form1.Picture1.Left = 0
'Form1.Picture1.Top = 0


Form1.Picture1.ScaleMode = 3
Form1.Show
```

```
szx = Form1.Picture1.ScaleWidth
szy = Form1.Picture1.ScaleHeight
Form1.Caption = "Saving Picture as Array"

ReDim pic(1 To szx, 1 To szy)
    For y = 1 To szy
        For x = 1 To szx
            If Form1.Picture1.Point(x, y) =
QBColor(0) Then
                pic(x, y) = 1
            End If
Next x, y

End Sub

Sub main()
Const PicName = "D:\NMB_Thesis\Chapter 8
- Extended Defects\c-plane\Synthetic
distributions\Honeycomb.bmp"
Const SaveName = "D:\NMB_Thesis\Chapter
8 - Extended Defects\c-plane\Synthetic
distributions\Honeycomb.dat"
Dim x As Integer, y As Integer, szx As Integer,
szy As Integer
'in pic(), 1 = black, 0 = white, -1 = black but
selected
'Open_Bitmap PicName, pic(), szx, szy
Load_Picture PicName, szx, szy
Open SaveName For Output As #1
Form1.Show
'Draw_Bitmap pic(), szx, szy, Form1.Picture1
```

```
'Form1.Picture2.Picture =
LoadPicture(PicName)

Form1.Caption = "Getting Points...)"
For y = 1 To szy
    For x = 1 To szx
        If pic(x, y) = 1 Then
            Get_Surrs x, y
            Save_Point
        End If
    Next x
Next y

Close #1
Form1.Caption = "Finished"
'x = Shell("notepad " & SaveName, 1)
End Sub

Sub Save_Point()
Dim i As Integer
Dim xtemp As Long, ytemp As Long

    For i = 1 To nocents
        xtemp = xtemp + cents(i).x
        ytemp = ytemp + cents(i).y
    Next i
    xtemp = xtemp / nocents
    ytemp = ytemp / nocents
    Print #1, xtemp, ytemp

    nocents = 0
End Sub
```

A6 Nearest Neighbour Analysis

The following *FORTRAN* code is used to calculate the nearest neighbour distribution parameter, R_n, described in Section 8.2.2. Point distributions need to be mapped onto a unit square with axis such that $0 \le x \le 1$ and $0 \le y \le 1$ prior to data analysis. The program reads in the raw data formatted in lines of x,y coordinates into the file specified as *Unit22*. The distribution parameter is displayed on screen.

```
! 'NEARN' calculates a single value
distribution parameter Rn
! for the data set in
a\samplesdata\NAMEdata.txt and
! returns it to the screen. A file of nearest
neighbour
! distances is put into
a\results\NAMEnear.txt. It has few uses,
! but Rn is a useful parameter

program NEARN
```

```
integer a,b,c,j,k,n
real points(2,2000), nn(2000), r(2000),
mean,tt,rn,aa,bb,area
character unit22*65, unit99*65

!change the NAME in unit 22 in the next line
unit22='D:\2d analysis disk
1\Samplesdata\Honeycomb.dat'
unit99='D:\2d analysis disk
1\results\Honeycomb.txt'
open(unit=22,file=unit22)
open(unit=99,file=unit99)
```

```
!defines parameters
write(6,*)'enter the number of points'
read(*,*)n

call getdata(n,points)

!do i=1,4
! write(*,*)points(1,i),points(2,i)
!end do

! calculates distance between all points
do a=1,n
 nn(a)=1000
  c=1
  r(1)=1.2
  do b=1,n,1
    c=c+1
    r(c)=sqrt(((points(1,b)-
points(1,a)))**2+(points(2,b)-points(2,a))**2)

    if(a.eq.b)then
    r(c)=r(c-1)
    else
    goto 111
  111 end if
    if(r(c).le.r(c-1).and.r(c).lt.nn(a)) then
    nn(a)=r(c)
    else
    nn(a)=nn(a)
    end if
  end do
  write(99,*)nn(a)
end do

do k=1,20
!write(6,*)nn(k)
end do
```

```
close(22)

tt=0.0d0
do k=1,n,1
tt=tt+nn(k)
end do

!calculate mean distance between closest
points
mean=tt/n
write(*,*)'                number of points is
n=',n
write(*,*)'sum of nearest neighbour distances
is  tt=',tt
write(*,*)'mean nearest neighbour distances is
=',mean
!area=aa*bb
area=1
write(*,*)'area of the unit squre is
=',area

!calculate rn value
rn=2.0d0*mean*(sqrt(n/area))
write(*,*)'                        rn is',rn
!close(99)
end

!'getdata' retrieves the x-y data from file unit
22 and puts it in array 'points'
subroutine getdata(n,points)
real points(2,2000),dummy(2,2000)
integer n,m,aa,bb
do m=1,n,1
  read(22,*)points(1,m),points(2,m)
end do
return
end
```

A7 Comparison to Poisson Distribution

The following *FORTRAN* code performs the Poisson test described in Section 8.2.2. Point distributions need to be mapped onto a unit square with axes such that $0 \le x \le 1$ and $0 \le y \le 1$ prior to data analysis. The program reads in the raw data formatted in lines of x,y coordinates into the file specified as *Unit22*. The Poisson distribution data is outputted in the file *Unit 11*.

```
! point does the poisson distribution test for
data file unit 22

program poiss

integer n,c,freq(2,1100), l, m, k, nx, xc, yc, p,
v, xr, nbins,j
```

```
real x,y, points(2,1100),a, b, pois(1100),
pro(1100),sumpro,sumpois
double precision xb, yb, box_width,increm, r,
tally(3,1100)
character yn, name*20, fil1*30, fil2*30,
corref*30, alldat*30
character comdat*30, source*30, ques,
raddat*30, corrl*40
```

```
character unit11*65, unit22*65, unit222*65,
unit33*65, unit44*65
character unit3*65, unit55*65

! enter paths

!11 is the output file from subroutine 'answer'
unit11 ='d:\2d analysis disk
1\Results\hexPOISSON.xls'
!22 is the scatter data
unit22='d:\2d analysis disk
1\Samplesdata\hex.dat'

open (unit=11, file =unit11)
open (unit=22, file =unit22)
!open (unit=222, file=unit222)
!open (unit=33, file=unit33)
!open (unit=44, file=unit44)
!open (unit=3, file=unit3)
!open (unit=55, file=unit55)

!defines parameters

do k=1,1100
 freq(1,k)=k-1
 freq(2,k)=0
end do

k=0
box_width=0.05d0
write(6,*)'enter a value for n, the number of
points'
read(*,*)n
call getdata(n,points)
write(*,*)'using n=',n,' points ....
box_width=',box_width

! box test creates frequency table from array
'points' in array 'freq'
nx=nint(1/box_width)
c=0
i=1

do yc=0,nx-1,1
       !write(*,*)'just about to enter box test
second loop yc=',yc
   do xc=0,nx-1,1
     xc=',xc
     xb=real(xc)*box_width
     yb=real(yc)*box_width
           do i=1,n,1
             x=points(1,i)
             y=points(2,i)

if((x.ge.xb).and.(x.lt.(xb+box_width)))then
if((y.ge.yb).and.(y.lt.(yb+box_width)))then
                 ! write(*,*)'found a point in
position ',xb,yb
                    c=c+1
                    else
                    end if
                end if
              end do
         if(c.ge.0)then
```

```
       freq(2,c+1)=freq(2,c+1)+1
       c=0
       else
       end if
    end do
end do
write(*,*)' '
write(6,*)'the first three frequencies are'
write(6,*)'points in box*',freq(1,1), freq(1,2),
freq(1,3)
write(6,*)'freq for this*',freq(2,1), freq(2,2),
freq(2,3)
write(*,*)' '

call probab(m,v,freq,pro)
call table(i,p,freq)


write(6,*)'numb of points using the freq table
= ',p
! calculates the mean for use in the poisson
work

a=n*box_width*box_width
write(6,*)'mean numb of points per box = ',a

call poisson(pois, a,m,freq)
call answer(m,v,freq,pro,pois,nbins)

write(*,*)'total proability checksums'
do j=1,100
      sumpro=sumpro+pro(j)
      sumpois=sumpois+pois(j)
end do
write(*,*)'probabilty sum from data
is',sumpro
write(*,*)'probability sum (poisson)
is',sumpois

20 format(a1)
close(3)
close(11)
close(22)
close(222)
close(44)
close(55)
stop
end

!***********the subroutines***************
! getdata gets the data from file 22 and puts it
into array 'points'
subroutine getdata(n,points)
real points(2,1100)
integer n,m
write(6,*)'reading in data from file'
do m=1,n,1
 read(22,*)points(1,m),points(2,m)

end do
return
end
```

```
!probab calculates the probabilities from the
frequency data in 'freq'
subroutine probab(m,v,freq,pro)
integer m,v,freq(2,1100)
real pro(1100)
do m=1,1000
   v=v+freq(2,m)
end do
write(*,*)'there are',v,'boxes if v is not 100
theres a problem'
do m=1,1000
 pro(m)=real(freq(2,m)/real(v))
end do
write(6,*)' '
write(6,*)'the first three probabilities are:'
write(6,*)'points in a box      ',freq(1,1),
freq(1,2), freq(1,3)
write(6,*)'prob from freq      ',pro(1), pro(2),
pro(3)
write(6,*)' '
return
end


!'table' checks whether the number of points
in freq equals n
subroutine table(i,p,freq)
integer i,freq(2,1100),p
i=0
p=0
do i=1,1000,1
   p=p+(freq(1,i)*freq(2,i))
end do
return
end


!poisson calculates the poisson values for
freq(1,n)
subroutine poisson(pois,a,m,freq)
integer m,freq(2,1100)
real pois(1100),a
```

```
pois(1)=exp(-a)
write(*,*)'first poisson value exp(-a)= pois(0)
is',exp(-a)
do m=2,1000,1
   pois(m)=(a*pois(m-1))/real(freq(1,m))
end do

write(*,*)' '
write(6,*)'the first three poisson data points
are'
write(6,*)'number in a
box',freq(1,1),',',freq(1,2),',',freq(1,3)
write(6,*)'poisson
probabs',pois(1),',',pois(2),',',pois(3)
write(6,*)' '
return
end


!answer writes the data to a file
subroutine answer(m,v,freq,pro,pois,nbins)
integer v,mon,freq(2,1100),dummy2,nbins
real
pro(1100),pois(1100),dummy3,dum22,dum33
nbins=0
dummy2=0
dummy3=0
dum22=0
dum33=0
totalfreq=0
write(11,*)'numb    freq    prob    pois
prob'

do m=1,100,1
 write(11,30)freq(1,m),freq(2,m),pro(m),pois(m)
     nbins=nbins+1
end do
30 format(i4,3x,i4,3x,f15.7,3x,f15.7)
return
end
```

A8 Radial Autocorrelation Function

The following *FORTRAN* code performs the radial autocorrelation test described in Section 8.2.2. Point distributions need to be mapped onto a unit square with axis such that $0 \le x \le 1$ and $0 \le y \le 1$ prior to data analysis. The program reads in the raw data formatted in lines of x,y coordinates into the file specified as *Unit22*. *Unit 55* contains normalisation data created using a random distribution. The radial autocorrelation function is outputted in *Unit44*.

```
program RADpoint

integer n,c,freq(2,1100), l, m, k, nx, xc, yc, p,
v, xr, nbins,j
real x,y, points(2,1100),a, b, pois(1100),
pro(1100),sumpro,sumpois
```

```
double precision xb, yb, box_width,increm, r,
tally(3.1100)
character yn, name*20, fil1*30, fil2*30,
corref*30, alldat*30
character comdat*30, source*30, ques,
raddat*30, corrl*40
```

```fortran
character unit11*65, unit22*65, unit222*65,
unit33*65, unit44*65
character unit3*65, unit55*65

!22 is the scatter data
unit22='D:\2d analysis disk
1\Samplesdata\Honeycomb.dat'
!44 is the main output file for the radial
correlation function
unit44='D:\2d analysis disk
1\Results\HoneycombRNorm0001.xls'
!55 contains reference data generated from
random numbers
unit55='D:\2d analysis disk
1\Programs\Refdat\NORMRdata0001.xls'

open (unit=22, file =unit22)
open (unit=44, file=unit44)
open (unit=55, file=unit55)

!defines parameters

write(6,*)'enter a value for n, the number of
points'
read(*,*)n
call getdata(n,points)
call radius(n,points,xr,tally)

20 format(a1)
close(22)
close(44)
close(55)
stop
end

!************the subroutines***************
! getdata gets the data from file 22 and puts it
into array 'points'
subroutine getdata(n,points)
real points(2,1100)
integer n,m
write(6,*)'reading in data from file'
do m=1,n,1
 read(22,*)points(1,m),points(2,m)
end do
return
end

!'radius' calculates the radial correlation
function

subroutine radius(n,points,xr,tally)
integer a,b,n,c,lim,dummy4,j,i
real
increm,r,s,points(2,1100),tally(3,1000),xr,su
m,ref,tal(3,1100)

!defines the increment 'increm' and fills
array'tally'with radial values
increm=0.001
```

```fortran
do xr=0,1.44,increm
  i=1+nint(xr/increm)
  tally(1,i)=xr
end do

write(*,*)'calculating radial values etc'

do a=1,n
    write(*,*)'working on point',a
  do b=(a+1),n
   r=sqrt((points(1,b)-
points(1,a))**2+(points(2,b)-points(2,a))**2)
    do xr=0,1.44,increm
     i=nint(xr/increm)
     if((r.ge.xr).and.(r.lt.(xr+increm)))then
        tally(2,i)=tally(2,i)+1.0
        else
        end if
    end do
  end do
end do
a=0

do s=increm,1.44,increm
  a=nint((s-increm)/increm)
   sum=sum+tally(2,a)
end do

write(*,*)'      test sum is',sum
write(*,*)'  if even should be',n*((n/2)-1)+n/2
write(*,*)'   if odd should be',n*(n-1)/2

m=0
lim=nint(1.44/increm)

do m=1,lim
 tally(3,m)=real(tally(2,m)/real(sum))
  write(*,60)tally(1,m),tally(2,m),tally(3,m)
end do
write(*,*)'test'
60 format(f15.6,3x,f15.6,3x,f15.6)
108 format(f15.6,',',f15.6)
do m=1,lim
 read(55,*)ref
 if(ref.eq.0.0)then
 ref=1
 end if
 write(*,*)m
 write(44,108)tally(1,m),tally(3,m)/ref
end do

write(*,*)'increm=',0.001
write(*,*)'using n=',n,' points'

61 format(42x,f10.7)

return
end
```

A9 Spatial Correlation Function

The following *FORTRAN* code is used to perform the test for spatial correlations described in Section 8.2.2. Point distributions need to be mapped onto a unit square with axis such that $0 \le x \le 1$ and $0 \le y \le 1$ prior to data analysis. The program reads in the raw data formatted in lines of x,y coordinates into the file specified as *Unit22*. A normalisation file generated using a random point distribution is contained in *Unit66*. *Unit44* contains the outputted spatial correlation function.

```fortran
program SPATIAL

integer n
real points(2,100000)
character unit22*65, unit44*65, unit66*65

!22 is the scatter data
unit22='D:\2d analysis disk
1\Samplesdata\hex.dat'
!44 is the main output file for the radial
correlation function
unit44='D:\2d analysis disk
1\Results\hexSpatial30000.dat'
!66 is a normalisation file generated from
random data
unit66='D:\2d analysis disk
1\Programs\Refdat\30000RadialNorm.dat'

open (unit=22, file=unit22)
open (unit=44, file=unit44)
open (unit=66, file=unit66)


write(6,*)'enter a value for n, the number of
points'
read(*,*)n
call getdata(n,points)
call vectors(n,points)


close(22)
close(44)
close(66)

stop
end


subroutine getdata(n,points)
real points(2,100000)
integer n,m
write(6,*)'reading in data from file'
do m=1,n,1
 read(22,*)points(1,m),points(2,m)
 write(*,*)points(1,m),points(2,m)
```

```fortran
end do
return
end


subroutine vectors(n,points)
integer s,t,n,x,y,xx,z
real
points(2,100000),norm(3,10000),a,b,c,d,grid(
3,10000),cc,dd,sum,dummy


write(*,*)'calculating vectors'

do x=0,9900,100
 y=y+1
 do xx=1,100,1
    z=x+xx
    grid(1,z)=xx
    grid(2,z)=y
    grid(3,z)=0
 end do
end do
y=0

do s=1,n,1
  a=points(1,s)
  b=points(2,s)
  write(*,*)a,b,s
  do t=1,n,1
    c=points(1,t)-a
    d=points(2,t)-b
    do x=1,10000,1
      cc=grid(1,x)/100
      dd=grid(2,x)/100
      if((c.lt.cc).and.(d.lt.dd).and.(c.ge.(cc-
0.01)).and.(d.ge.(dd-0.01)))then
        grid(3,x)=grid(3,x)+1
      else
      end if
    end do
    c=0
    d=0
  end do
end do
```

```
sum=1
do x=1,10000,1
  sum=sum+grid(3,x)
end do

do x=1,10000,1
  read(66,*)norm(1,x),norm(2,x),norm(3,x)
end do
```

```
do x=1,10000,1
  dummy=sum*norm(3,x)
  write(44,*)grid(1,x),grid(2,x),(grid(3,x)/sum)
end do

return
end
```

Reflectivity Calculations

B1 Derivation of Reflectivity[1]

Application of suitable boundary conditions to a plane monochromatic wave incident on a planar surface separating two isotropic, dielectric media yields the simplified Fresnel Equations B1 and B2:

$$r_\perp = \left(\frac{E_{0r}}{E_{0i}} \right)_\perp = \frac{n_i \cos\theta_i - n_t \cos\theta_t}{n_i \cos\theta_i + n_t \cos\theta_t} \tag{B1}$$

$$r_{\mathrm{II}} = \left(\frac{E_{0r}}{E_{0i}} \right)_{\mathrm{II}} = \frac{n_t \cos\theta_i - n_i \cos\theta_t}{n_i \cos\theta_t + n_t \cos\theta_i} \tag{B2}$$

where $r_\perp$ denotes the amplitude reflection coefficient perpendicular to the plane of incidence, r_{II} the amplitude reflection coefficient parallel to the plane of incidence, n_i is the refractive index of the material incident to the boundary and n_t is the refractive index of the material at the other side of the boundary.

---

[1] Hecht E., *Optics*, (Addison-Wesley, Reading Massachusetts, 1974).

For the purposes of this analysis we require the reflectance, R, defined as the ratio of the reflected over the incident flux. It can be shown that:

$$R = R_{II} \cos^2 \gamma_i + R_\perp \sin^2 \gamma_i \tag{B3}$$

and

$$T = T_{II} \cos^2 \gamma_i + T_\perp \sin^2 \gamma_i \tag{B4}$$

where γ_i is the azimuthal angle, defined as the angle between the plane of vibration and the plane of incidence such that:

$$\tan \gamma_i = \frac{[E_{0i}]_\perp}{[E_{0i}]_{II}} \tag{B5}$$

The solution of Equation B3 for all allowed angles of transmittance from the GaN foil is shown in Figure B1.

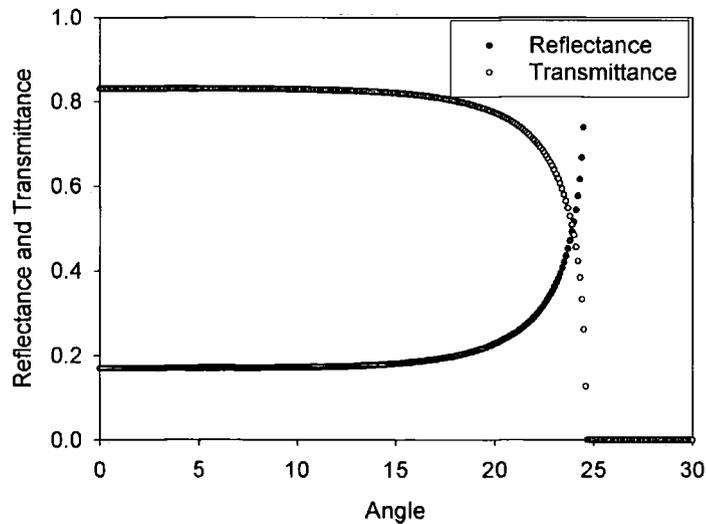**Figure B1:** **Reflectance and transmittance versus observed angle of escape for propagation of light from GaN to vacuum.**

Appendix C

List of Publications

'*Combined TEM-CL Investigation of Inhomogeneities in GaN Epilayers and InGaN Quantum Wells*', N.M. Boyall, K. Durose, T.Y. Liu, A. Trampert, and I.M. Watson, MSMXIII, In press.

'*The Effect of the Wall Contact and Post-Growth Cool-Down on Defects in CdTe Crystals Grown by 'Contactless' Physical Vapour Transport*', W. Palosz, K. Grasza, K. Durose, D.P. Halliday, N.M. Boyall, M. Dudley, B. Raghothamachar and L. Cai, Journal of Crystal Growth, **254**, 316-328, 2003.

'*A Method of Normalising Cathodoluminescence Images of Electron Transparent Foils for Thickness Contrast Applied to InGaN Quantum Wells*', N.M. Boyall, K. Durose and I.M. Watson, Journal of Microscopy, **209**, 41 - 46, 2003.

'*Simultaneous TEM and Cathodoluminescence Imaging of Non Uniformity in InGaN Quantum Wells*', N.M. Boyall, K. Durose and I.M. Watson, Materials Research Society Symposium Proceedings, **743**, 677-682, 2003.

'An In-Situ TEM Cathodoluminescence Study of Electron Beam Degradation of Luminescence from GaN and InGaN Quantum Wells', N.M. Boyall, K. Durose and I.M. Watson, Materials Research Society Symposium Proceedings, **743**, 683-688, 2003.

'Spatial Analysis of Dislocation Distribution as a Means of Assessing Crystal Growth Processes', E.M. Walker, D.J. Buckley, N.M. Boyall, K. Durose, K. Grasza, A Szczerbakow and W. Palosz, Institute of Physics Conference Series, **169**, 215 – 218, 2001.